Monthly Notices of the ROYAL ASTRONOMICAL SOCIETY

MNRAS **544,** 3647–3682 (2025) https://doi.org/10.1093/mnras/staf1721
Advance Access publication 2025 October 29

Eclipse mapping with *Ariel*: future prospects for a population-level mapping survey

Daniel Valentine [1,2★] Hannah R. Wakeford [1] Mark Hammond [3] Ryan C. Challener [4] Billy Edwards [5] Theresa Lüftinger[2] and Maximillian N. Günther [2]

[1]*School of Physics, University of Bristol, HH Wills Physics Laboratory, Tyndall Avenue, Bristol BS8 1TL, UK*
[2]*European Space Agency (ESA), European Space Research and Technology Centre (ESTEC), Keplerlaan 1, NL-2201 AZ Noordwijk, the Netherlands*
[3]*Department of Physics, University of Oxford, Oxford OX1 3PU, UK*
[4]*Department of Astronomy, Cornell University, 122 Sciences Drive, Ithaca, NY 14853, USA*
[5]*SRON Netherlands Institute for Space Research, Niels Bohrweg 4, NL-2333 CA Leiden, the Netherlands*

Accepted 2025 September 26. Received 2025 September 26; in original form 2025 May 27

ABSTRACT

Eclipse mapping is a powerful tool for measuring 3D profiles of exoplanet atmospheres. To date, only *JWST* has been capable of widely applying this technique, but as a general observatory, it is too time-limited to conduct population-level mapping studies. Ariel, on the other hand, is a dedicated exoplanet mission set to observe 1000 transiting exoplanets, making it a natural candidate for this. To assess *Ariel*'s mapping potential, we quantitatively benchmark its abilities against those of *JWST* using a simulation-and-retrieval framework with existing *JWST* eclipse maps as test cases. We find that for high-ranking targets, *Ariel* will be able to derive qualitatively similar maps to *JWST* using the same amount of observations; for mid-ranking targets, *Ariel* will be able to compete using as few as 3× as many observations; and for lower ranking targets, the use of phase curves overcomes the need for an impractical number of repeated eclipse observations. We find that while *Ariel* is unlikely to have extensive latitudinal mapping abilities, it will have wide-ranging longitudinal abilities, from which the first-order atmospheric dynamics can be constrained. Using an analytically derived metric, we determine the best eclipse mapping targets for *Ariel*, finding that it will be able to map nearly 100 targets using full phase curves in only quarter of its lifetime. This would be the largest mapping survey to date, and have enormous ramifications for our understanding of exoplanet atmospheric dynamics. Finally, we rank all the best mapping targets for both *JWST* and *Ariel* in order to encourage future eclipse mapping studies.

Key words: methods: observational – exoplanets – planets and satellites: atmospheres.

1 INTRODUCTION

Exoplanet atmospheres are complex, heterogeneous environments, but past studies have tended to treat them as 1D structures, primarily due to limitations associated with the precision, temporal coverage, and/or cadence of observations. The unprecedented quality of *JWST* data overcomes these limitations and now allows us to characterize the multidimensional profiles of exoplanet atmospheres (e.g. L.-P. Coulombe et al. 2023; M. Hammond et al. 2024; M. M. Murphy et al. 2024; N. Espinoza et al. 2024; R. C. Challener et al. 2024; D. Valentine et al. 2024b; M. Lally et al. 2025). However, as an oversubscribed general observatory, the opportunities to do this with *JWST* are limited.

The multidimensional profiles of exoplanet atmospheres have previously only been characterizable through the inversion of phase curves into flux maps (N. B. Cowan & E. Agol 2008). We refer to this technique as 'phase mapping', in which the entire planetary orbit is observed, allowing the flux of the visible hemisphere at every orbital phase to be measured and used to construct a global flux map. However, only differing longitudes are revealed by the planetary rotation, whilst the observed latitudes are constant. Additionally, this technique relies on whole-hemisphere measurements, which therefore only yield hemispherically averaged representations of the true spatial flux profile at each phase of rotation. Hence, only large-scale longitudinal information can be constrained by these so-called 'phase maps'. The use of phase curves also naturally limits the technique and subsequent inferences to planets with short enough periods to justify full-orbit observations; see L. Dang et al. (2025) for a comprehensive summary of *Spitzer* 4.5 μm phase curves.

Eclipse mapping takes this technique one step further in order to unlock the full 3D (longitude–latitude–pressure) profiles of exoplanet atmospheres (E. Rauscher et al. 2007). During eclipse ingress, the dayside of the planet is gradually occulted by the star, leading to gradual flux decreases in the light curve until the planet is fully eclipsed. The inverse is also true during egress as the planet is revealed from behind the star. With high-cadence data, these partial eclipse phases are well sampled, wherein the star is essentially observed to be obscuring/revealing successive 'slices' of the dayside profile. The change in flux between successive measurements can therefore be attributed to these slices, enabling slice profiles of the dayside atmosphere to be derived from both ingress and egress. Because

★ E-mail: daniel.valentine@bristol.ac.uk

the eclipse geometry of ingress is approximately inverse to that of egress for planets that orbit off the stellar equator, these slice profiles are oppositely oriented. Overlaying them therefore results in a grid which slices over both the longitudes and latitudes of the dayside hemisphere, within which the flux of each cell is measurable, thereby producing a 2D map of the dayside thermal profile (E. Rauscher, V. Suri & N. B. Cowan 2018). Performing this mapping technique as a function of pressure with spectroscopic observations further extends the profile to 3D. By exploiting the geometry of eclipse with high-cadence observations, eclipse mapping can therefore measure the latitudinal profiles of exoplanet atmospheres, and overall constrain smaller scale structure than is possible with phase mapping. However, eclipse mapping requires higher quality data than phase mapping, and can only map the dayside. For a comparison of phase versus eclipse mapping, see fig. 1 of J. Wit et al. (2012).

Spherical harmonics are traditionally used in the modelling framework of eclipse mapping because they can reproduce any pattern on a sphere, with the degree, $l_{\rm max}$, of the model denoting the complexity of the map. The first exoplanet to be eclipse mapped was HD 189733b, using 8 Spitzer/IRAC eclipses and a partial phase curve (C. Majeau, E. Agol & N. B. Cowan 2012; J. Wit et al. 2012). However, even with this large data set, the map could only constrain the first-order harmonics, corresponding to large-scale longitudinal patterns, and contained no robust latitudinal information, which is equivalent to what one would obtain with phase mapping alone. The unprecedented quality of *JWST* data now allows higher quality maps to be derived for more targets using fewer data.

A handful of exoplanets have now been eclipse mapped using *JWST*. The first of these was WASP-18b, mapped using a single NIRISS/SOSS eclipse as part of the ERS programme (L.-P. Coulombe et al. 2023). This map used up to fifth-order harmonics and contained evidence of magnetic field interactions with the atmosphere. Following this, WASP-43b was mapped using a MIRI/LRS phase curve (M. Hammond et al. 2024). This was the first eclipse map wherein the latitudinal profile was robustly constrained, revealing indications of a latitudinal hotspot offset. These indications were confirmed in an additional map of WASP-43b constructed from a NIRSpec/G395H phase curve, which provided a 4σ detection of this latitudinal asymmetry in the dayside atmosphere (R. C. Challener et al. 2024). WASP-17b was mapped from a single MIRI/LRS eclipse observation (D. Valentine et al. 2024b), revealing a substantial day-night temperature contrast with a marginal eastward hotspot offset, indicative of inefficient heat recirculation for this hot Jupiter. At the cooler end of the hot Jupiter regime, HD 189733b was mapped once again with the inclusion of two MIRI/LRS eclipse observations (M. Lally et al. 2025), revealing a much larger hotspot offset and smaller day-night temperature gradient than WASP-17b, indicative of efficient heat recirculation. WASP-69b was also preliminarily mapped from a MIRI/LRS eclipse, but degeneracies with the ephemeris led to an unconstrained hotspot location (E. Schlawin et al. 2024). These examples demonstrate the power of eclipse mapping in extracting dynamical information, with a number of other programmes having been accepted to carry out such studies with *JWST* (e.g. KELT-8b with MIRI/LRS, GO 5687, PI: Valentine; KELT-20b with NIRSpec/G395H, GO 6978, PI: Wardenier; TOI-2490b with NIRSpec/G395H, GO 7686, PI: Mullens).

In order to interpret the atmospheric dynamics of an exoplanet as inferred by the observables of an eclipse map, one must compare to general circulation models (GCMs), tuning different parameters until the same thermal structure is derived as that observed in the eclipse map. However, many of these parameters can be degenerate with one another; for example, both enhanced metallicity and atmospheric drag can seek to reduce the east–west hotspot offset, whilst rotation rate and irradiation temperature both dominate the heat recirculation regime at first order (T. Kataria et al. 2016; A. P. Showman, X. Tan & V. Parmentier 2020). Additionally, such comparisons carry a model dependence because the computational complexity of GCMs necessitate a number of a-priori assumptions and approximations to be made, the different choices of which can yield significantly different end results even when the input parameters are the same (M. Hammond et al. 2024). Degeneracies and model-dependencies such as these can be alleviated with a large and diverse enough sample to isolate control parameters and qualitatively test model assumptions across a wide parameter space (N. T. Lewis & M. Hammond 2022; A. Roth, V. Parmentier & M. Hammond 2024). Hence, a population-level eclipse mapping study is needed in order to truly utilize the wealth of atmospheric dynamic information that exoplanet eclipse maps contain. Whilst *JWST* has proved fruitful for pioneering the eclipse mapping technique, it is not conducive for such a time-costly study; a dedicated exoplanet mission is required.

An observatory must be capable of high-cadence, high-flux precision, and precise pointing observations in order to facilitate eclipse mapping. In order to perform 3D mapping, the observatory must also have spectroscopic capabilities. The natural candidate for such requirements is the *Ariel* mission (G. Tinetti et al. 2018). Set to launch in late 2029 as the next ESA medium-class (M4) science mission, *Ariel* will perform a census of the atmospheric chemistry and thermodynamics of hundreds of transiting exoplanets over a four-year primary mission lifetime. Designed for precise spectroscopic measurements on an L2 orbit, *Ariel* meets the above requirements for eclipse mapping, with continuous spectroscopic coverage from $1.1 - 7.8$ μm and photometric coverage down to 0.5 μm, sampling the majority of the flux output for irradiated exoplanets. Crucially, as a dedicated exoplanet mission, *Ariel* has the observing time that *JWST* does not to conduct a population-level mapping study.

Spitzer proved the baseline requirements for eclipse mapping from its ability to map the highest ranking eclipse mapping target (S. Boone, D. Grant & M. Hammond 2024), HD 189733b, at the most fundamental level (C. Majeau et al. 2012; J. Wit et al. 2012). The capabilities of the *Ariel* mission for such observations will supersede that of *Spitzer*, indicating that *Ariel* will at least have some degree of eclipse mapping abilities, the extent of which therefore needs to be determined.

The eclipse mapping capabilities of an observatory can be determined quantitatively via a simulation-and-retrieval framework, or qualitatively via analytic methods [e.g. using the eclipse mapping metric (EMM) proposed by S. Boone et al. 2024]. We apply both methods here to robustly assess *Ariel*'s eclipse mapping capabilities. Using the aforementioned *JWST* eclipse maps as test cases, we post-process them into simulated *Ariel* light curves for mock eclipse mapping retrievals in order to directly benchmark *Ariel*'s eclipse mapping abilities against those of *JWST*. We then use the methods of S. Boone et al. (2024) to rank all the best eclipse mapping targets and provide recommendations for the objectives, targets, and design of a population-level mapping survey with Ariel.

The structure of this paper is as follows. In Section 2, we outline our simulation-and-retrieval framework for our test case analysis, and verify that it produces consistent results with the input *JWST* maps. In Section 3, we use this framework to conduct our *Ariel* test case analysis, comparing the results to *JWST* in order to both assess *Ariel*'s mapping abilities, and directly benchmark the mapping abilities of the two observatories. In Section 4, we analytically rank the best mapping targets for both Ariel and *JWST*, and use the results of this and our test cases to devise a recommended target list and

Table 1. Test cases. These are the planets which have been reliably eclipse mapped with *JWST* to date, alongside a GCM output of HD 209458b. We use these to benchmark the eclipse mapping capabilities of the *Ariel* mission versus those of *JWST*.

Planet	*JWST* instrument	Observations	Reference
HD 189733b	MIRI/LRS	2 Eclipses	M. Lally et al. (2025)
HD 209458b	MIRI/LRS∗	1 Eclipse∗	M. Hammond & D. S. Abbot (2022)
WASP-18b	NIRISS/SOSS	1 Eclipse	L.-P. Coulombe et al. (2023)
WASP-17b	MIRI/LRS	1 Eclipse	D. Valentine et al. (2024b)
WASP-43b	MIRI/LRS	1 Phase Curve	M. Hammond et al. (2024)
	NIRSpec/G395H	1 Phase Curve	R. C. Challener et al. (2024)

Note. ∗HD 209458b has no *JWST* eclipse observations, but as one of the canonical hot Jupiters, we include a map post-processed from the 160 mbar level of a GCM of the planet, corresponding to pressures probed in the mid-IR, and integrated over the MIRI/LRS bandpass.

observational strategy for a population-level mapping survey with *Ariel*. Finally, in Section 5, we give our conclusions.

2 SIMULATION-AND-RETRIEVAL FRAMEWORK

In this section, we detail our simulation-and-retrieval framework. In order to directly benchmark the eclipse mapping capabilities of *Ariel* against those of *JWST*, we take every published *JWST* eclipse map to date[1] and use them as test cases. These are listed in Table 1, and span a range of *JWST* instruments, observational set-ups, and mapping-model complexities, which allow us to robustly assess *Ariel*'s mapping abilities across the observational parameter space. We note that we also include a map generated from the 160 mbar level of a `THOR` GCM of HD 209458b (L4 control case in M. Hammond & D. S. Abbot 2022), post-processed as it would be observed by a MIRI/LRS observation, since this planet has not yet been observed in eclipse with *JWST*. We choose to include it here because as one of the canonical hot Jupiters, it is a natural high-tier target for *Ariel*, therefore simulations of its eclipse mapping potential are imperative.

We then determine the data quantity that *Ariel* would need to derive a qualitatively equivalent map for each test case, and compare the quantitative constraints. To do this, we take the *JWST* eclipse map, post-process it into a simulated *Ariel* light curve and retrieve on it, continuously stacking observations if necessary until the input mapping signal is recovered. Whilst *Ariel* simultaneously observes using all of its spectrographs and photometric filters for every observation, which we highlight is highly advantageous for 3D mapping, we choose to conduct our simulations in the closest *Ariel* spectrograph to the input *JWST* spectrograph for fairness of comparison and ease of analysis. For *JWST* NIRISS/SOSS Order 1 ($0.85 - 2.83$ μm), this is *Ariel* NIRSpec ($1.10 - 1.95$ μm); for *JWST* NIRSpec/G395H ($2.84 - 5.14$ μm), it is *Ariel* AIRS Ch0 ($1.95 - 3.90$ μm); and for *JWST* MIRI/LRS ($5.0 - 12.0$ μm), it is *A riel* AIRS Ch1 ($3.9 - 7.8$ μm). A comparison between the bandwidths and throughputs of these instruments is shown in Fig. 1. We work with broad-band-integrated (i.e. 'white-light') light curves for the entirety of this analysis.

2.1 Simulation framework

We use the mapping software `starry` (R. Luger et al. 2019) to post-process these input maps into simulated light curves. To construct a light curve in `starry`, one sets up a star–planet system with user-defined orbital parameters; we adopt the same orbital parameters as those used in the original work for each test case (see Table 1). For

[1]The maps can be obtained through the Zenodo links contained within each reference. We exclude the WASP-69b eclipse map (E. Schlawin et al. 2024) due to the uncertainties reported by the authors.

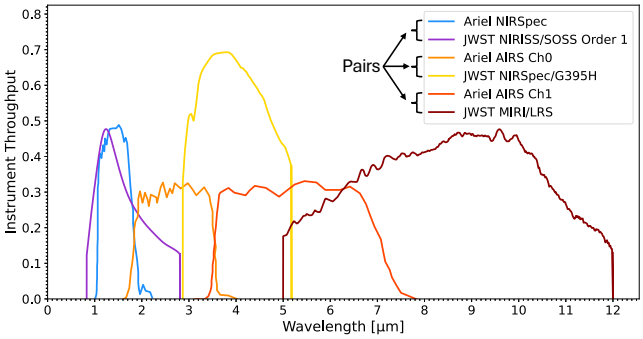

Figure 1. *JWST* versus *Ariel* spectrograph bandwidths and throughputs, obtained from D. Grant & H. R. Wakeford (2024) and L. V. Mugnai et al. (2020), respectively.

HD 209458b, we adopt system parameters from the *JWST* NIRCam analysis presented in Q. Xue et al. (2024). In order to inject the mapping signal into the simulated light curve, we take the input eclipse map from each original reference in units of F_p/F_* in `.npy` format and load it directly into the `starry` *planet* object. This effectively constructs a constant output star, a planet with the same spatial flux profile as the input map, and simulates the orbit and rotation of the planet and the resultant eclipse that would be observed by the original instrument, generating the desired simulated light curve.

Because the input maps are in units of F_p/F_* as observed by the original *JWST* spectrograph, when simulating the light curves as they would be observed by the equivalent *Ariel* spectrograph, we analytically rescale the relative flux values by multiplying through the flux ratios (*Ariel*/*JWST*) of the instruments. We analytically calculate the relative flux for each instrument using

$$\frac{F_p}{F_*} = \frac{I_p}{I_*}\left(\frac{R_p}{R_*}\right)^2, \tag{1}$$

where F is flux, I is intensity, and R is radius, with the subscripts p and $*$ denoting the planet and star, respectively. The intensity is calculated with a blackbody assumption using the Planck function as

$$I_\alpha = \frac{2hc^2}{\lambda_{\rm thr}^5 e^{\left(\frac{hc}{\lambda k_B T_\alpha}-1\right)}}, \tag{2}$$

where the wavelength-dependence, $\lambda_{\rm thr}$, carries our scaling between *JWST* and *Ariel*, and is weighted by the relevant instrument throughput. We use the equilibrium temperature of each test case for the planetary temperature, T_p, and the stellar effective temperature for T_*, again adopted from the relevant citation in Table 1. To additionally account for differences between the measured and analytically predicted *JWST* eclipse depth, we further take their ratio and multiply this through as a correction factor when scaling the *Ariel* flux.

For fairness of comparison, we adopt the same observing time and baseline distribution of the original *JWST* observations for our *Ariel* simulations. For HD 209458b, we assume a *JWST* comparison observation made up of one MIRI/LRS eclipse observation using a standard 1:1 baseline, with an additional hour pre-eclipse to account for the MIRI/LRS persistence ramp (A. Dyrek et al. 2024), and half an hour post-eclipse to emulate a scheduling window buffer.

To set the cadences and flux precisions of the *Ariel* simulated light curves, we use outputs from `ArielRad` (L. V. Mugnai et al. 2020), which is an end-to-end radiometric tool designed to simulate realistic *Ariel* observations. `ArielRad` provides the saturation time within every wavelength channel of a given spectrograph for a given target. We adopt the minimum saturation time across the channels of a given spectrograph for a given target as the cadence of our simulated observations in order to ensure that there is no saturation across the entire wavelength range. We then calculate the native flux error from `ArielRad` using this cadence in order to derive the precision of our simulated light curve (i.e. the flux error on each data point).

However, due to *Ariel*'s smaller collecting area compared to *JWST* (1 m versus 6.5 m diameter mirror; R. T. Zellem et al. 2019), the saturation times can run into the tens of minutes, which leads to poor spatial sampling of the dayside. R. C. Challener & E. Rauscher (2023) numerically determined that a 16/16 sampling rate of ingress/egress (32 in total) is sufficient to scan over all spatial signals up to fourth spherical harmonic degree. To facilitate eclipse mapping with *Ariel*, we therefore introduce a decision loop into our calculations that if the saturation time is short enough to provide $\geq$32 samplings of ingress/egress, then we adopt it as the cadence (true for our bright HD test cases). If the saturation time is longer than this (true for our dimmer WASP test cases), then we adopt a cadence such that the criterion of 32 samplings of ingress/egress is achieved, and rescale our flux precision accordingly by substituting this value back into `ArielRad`.

When simulating stacking additional *Ariel* observations, we rescale the flux precision as $\sqrt{N}$ the number of observations following a first-order photon noise approximation. In doing so, we adopt a noise floor of 10 ppm, as set by L. V. Mugnai et al. (2020), to prevent the flux precision from scaling down indefinitely.

2.2 Mapping framework

To extract the mapping signal from the simulated light curves and construct eclipse maps from them, we use the eclipse mapping software `ThERESA` (R. C. Challener & E. Rauscher 2022). Here, we briefly summarize the methodology of `ThERESA`, and refer the reader to R. C. Challener & E. Rauscher (2022) for further details.

To construct an eclipse map, one fits to signals in the light curve during ingress/egress which correspond to deviations from the occultation of a uniformly emitting planet, and converts them to the brightness pattern to which they correspond. To do this, one therefore requires a set of basis light curves which are translatable to basis maps. A natural formulation for this is spherical harmonics, as was first adopted for exoplanet eclipse mapping (C. Majeau et al. 2012; J. Wit et al. 2012). However, pure spherical harmonic mapping suffers from degeneracies in that while the set of basis maps themselves are orthogonal and thus independent of one another, their corresponding basis light curves are not. This means that the same feature in the light curve can be produced by an ensemble of different basis map configurations, leading to signal degeneracy complications which inhibit definitive mapping solutions.

The problem here can be attributed to the fact that the orthogonality of the modelling basis is located on the output side (i.e. the maps) rather than the observable side (i.e. the light curve). E. Rauscher et al. (2018) therefore proposed the method of 'eigenmapping' in order to overcome such signal degeneracies by inverting the order of the orthogonality. By performing principal component analysis (PCA) on the spherical harmonic basis, this method transforms it to a new basis in which the basis light curves ('eigencurves') are now the ones that are orthogonal to one another. This facilitates unique mapping solutions to each light-curve signal using the newly created 'eigenmaps', overcoming the signal degeneracy complication. This is the modelling framework that `ThERESA` adopts.

`ThERESA` optimizes for spherical harmonic degree, $l_{\rm max}$ and number of components, N, selecting the appropriate model complexity based on the information content of the data via the Bayesian Information Criterion (BIC; A. E. Raftery 1995). We use the notation LXNX to refer to our eigenmapping models, which denotes the maximum spherical harmonic degree used in the eigenbasis input (LX), and the number of eigenmap components used to construct the overall eclipse map (NX).

`ThERESA` ranks the eigenmaps in terms of their observability, fitting the most observable signals first. The NX of a model therefore denotes its complexity. In general, the first (N1) eigenmap corresponds to a day–night temperature contrast; the second (N2) eigenmap to an east–west hotspot offset; the third (N3) to north–south brightness patterns; and higher order (N4+) maps to smaller scale patterns from less dominant atmospheric dynamics, such as the magnetic drag effects in the WASP-18b eclipse map (L.-P. Coulombe et al. 2023). Hence, only models with N3+ can contain any latitudinal structure.

Since the modelling framework is built on spherical harmonics, the derived mapping model will naturally extend over the entire sphere of the planet. However, `ThERESA` uses a visibility function to calculate which longitudes of the planet were scanned over during the observation, which may extend beyond the dayside due to the rotation of the planet during the observation. It is only in these observed regions that the model is in fact data-driven, and so we only plot our maps and infer constraints over these regions.

The maps are finally converted from relative flux units to brightness temperature, weighted by the instrument throughput and calculated per pixel of the user-set resolution of the eclipse map (we elect to use $48_{\rm lon} \times 24_{\rm lat}$ pixels for runtime efficiency). We model the stellar flux using Phoenix models (T.-O. Husser et al. 2013) with stellar parameters adopted from the original reference (see Table 1) for each test case [using Q. Xue et al. (2024) again for HD 209458b]. Phoenix models were used in the original analysis for all of the test cases other than WASP-18b, where the star was modelled as a blackbody; for ease of comparison with the original work, we therefore model it the same way here. To prevent non-physical solutions, `ThERESA` enforces a physicality constraint that the flux in every cell must be greater than zero. This constraint is not enforced on the regions of the planet not scanned over during the observation.

2.3 Verification of the *JWST* inputs

To first verify that our simulation-and-retrieval framework yields both quantitatively and qualitatively equivalent maps as were injected, we first post-process these input maps into simulated versions of the *JWST* light curves originally used to derive them, and test that we recover the same map. For HD 209458b, we simulate the light-curve flux precision and cadence using `PandExo` (N. E. Batalha et al. 2017), and adopt the same baseline as described in Section 2.1.

Since any attempt to simulate *Ariel* systematics would be an approximation prior to commissioning tests conducted in space following launch, we elect to conduct our simulations with no

Table 2. Comparison of the literature parameters of the test cases versus those we recover from our simulation-and-retrieval framework. We quote the median dayside temperature, in addition to the temperature range across the observed regions of the planet in square brackets. We list the longitudinal hotspot offset for each test case, with the latitudinal hotspot offset below if one was measured (only true in the case of WASP-43b).

		Literature			Simulations		
Planet	Observation	Model	Hotspot (deg)	$T_{\rm Bright}$ (K)	Model	Hotspot (deg)	$T_{\rm Bright}$ (K)
HD 189733b	2 MIRI/LRS Eclipses	L5N2	$33.0^{+2.3}_{-2.5}$[a]	1210 [1000 − 1330]	L5N2	33.7 ± 3.1	1200 ± 10 [1010 − 1320]
HD 209458b	1 MIRI/LRS Eclipse (GCM)	/	48.8	1480 [1150 − 1600]	L5N2	$54.3^{+6.2}_{-6.1}$	1430 ± 20 [1240 − 1570]
WASP-18b	1 NIRISS/SOSS Eclipse	L5N5	$\sim -40 - 40$[b]	2900 [1250 − 3100]	L5N5	$\sim -40 - 40$[a]	2860 ± 40 [1250 − 3140]
WASP-17b	1 MIRI/LRS Eclipse	L2N2	$18.7^{+11.1}_{-3.8}$	1600 [600 − 2170]	L2N2	$18.1^{+8.5}_{-1.1}$	1600 ± 60 [600 − 2180]
WASP-43b (Hammond+24)	1 MIRI/LRS Phase Curve	L2N6[c]	7.8 ± 0.4 $-10.7^{+4.1}_{-4.7}$	1530 [750 − 1790]	L2N6	$6.6^{+0.4}_{-0.5}$ $-14.3^{+9.8}_{-8.5}$	1520 ± 50 [730 − 1760]
WASP-43b (Challener+24)	1 NIRSpec/G395H Phase Curve	L3N6	6.9 ± 0.5 $-13.4^{+3.2}_{-1.7}$	1640 [710 − 1975]	L3N6	7.2 ± 0.3 $-12.6^{+2.4}_{-1.7}$	1630 ± 25 [720 − 1950]

Notes. [a]We quote the median value derived from the canonical analysis, which used both the *JWST* and *Spitzer* data, but the uncertainties from only fitting the *JWST* data for fairer comparison to our simulation.
[b]No significant hotspot offset was measured for WASP-18b, but rather a brightness plateau around the substellar point – we therefore instead note the ranges of this plateau here.
[c]The canonical analysis of this data used spherical harmonic mapping, but a secondary eigenmapping analysis with `ThERESA` was also conducted; that model is stated here for comparison, but the other values and input map are from the primary analysis.

injected systematic signal. These *JWST* simulations therefore give us a fairer set of maps against which to eventually compare our *Ariel* simulations, since they remove any systematic biases (E. Schlawin et al. 2023) between the original work and our framework, in addition to any potential modelling biases.

We tabulate the results of our *JWST* simulations, including the mapping models, temperatures, and hotspot offsets, against those of the literature values in Table 2. No literature mapping model is listed for HD 209458b as this is a GCM output, not a data-derived *JWST* eclipse map (see Section 2 for details). We note that the temperature ranges quoted in the square brackets are only defined over the longitudes that were visible during the observation; whilst our models naturally extend over the entire planet, they are not data-validated over these unobserved longitudes, and hence we do not place constraints on nor plot them. The median temperatures quoted are only defined across the dayside longitudes (i.e. between $\pm 90^{\circ}$), since these are the regions most formally constrained by eclipse maps. This also enables more intuitive interpretation for cases where a significant portion of the nightside is observed. These median dayside temperatures are weighted by the cosine squared of the latitudes to account for the decreasing emitting area and reduced viewing geometry.

We find that for each of our test cases, we recover the same mapping model from our simulations as was derived in the original analyses, indicating that the mapping signal is being correctly injected. Below, we discuss the consistency of our simulation-retrieved hotspot offsets and temperatures with the literature values.

2.3.1 *Hotspots*

In general, our simulation-recovered hotspots are all within 1σ of the literature values, with similar magnitude uncertainties consistent with random scatter. The only notable discrepancy is in the case of the WASP-43b MIRI/LRS map (M. Hammond et al. 2024), for which the longitudinal hotspot offset is only consistent to within 2σ, and the uncertainty on the latitudinal hotspot offset is $\sim 2\times$ larger in our simulation.

Both of these can be attributed to the differing modelling framework we employ compared to the original analysis; this is the only test case where spherical harmonic mapping rather than eigenmapping was used to derive the input map. A secondary eigenmapping analysis with `ThERESA` was carried out in that work, and our longitudinal hotspot offset is in fact 1σ consistent with that map. Fig. 5 of M. Hammond et al. (2024) also shows that the eigenmapping analysis derived a less-constrained latitudinal profile, consistent with what we recover here. Since we will also use `ThERESA` to model the Ariel simulations, this modelling bias is therefore removed by adopting this simulated *JWST* result as our comparison case. We also note that the discrepancies between the models are largely exacerbated by the small uncertainties on the hotspot offset in this case, which is driven by the inclusion of the full phase curve signal in the map; morphologically, the maps are essentially identical, and yielded identical inferences on the atmospheric dynamics (M. Hammond et al. 2024).

For WASP-17b, we conversely recover slightly smaller uncertainties on the hotspot offset from our simulation than was originally derived. This can be attributed to the lack of systematics in the simulated light curve; the original MIRI/LRS eclipse observation of WASP-17b (D. Valentine et al. 2024b) showed a large magnitude persistence ramp of a morphology similar to that of the phase signal associated with the hotspot offset, leading to degeneracies between these two parameters. This effect was more significant than has been observed for most other *JWST* MIRI/LRS observations, which tend to show a faster decaying and oppositely oriented ramp in the white light curve (e.g. D. Grant et al. 2023; T. J. Bell et al. 2024), leading to a larger degeneracy for the WASP-17b eclipse map. The systematic-free nature of our simulation breaks this degeneracy and results in a better constrained hotspot offset.

Both of these examples support our decision to remove both modelling- and systematic-dependencies from our test cases in order for fairer eventual comparison to our *Ariel* simulations. Hence, we conclude that our recovered hotspot offsets are consistent with the literature values, indicating that the mapping signal is being correctly injected into the light curves.

2.3.2 *Temperatures*

In order to compare to 'literature' temperature values for HD 209458b, the map of which is post-processed from a GCM, we use the `utils.fmap_to_map()` functionality of `ThERESA` to convert

Table 3. *JWST* versus *Ariel* test case results. We outline the results of our *Ariel* simulations, in particular the recovered models, hotspot offsets, and temperatures, as a function of the number and type of observations required in order to derive them. For ease of comparison, we also re-tabulate our simulated *JWST* results from Table 2. In the case of WASP-43b, we first list the longitudinal and then the latitudinal hotspot offset below. Temperatures are quoted over the regions of the planet visible during the observation in square brackets, alongside the median dayside temperature and uncertainty.

	JWST				*Ariel*			
Planet	Observation	Model	Hotspot (deg)	$T_{\rm Bright}$ (K)	Observation	Model	Hotspot (deg)	$T_{\rm Bright}$ (K)
HD 189733b	2 MIRI/LRS Eclipses	L5N2	33.7 ± 3.1	1200 ± 10 [1010 − 1320]	2 AIRS Ch1 Eclipses	L5N2	$31.5^{+4.2}_{-6.3}$	1210 ± 20 [1050 − 1290]
HD 209458b	1 MIRI/LRS Eclipse (GCM)	L5N2	$54.3^{+6.2}_{-6.1}$	1430±20 [1240 − 1570]	1 AIRS Ch1 Eclipse	L5N2	$58.2^{+20.8}_{-20.6}$	1400 ± 50 [1280 − 1510]
WASP-18b	1 NIRISS/SOSS Eclipse	L5N5	∼−40−40	2860 ± 40 [1250 − 3140]	3 Ariel NIRSpec Eclipses	L5N5	∼−40−40	2890 ± 40 [1270 − 3130]
WASP-17b	1 MIRI/LRS Eclipse	L2N2	$18.1^{+8.5}_{-1.1}$	1600 ± 60 [600 − 2180]	5 AIRS Ch1 Eclipses	L2N2	$33.7^{+38.7}_{-21.9}$	1675 ± 180 [1250 − 2000]
					20 AIRS Ch1 Eclipses	L2N2	$24.6^{+12.3}_{-7.8}$	1650 ± 100 [1050 − 2050]
					1 AIRS Ch1 Phase Curve	L2N4	$18.7^{+1.2}_{-3.0}$	1620 ± 30 [700 − 2100]
WASP-43b (Hammond+24)	1 MIRI/LRS Phase Curve	L2N6	$6.6^{+0.4}_{-0.5}$ $-14.3^{+9.8}_{-8.5}$	1520 ± 50 [730 − 1760]	1 AIRS Ch1 Phase Curve	L2N4	10.9 ± 0.8 /	1530 ± 50 [800 − 1700]
					18 AIRS Ch1 Phase Curves	L2N6	$6.9^{+0.5}_{-0.7}$ $-11.8^{+8.2}_{-9.6}$	1510 ± 50 [800 − 1720]
					18 AIRS Ch1 Eclipses	L2N2	9.6 ± 1.0 /	1520 ± 15 [950 − 1720]
WASP-43b (Challener+24)	1 NIRSpec/G395H Phase Curve	L3N6	7.2 ± 0.3 $-12.6^{+2.4}_{-1.7}$	1630 ± 25 [720 − 1950]	1 AIRS Ch0 Phase Curve	L3N4	$11.3^{+0.7}_{-0.6}$ /	1640 ± 25 [750 − 1950]
					18 AIRS Ch0 Phase Curves	L3N6	$6.5^{+0.5}_{-0.6}$ $-14.1^{+2.1}_{-2.2}$	1650 ± 25 [730 − 1950]
					18 AIRS Ch0 Eclipses	L3N2	10.9 ± 1.0 /	1640 ± 10 [950 − 1950]

the GCM flux map to brightness temperature, using a Phoenix model (T.-O. Husser et al. 2013) with stellar parameters from Q. Xue et al. (2024) to model the stellar flux. For our data-derived test cases, we compare directly to the literature values.

As in the case of the hotspot offsets, we find that our simulation-recovered temperatures are also largely consistent with the literature values (see Table 2). We do not quote uncertainties on the literature values here they are not quoted in all cases, and not comparative for the GCM-derived map of HD 209458b. The only notable discrepancy between the literature-and-simulation temperatures is in the case of HD 209458b, for which the limb temperatures are recovered to be ∼ 100 K hotter than the input map, whilst the median dayside temperature is recovered slightly too cold.

There are complexities between directly comparing a GCM map and a data-derived eclipse map, which can appear to be different but in reality be consistent; for further details, see R. C. Challener & E. Rauscher (2023). However, we were able to show that these differences can be attributed to this map having the largest hotspot offset with the most extended profile. Hence, in the most reliable central-longitudes region of the map, from which the day–night contrast is largely derived, the temperature gradient is observed to be quite small, and the sharper drop-off to the limbs is missed. We tested this theory by extending the observation to a full phase curve in order to more accurately measure the limb temperatures, and found that the day–night gradient was more successfully recovered in this case, in addition to producing a more consistent median dayside temperature. For a map derived from an eclipse-only observation, these discrepant limb temperatures are of least concern because they are largely unconstrained due to being only momentarily observed and not optimally viewed. However, we recommend that for a data-derived eclipse map of HD 209 458 with *JWST*, a long baseline would be advisory in order to account for this large hotspot offset.

In all other cases, the recovered temperatures from these *JWST* simulations are consistent with the input maps within the uncertainties. Coupled with the consistent hotspot offsets, this validates that the mapping signal is being correctly injected. We therefore now proceed to construct our Ariel simulations.

3 ARIEL TEST CASE SIMULATIONS

Here, we inject our test case eclipse maps into simulated *Ariel* light curves. We then retrieve on these simulated light curves using `ThERESA`, seeking to recover the same eclipse mapping model, LXNX, that we recover from our *JWST* simulations (Table 2). If the number of observations is insufficient to recover the input map, then we simulate stacking additional *Ariel* observations by scaling the flux precision by $\sqrt{N}$ the number of observations (up to a noise floor of 10 ppm) until we recover the input model.

Our primary goal is to test the data quantity required by *Ariel* in order to derive the same qualitative mapping model as *JWST*, and then compare the quantitative inferences that are derivable from those maps between the observatories. In the following subsections, we outline the results of our test cases, and the primary conclusion that we draw from each. We tabulate the comparisons between *JWST* and Ariel in Table 3.

3.1 HD 189733b and HD 209458b

HD 189733b and HD 209458b are the two canonical hot Jupiters which paved the way for many advancements in the field as a result

of their system brightness and therefore high data quality (e.g. D. Charbonneau et al. 2000; T. M. Brown et al. 2001; F. Bouchy et al. 2005; D. Deming et al. 2006, 2013; H. A. Knutson et al. 2007, 2012; A. P. Showman et al. 2008; D. K. Sing et al. 2011; C. Majeau et al. 2012; J. Wit et al. 2012; R. T. Zellem et al. 2014; E. Flowers et al. 2019; B. M. Kilpatrick et al. 2020; J. Inglis et al. 2024; Q. Xue et al. 2024). As such, much of our theoretical understanding and modelling frameworks are based upon these targets. They are two of the highest ranking targets in terms of their EMM (S. Boone et al. 2024). Hence, they are the natural first test cases for a study such as this.

3.1.1 HD 189733b

HD 189733b is the planet with the overall highest EMM (S. Boone et al. 2024), with its best value for MIRI/LRS. This is therefore our fundamental test case; an observatory with baseline eclipse mapping capabilities should be capable of eclipse mapping it in the mid-infrared, as *Spitzer* was capable of doing (C. Majeau et al. 2012; J. Wit et al. 2012). The input *JWST* MIRI/LRS map (M. Lally et al. 2025) is a two-component (N2) model, broadly corresponding to a day–night temperature contrast and longitudinal hotspot offset, with no constrained latitudinal structure. We take this input map and post-process it into an *Ariel* AIRS Ch1 light curve, our MIRI/LRS equivalent, using the methods outlined in Section 2.1.

Since our *JWST* reference case was produced using two *JWST* MIRI/LRS eclipses, we compare to what we would recover using two *Ariel* AIRS Ch1 eclipses by scaling our flux uncertainties down by $\sqrt{2}$. We list our recovered model, hotspot location, and temperatures in Table 3. We find that with the same amount of data as *JWST*, *Ariel* is able to recover the input mapping model, proving that it has, at minimum, baseline eclipse mapping capabilities. We also note that, the same as *JWST*, *Ariel* can also map HD 189733b using only a single eclipse observation, but we discuss the results of our two-eclipse example here for fairness of comparison to the results of M. Lally et al. (2025).

Fig. 2 shows our simulation-recovered *JWST* map on the left, *Ariel* map in the middle, and difference map (*JWST*−*Ariel*) on the right, with flux profiles plotted above to give a sense of the temperature constraints as a function of longitude. The difference plot reveals any structural differences between the *JWST* and *Ariel* maps. For identical maps, the difference map and flux profile would be flat, and the differenced hotspot would be located at the substellar point. The uncertainties quoted on the differenced hotspot are the sum of the *JWST* and *Ariel* uncertainties, whilst for the differenced flux profile, we sum the uncertainties in quadrature.

We plot the maps in absolute temperature units since we rescale the *Ariel* values from the *JWST* ones using a blackbody assumption therefore we expect to recover comparable temperatures. The measured flux, on the other hand, will differ due to the different wavelengths of the spectrographs therefore we plot the differenced flux profile in relative units.

These plots show that overall, we recover a highly consistent thermal structure between *JWST* and *Ariel* for this test case. However, the AIRS Ch1 spans a slightly narrower temperature range than the MIRI/LRS map, leading to a slightly shallower day–night temperature gradient. This is consistent with theoretical expectations: AIRS Ch1 spans a narrower bandwidth than MIRI/LRS, and therefore samples less of the planet's spectral energy distribution.

In Fig. 3, we show the posteriors of our recovered longitudinal hotspot offsets between the observatories. The overlap between the posteriors, and the fact that the difference map in Fig. 2 shows a differenced hotspot offset consistent with zero, demonstrates that we accurately recover the injected hotspot offset with *Ariel*, and at only $\sim 2\times$ lower precision than *JWST*.

The flux profiles above the maps are highly consistent in terms of both morphology and precision, with *Ariel* tightly constraining the flux and thus temperature distribution of the central longitudes in a manner comparable to *JWST*. In total, *Ariel* achieves a median temperature precision of 20 K across the dayside, compared to the 10 K precision achieved with *JWST*.

The precision achieved on both the recovered hotspot and dayside temperature is encouraging, and can likely be attributed to the brightness of the HD 189 733 system. This results in fast saturation times for *JWST* due to its large collecting area, necessitating a <1 s cadence. Conversely, *Ariel*'s smaller collecting area allows it to expose for approximately twice as long, resulting in a comparable flux precision to *JWST*, but still with a short enough cadence to finely sample the dayside flux profile. This enables *Ariel* to rival *JWST* in terms of not only qualitative, but also quantitative mapping ability for brighter targets, using fewer observations than one would expect from a simple scaling of their collecting areas. This test case therefore gives promising indications of *Ariel*'s potential to eclipse map bright targets at high precision.

3.1.2 HD 209458b

HD 209458b is the planet with the second highest EMM for MIRI/LRS (S. Boone et al. 2024). However, no eclipse observations have yet been conducted with *JWST*. We therefore use a GCM output of the planet (M. Hammond & D. S. Abbot 2022) to inform our test case here (see Section 2 for details). Similar to our previous test case, our *JWST* reference map here is a two-component (N2) model with no constrained latitudinal structure. To test what we would recover with *Ariel*, we post-process this GCM output into an equivalent Ariel AIRS Ch1 light curve using the methods outlined in Section 2.1.

With this test case, we now benchmark *Ariel*'s eclipse mapping abilities versus those of *JWST* using only a single eclipse observation. We plot the *JWST*, *Ariel*, and difference maps for HD 209458b in Fig. 4, the longitudinal hotspot posteriors in Fig. 5, and tabulate these values in Table 3. We find that even this minimal amount of data is sufficient to recover the input mapping model. *Ariel*'s ability to map high-ranking *JWST* mapping targets using only single eclipse observations, compared to the eight required by *Spitzer* to map even the highest ranking target (C. Majeau et al. 2012; J. Wit et al. 2012), is encouraging for its future mapping prospects.

We once again derive a highly consistent thermal structure, as evidenced by the similar contour profiles and mostly flat difference map in Fig. 4. The residual structure in the latter is of the same origin as was found for the previous test case: a comparable spatial temperature profile, but over a narrower range for AIRS Ch1 compared to MIRI/LRS due to the narrower bandpass. This lends further credence to this effect being systemic rather than systematic. The median dayside temperature is constrained at 50 K by *Ariel* in this case, compared to 20 K for *JWST*. The hotspot posterior plot shows that *Ariel* accurately recovers the hotspot offset at 1σ agreement with the *JWST* value, and at only $\sim 3\times$ lower precision.

The quality of these constraints can again be attributed to the brightness of the system inhibiting *JWST*'s integrations times compared to *Ariel*'s, allowing the latter to increase its flux precision whilst still maintaining good spatial scanning. The relative precision on mapping parameters between *JWST* and *Ariel* is slightly lower here than in the previous test case because the HD 209 458 system is

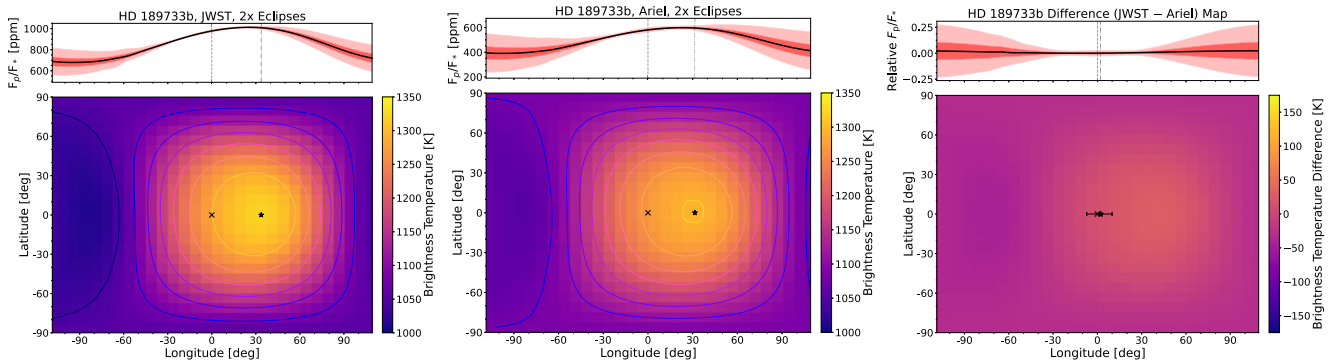

Figure 2. HD 189733b eclipse maps, with flux profiles shown above. The cross and dashed line mark the location of the substellar point, whilst the star and dash-dotted line mark the location of the hotspot. *Left:* Simulated version of the *JWST* MIRI/LRS map, derived from two eclipses (M. Lally et al. 2025). *Middle:* Equivalent *Ariel* AIRS Ch1 map, also derived from two eclipse observations. *Right:* Difference map (*JWST*−*Ariel*). The flat structure shows that we recover consistent thermal structures between the instruments, although with a slightly shallower day–night gradient for the latter as a consequence of its smaller bandwidth (see the text). The overlap of the differenced hotspot with the substellar point shows that we accurately and precisely recover this key parameter.

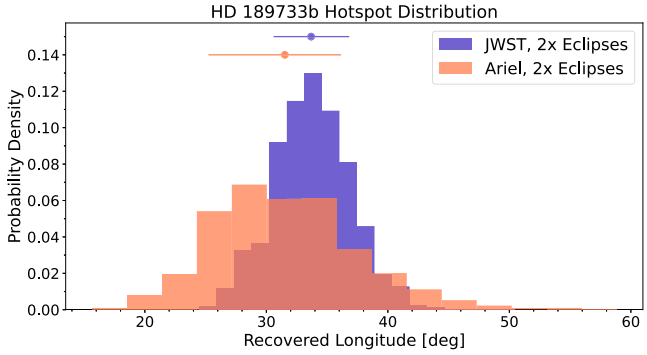

Figure 3. HD 189733b hotspot location posteriors. In blue is what we recover from the *JWST* MIRI/LRS map, and in orange what we recover from the *Ariel* AIRS Ch1 map. Using the same amount of data, *Ariel* is able to recover a highly consistent hotspot offset with uncertainties only $\sim 2\times$ as large as *JWST* for this bright target.

relatively dimmer, meaning that even with this longer cadence, *Ariel* is not able to rival *JWST*'s flux precision to the same degree. However, this $\sim 3\times$ scaling still exceeds first-order expectations for how one might expect the much smaller *Ariel* telescope to compare against *JWST*. This test case therefore further supports our prior conclusion that *Ariel* shows promising potential to map bright targets.

3.1.3 3D Mapping of HD 189733b and HD 209548b

Since *Ariel* simultaneously observes using all of its spectrographs, giving it inherent 3D mapping abilities, we also test its ability to map the atmospheres of these high-ranking mapping targets using its AIRS Ch0 and NIRSpec instruments. We rescale the input flux maps to the values that would be observed in the bandwidth and throughput of these instruments using the methods of Section 2.1, and retrieve on them with `ThERESA`. We find that we again recover the same input mapping model, with consistent thermal structure and 1σ consistent hotspot offsets as we find with our AIRS Ch1 examples.

Out of our *JWST* spectrographs of interest for eclipse mapping (see Table 1 and S. Boone et al. 2024), these two canonical hot Jupiters can only be mapped in the mid-IR, using MIRI/LRS, as they are too bright and saturate in NIRISS/SOSS and NIRSpec/G395H[2] *Ariel*'s lower collecting area means that it can observe these targets in the near-IR without saturating, allowing it map them across its entire wavelength range from 0.5 to 7.8 μm. Hence, for these two canonical hot Jupiters, *Ariel* is the only way to access and map these pressures, which is imperative if we are to build a full 3D picture of their atmospheres. This further adds to the need for another eclipse mapping observatory in order to provide synergy to what is achievable with *JWST*, and the advantages of using *Ariel* to do so.

Hence, the primary conclusion that we reach from these test cases is that *Ariel* has, at minimum, baseline-level eclipse mapping capabilities. Its ability to directly compete with *JWST* using the same amount of data for these highest ranking targets is a testament to the fact that *JWST* light curves are of a quality that far supersedes the threshold for eclipse mapping, at least for longitudinal signals of bright targets. In such cases, *Ariel* therefore does not need to directly match *JWST* light-curve quality in order to observe the same mapping signals. Hence, for bright, high-ranking mapping targets, *Ariel* light curves will have the precision necessary to measure eclipse maps in the same observational time as *JWST*.

3.2 WASP-18b

S. Boone et al. (2024) rank the top 15-to-16 eclipse mapping targets for *JWST*. WASP-18b is the target that achieves the lowest numeric score, placing 16th in the NIRISS/SOSS ranking. We showed in the previous subsection that our 'best of the best' test cases are mappable using as little as single eclipse observations with *Ariel*. We now assess how well *Ariel* performs for our 'worst of the best' test case. We take the input WASP-18b map, derived from a single *JWST* NIRISS/SOSS eclipse (L.-P. Coulombe et al. 2023), and post-process it into an equivalent *Ariel* NIRSpec light curve using the methods outlined in Section 2.1.

The input map in this case is a higher order L5N5 model,[3] which, as evident in the left panel of Fig. 6, contains a degree of complex, small-scale structure that we seek to replicate with *Ariel*. There is no hotspot offset to compare in this case because

[2]We note that HD 189733b only partially saturates in NIRSpec/G395H, but this is still using only two groups per integration.
[3]We note that an L2N5 model was only slightly less preferred and formally statistically indistinguishable (L.-P. Coulombe et al. 2023).

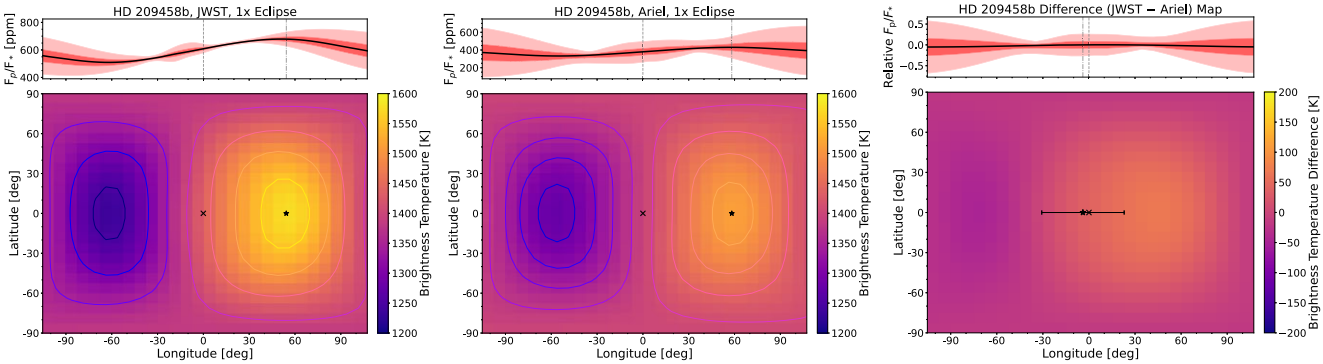

Figure 4. HD 209458b eclipse maps, with flux profiles shown above. The cross and dashed line mark the location of the substellar point; the star and dash-dotted line mark the location of the hotspot. *Left:* Simulated *JWST* MIRI/LRS map, derived from a single eclipse observation post-processed from a GCM of the planet (M. Hammond & D. S. Abbot 2022, see Section 2 for details). *Middle:* Equivalent *Ariel* AIRS Ch1 map, also derived from a single eclipse observation. *Right:* Difference map (*JWST*−*Ariel*). The mostly flat structure shows that we accurately recover the *JWST* input map with *Ariel*, but with an expected shallower day–night gradient due to the smaller *Ariel* instrument bandwidth. The overlap of the differenced hotspot with the substellar point shows that we recover this key parameter to better than 1σ.

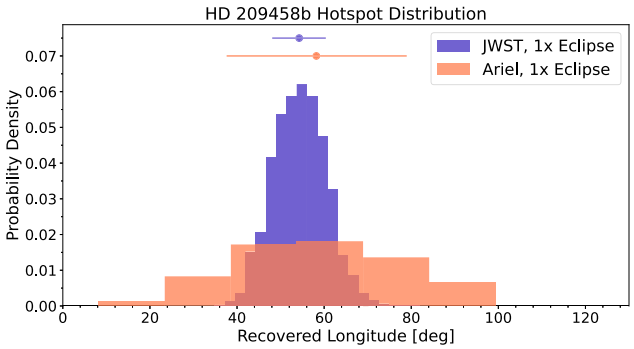

Figure 5. HD 209458b hotspot location posteriors. In blue is what we recover from the *JWST* MIRI/LRS map, and in orange what we recover from the *Ariel* AIRS Ch1 map. Using the same amount of data, and only a single eclipse observation at that, *Ariel* is able to recover a consistent hotspot offset as *JWST* with uncertainties only $\sim 3\times$ as large for this bright target.

WASP-18b, as an ultra-hot Jupiter, has a hotspot localized to the substellar point, a consequence of the much shorter radiative timescales preventing efficient advection of heat, and/or magnetic field interactions with the ionized flow imparting a strong drag (L.-P. Coulombe et al. 2023). However, the input eclipse map does have a distinctive overturning-morphology around the substellar region, with an approximately double-peaked brightness plateau extending between $\sim \pm 40^\circ$ longitude.

Given the lower EMM of this target, we find that in this case, *Ariel* requires more observations compared to *JWST* in order to recover the same mapping model. This is further exacerbated by the fact that the WASP-18 system is dimmer than our previous test cases, which results in long native saturation times for *Ariel*, and therefore a cadence that is too long for adequate spatial scanning of the dayside atmosphere. We therefore rescaled the cadence per the methods of Section 2.1 in order to maximize the spatial information content of the light curve, which necessarily leads to a reduced flux precision.

Despite this, we find that as few as three eclipse observations are sufficient in this case to accurately recover this high-order L5N5 model, as evidenced by the consistent contour profiles between the maps, and flat difference map in Fig. 6. The most notable differences are slight artefacts beyond the limbs, which the flux profiles show contribute negligible signal to the overall map and therefore are the most unconstrained.

The *Ariel* NIRSpec and *JWST* NIRISS/SOSS instruments have the most comparable wavelength coverage of our designated *Ariel*–*JWST* pairs. Consequently, we recover a highly consistent thermal structure between the maps, with near-identical temperature ranges and thermal gradients. In terms of precision, we find that with $3\times$ as many observations, *Ariel* is able to constrain the median dayside temperature to the same precision as *JWST*, at 40 K in both cases (see Table 3). The 2D profile is similarly well constrained, as evidenced by the similar magnitude flux profile uncertainties.

Whilst three eclipse observations may be difficult to request on the oversubscribed *JWST*, it is more than feasible for a dedicated exoplanet mission like *Ariel*, which can dedicate up to twenty observations for high-ranking targets in its census (B. Edwards & G. Tinetti 2022). This lends further credence to our prior conclusion: that *JWST* light curves far supersede the minimal quality required for eclipse mapping, therefore directly matching its data quality is not required in order to replicate its mapping capabilities. This validates *Ariel* as an observatory capable of deriving both qualitatively and quantitatively similar multidimensional mapping results as *JWST*, even for dimmer targets.

3.2.1 *Time sampling test*

Here, we test whether our simplifying assumption of fitting a single noise-scaled light curve yields the same results as jointly fitting separate light curves with slightly different time sampling, as would be obtained in reality. The time sampling of an observation is critical for eclipse mapping since it sets the spatial scanning of the atmosphere. Using our optimized cadence calculation detailed in Section 2.1, we find that for WASP-18b, cadences below 47 s maximize the spatial information content of the light curve. We therefore test shifting the additional observations by 10 s in either direction in order to provide a non-integer time sampling offset between the observations. From jointly fitting these light curves, we find that we are able to derive the same qualitative map with identical quantitative constraints as following $\sqrt{N}$ statistics.

We attribute this to our use of the optimized cadence when designing the *Ariel* light curves, meaning that no matter the placement of the data points, they each sample the spatial profile of the atmosphere

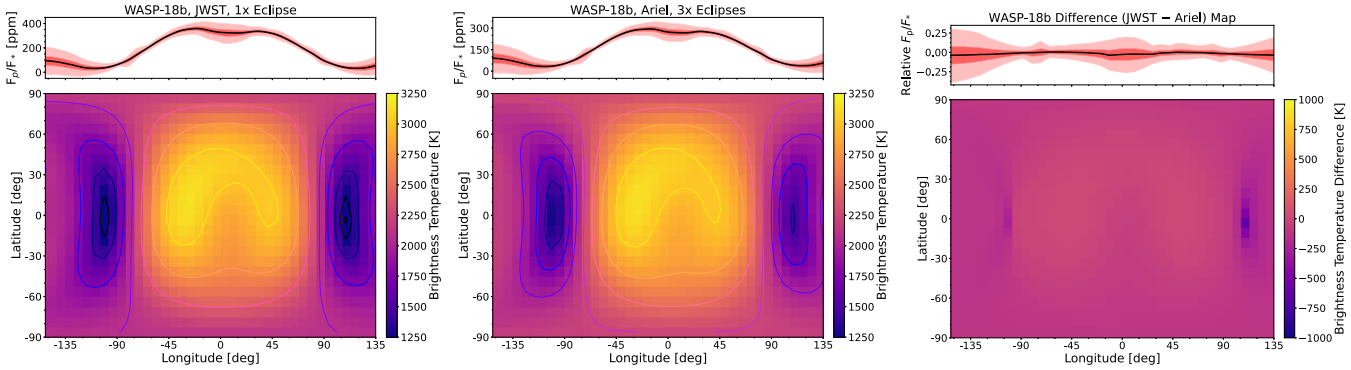

Figure 6. WASP-18b eclipse maps, with flux profiles shown above. *Left:* Simulated version of the *JWST* NIRISS/SOSS map, derived from one eclipse observation (L.-P. Coulombe et al. 2023). *Middle:* Equivalent *Ariel* NIRSpec map, derived from three eclipse observations. *Right:* Difference map (*JWST*−*Ariel*). The flat structure of the latter shows that with *Ariel*, we recover the thermal structure of the input map with high accuracy. The artefacts beyond the limbs are of least concern since, as the flux profiles show, they contribute negligible signal to the overall map.

at the maximum achievable resolution. This demonstrates that if the cadence of observations is optimized, then specific phase placements of the data points is not necessary to combine data sets and increase the signal-to-noise (SNR). By designing the observations in this way, *Ariel* will therefore have the ability to combine data sets in order to map lower ranking mapping targets.

The fact that *Ariel* can compete with *JWST* for both the 'best of the best' and the 'worst of the best' targets in the ranking of S. Boone et al. (2024), using a reasonable amount of data, indicates that *Ariel* will have the capability of mapping all of these highest ranking targets, of which there are 22 unique ones. This gives promising indications of *Ariel*'s potential to expand the parameter space of eclipse mappable data sets and facilitate population-level mapping studies at a faster rate than what is feasible with *JWST*.

3.3 WASP-17b

Despite being successfully eclipse mapped by *JWST* MIRI/LRS using only a single eclipse observation (D. Valentine et al. 2024b), WASP-17b does not rank amongst the top 15 targets for any of our *JWST* spectrographs of interest (S. Boone et al. 2024). Given that *Ariel* has shown the potential to map all of these high-ranking targets, we therefore elected to expand the analysis of S. Boone et al. (2024) in order to identify where WASP-17b falls (see Section 4.1 for further details). In the appendix, we tabulate the rankings of the 100 best eclipse mapping targets for *JWST* NIRISS/SOSS (Table B1), NIRSpec/G395H (Table B2), and MIRI/LRS (Table B3) that we derived in this way.

From this expanded analysis, we find that WASP-17b ranks as approximately the 100th best eclipse mapping target for *JWST* MIRI/LRS. Whilst it scores much higher in terms of longitudinal EMM (34th), a testament to the ability of D. Valentine et al. (2024b) to recover the longitudinal hotspot shift using only a single eclipse observation, its overall EMM is brought down by its poorer latitudinal ranking (167th), a consequence of WASP-17b's low impact parameter of 0.35. This explains why no latitudinal structure was recovered in the *JWST* eclipse map, with a lower order two-component (N2) model being preferred. This test case is therefore used to push *Ariel* to its limits by testing its ability to compete with *JWST* for a much dimmer and lower ranking mapping target. Below we detail four cases: (1) using five eclipses, (2) using 20 eclipses, (3) an extended baseline method, and (4) a full orbital phase curve.

3.3.1 *Five eclipses case*

We take the L2N2 MIRI/LRS map of WASP-17b from D. Valentine et al. (2024b), post-process it into an AIRS Ch1 light curve using the methods outlined in Section 2.1, and continue to scale the `ArielRad`-derived flux precision by $\sqrt{N}$ the number of observations until we recover the same model with *Ariel*. As a dimmer target, the native cadence of the observation was too long to finely sample the dayside flux profile. We therefore used the methods outlined in Section 2.1 to rescale the cadence to the maximal value that ensures adequate spatial scanning, and degraded the flux precision accordingly.

Despite this reduced flux precision, we find that, even for this dimmer, lower ranking target, the same mapping model is recoverable at statistical significance (ΔBIC $\gtrsim$10, A. E. Raftery 1995) using as few as five eclipse observations; this map is shown in the top row of Fig. 7. However, unlike the previous test cases, where the same atmospheric structure was recovered with similar constraints as the *JWST* map, this five-eclipse *Ariel* map fails to adequately constrain either the hotspot offset or temperature profile.

Whilst the median dayside temperature is recovered accurately, the contour profile in Fig. 7 shows that the 2D structure is inaccurate, and the overhead flux profile shows that it is largely unconstrained, with a median dayside uncertainty of 180 K. This leads to a discrepant and poorly constrained hotspot offset of $33.7^{+38.7}_{-21.9}{}^{\circ}$, the posterior of which is plotted in Fig. 8. The *Ariel* map also exhibits a much shallower day–night temperature gradient closer to 500 K than the steep 1000 K gradient of the *JWST* map. Whilst our previous test cases showed that we expect to recover a slightly shallower thermal profile with AIRS Ch1 than we do with MIRI/LRS, this level of discrepancy is too large to be explained by the different instrument bandwidths, and can rather be attributed to poor signal recovery.

Thus, despite *Ariel* recovering the correct mapping model, the map itself does not agree either qualitatively or quantitatively with the *JWST* map. This is converse to the WASP-18b case, where the threshold for signal identification also produced a map with similar quantitative constraints. This is because that model was much higher order therefore it necessitated precise constraints in order to correctly resolve the small-scale signals. The lower order WASP-17b map, on the other hand, means that whilst *Ariel* is able to recover these higher amplitude signals using only 5× as many observations, this does not necessarily mean that it is able to adequately constrain them.

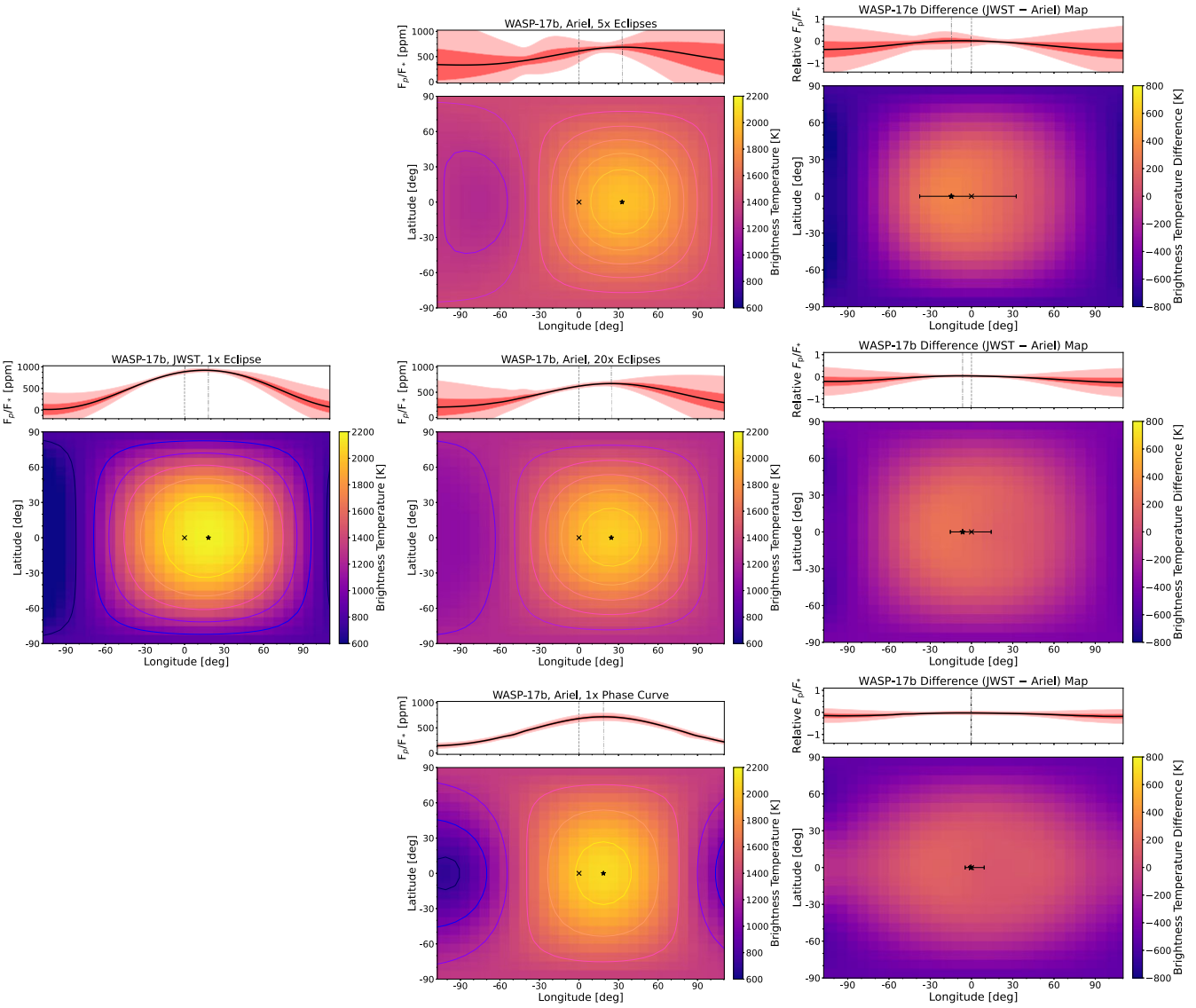

Figure 7. WASP-17b eclipse maps, with flux profiles shown above. The cross and dashed line mark the location of the substellar point; the star and dash-dotted line mark the location of the hotspot. *Left:* Simulated version of the *JWST* MIRI/LRS map, derived from one eclipse observation (D. Valentine et al. 2024b). *Middle:* Equivalent *Ariel* AIRS Ch1 maps, derived from (top) five eclipse observations (∼50 h), (middle) twenty eclipse observation (∼ 200 h), and (bottom) one phase curve (∼ 100 h). *Right:* Difference maps (*JWST*−*Ariel*). Moving down the rows, we better recover the input thermal structure, and improve both the precision and accuracy of the recovered parameters (temperature profile and hotspot offset) with *Ariel*. The use of a full or at least partial phase curve is the most time-efficient way for *Ariel* to recover the input map for this dimmer, lower ranking mapping target.

3.3.2 Twenty eclipses case

Due to the $\sqrt{N}$ scaling of photon noise, the greatest increase in light-curve SNR comes from the stacking of the first few observations: many more are needed beyond this to increase the SNR enough to make substantial improvements. In this case, even by increasing the number of eclipse observations to twenty, at the upper limit even for the highest ranking *Ariel* targets (B. Edwards & G. Tinetti 2022), *Ariel* is still unable to satisfactorily replicate the input map.

The hotspot offset, as evidenced by the posteriors in Fig. 8, is better constrained in this case, with a measured value of $24.6^{+12.3\circ}_{-7.8}$, but not to a satisfactory enough degree to warrant using 20× as many observations as is required with *JWST*. Similarly, the temperature profile (middle row of Fig. 7) is better constrained to a median dayside precision of 100 K, and yields a more consistent contour profile with a better constrained flux profile, but the day–night gradient is still not satisfactorily reproduced, as evidenced by the residual structure of the difference map.

We therefore conclude that *Ariel* is unable to adequately derive the input map for this lower ranking test case using a feasible number of repeated eclipse observations alone.

3.3.3 Extended baseline mapping

Instead of stacking more eclipses, which beyond N=20 would contribute less than 0.5 per cent improvement to the SNR of the light curve with each additional observation, we here test whether changes to the observing style may improve the constraints of the *Ariel* map.

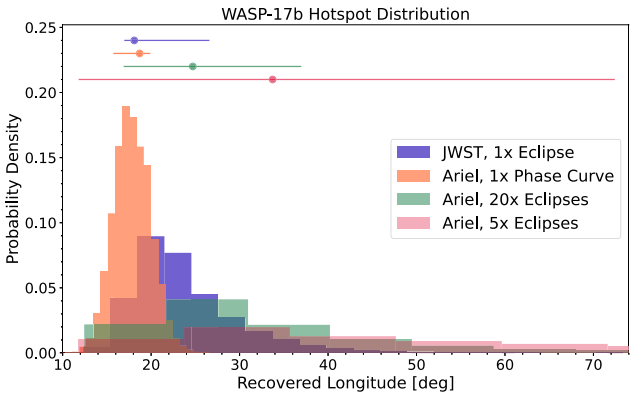

Figure 8. WASP-17b hotspot location posteriors. In blue is what we recover from the *JWST* MIRI/LRS map, and in red, green, and orange what we recover from the *Ariel* AIRS Ch1 maps derived from five eclipses, twenty eclipses, and one phase curve, respectively. Using eclipses only, we are unable to match the precision nor accuracy of the *JWST* map. Using a full phase curve, we recover the input hotspot offset with both high accuracy and precision.

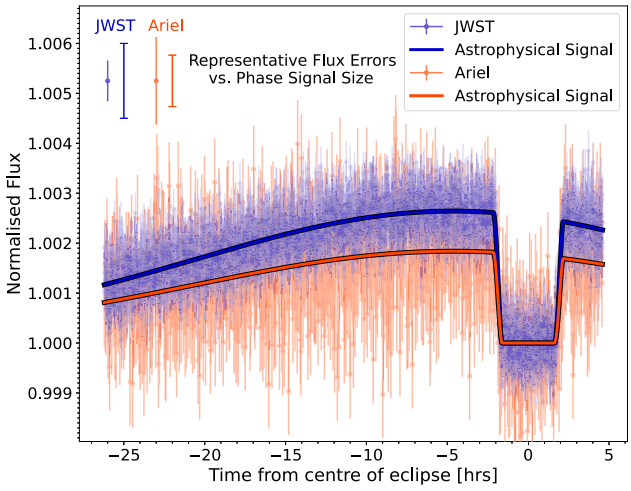

Figure 9. Partial phase curve of WASP-17b compared to the phase signal size, as observed using *JWST* MIRI/LRS compared to *Ariel* AIRS Ch1.

Phase mapping uses the shape of the phase curve to measure the hotspot offset and thermal profile, whilst eclipse mapping uses the shape of ingress/egress. These techniques therefore provide two distinct and independent measurements of these parameters. By extending the pre-eclipse baseline of the light curve to measure the peak of the phase curve, we can perform both of these measurements simultaneously via joint phase and eclipse mapping. This allows us to use the constraints of the former to anchor the constraints of the latter and alleviate signal-versus-noise degeneracies. This strategy is being utilized in *JWST* GO 5687 (D. Valentine et al. 2024a), and has shown successful application by combining a *Spitzer* partial phase curve with *JWST* eclipses of HD 189733b (M. Lally et al. 2025).

Whilst we only plot the regions of the planet visible during the observation, our models naturally extend over the entire planet. Whilst not formally valid over the unobserved regions because they are not data-driven, the nightside flux of these models are driven by the day-to-limb contrast of the eclipse map, and gives a first-order approximation of what we would expect to measure for the nightside. Hence, these models can be used to approximate full phase-curve observations, at least in the regime of simulations for an in-development observatory.

By extending our simulations to a full phase curve observation in this way, we find that the peak of the phase curve for WASP-17b using the D. Valentine et al. (2024b) input map falls approximately six hours before the start of eclipse. The *JWST* pre-eclipse baseline of three hours, which we also adopt for our *Ariel* simulated light curves, is therefore too short to measure this peak.

We first test extending the pre-eclipse baseline by 3×, to nine hours, in order to capture the location of this peak with a few hours of baseline either side to characterize its morphology. We find that we are now able to recover the mapping signal using only one observation, with a measured hotspot offset of $32.1^{+17.2}_{-12.4}$°. Whilst the accuracy is still lacking, the precision in this case is ∼ 2× better than the five standard baseline eclipse case that was required before to derive this signal previously, and achieved in one third of the time (15 versus 45 h, respectively). The same is true for the derived thermal profile, which is now much more consistent with the steep day–night gradient of the input map at order 1000 K, and constrained at a more comparable precision (75 K median dayside precision for *Ariel* compared to 60 K for *JWST*).

By further extending the pre-eclipse baseline, we find further improvement in the accuracy and precision of both the hotspot offset and the thermal profile. With a 6× pre-eclipse baseline extension (18 h, 24 total), we recover a hotspot offset of $22.6^{+2.6}_{-5.2}$° and $T_{\mathrm{day-night}}$ ∼1000 K with 50 K median dayside precision. With an 8× extension (24 h, 30 total), we recover a hotspot offset of $18.5^{+4.0}_{-3.9}$° and $T_{\mathrm{day-night}}$ ∼1000 K with 40 K median dayside precision. The latter is the example plotted in Fig. 9. With these baseline extensions, we now recover these key mapping parameters at even better precision than the standard baseline *JWST* eclipse (∼10 h), using only up to ∼ 3× as much observing time.

The amount of pre-eclipse baseline extension required is longer for *Ariel* than what is expected for *JWST* to successfully employ this strategy, with the GO 5687 programme finding from their simulations that only one to two additional hours prior to the phase curve peak were necessary in order to successfully characterize it. This reason for this is evidenced in Fig. 9, which shows that the phase signal is much more easily identifiable close to eclipse for *JWST* case than it is in for *Ariel*. This is partially a result of the larger amplitude of the phase signal due to the longer wavelengths and wider bandwidth of MIRI/LRS compared to AIRS Ch1, but primarily due to the higher native flux precision of *JWST* for dimmer targets.

Despite the longer baseline extension required, the time-efficiency gained compared to using repeated standard baseline eclipses still holds true. Even the minimal 5-eclipse case would require ∼50 h of observing time compared to ∼30 h for the scenario plotted in Fig. 9. Hence, the most time-efficient way for *Ariel* to map a large population of planets, which include dimmer, lower ranking mapping targets, is through the incorporation of phase information. The current *Ariel* strategy can dedicate up to twenty observations for high-ranking targets, and five for low-ranking targets (B. Edwards & G. Tinetti 2022). By comparing the observing times outlined above, we thus find that these extended-baseline observations are feasible.

However, there is no 'one strategy fits all' way of facilitating this observing style. The position of the peak of the phase curve will vary from target-to-target depending on the magnitude of the hotspot offset. HD 209458b, for example, with its much larger offset compared to WASP-17b, has a peak position ∼ 10−11 h prior to the beginning of eclipse (R. T. Zellem et al. 2014). Conversely, targets like CoRoT-2b have been observed to have westward hotspot offsets (L. Dang et al. 2018), meaning their peak in flux occurs

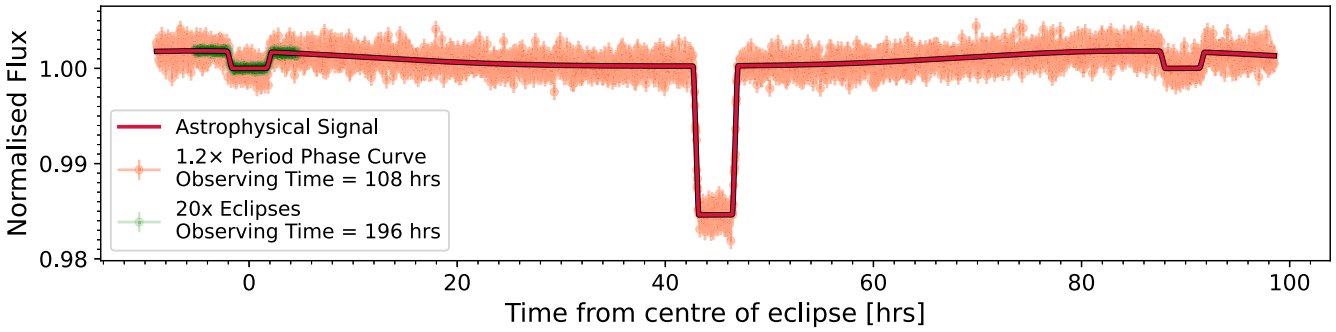

Figure 10. Proposed observing strategy to best facilitate mapping with *Ariel*. By observing 1.2×period phase curves, a number of benefits are gained (see Section 3.3.4) which allow *Ariel* to derive better mapping results using less observing time than is feasible by stacking repeat eclipse-only observations. We use our WASP-17b AIRS Ch1 test case for illustrative purposes here, where a phase curve of this nature (orange) is measurable in almost half the observing time required to measure 20 eclipse-only observations (green), and achieves better results.

post-eclipse, and therefore require a post-eclipse baseline extension instead. The brightness of the target and resultant flux precision will also determine how much baseline either side of the peak need be characterized in order to identify the phase signal and successfully apply this strategy, as Fig. 9 shows. Hence, the best way to facilitate this observing style for a large and diverse number of targets – and produce a uniform final data set, per the *Ariel* mission aims (G. Tinetti et al. 2018) – is to observe full phase curves of each target.

3.3.4 Full orbit phase curves

By designing these phase curves as being of observing length 1.2×period, centred on the transit with two eclipses bracketing the observation either side (see Fig. 10), we gain a number of advantages that would bolster *Ariel*'s mapping abilities. We outline these qualitatively below before going on to show its quantitative applications to WASP-17b.

(i) **Guarantee of signal characterization and data uniformity:** With a full-orbit phase curve, the peak is guaranteed to be observed with enough baseline to characterize its morphology no matter how far it is shifted from mid-eclipse. This enables us to anchor the large-scale longitudinal profile and break ingress/egress degeneracies, regardless of the magnitude or direction of the hotspot offset. This uniform observing strategy facilitates the holistic inferences that form the core of the *Ariel* mission aims (G. Tinetti et al. 2018).

(ii) **Precise system parameters:** The shape of the phase curve, including the transit, can be fit in order to improve our precision on key system parameters, which are unlikely to be known accurately for every target in such a large sample. High precision on system parameters, in particular the inclination and semimajor axis of the orbit, is imperative in order to correctly attribute the small-scale signals of eclipse mapping (R. C. Challener et al. 2024).

(iii) **Centre-of-transit time and ephemeris constraints:** The transit can further be used to accurately measure the centre-of-transit time and attribute centre-of-eclipse timing offsets to a mapping signal (I. Dobbs-Dixon, E. Agol & D. Deming 2015). Measuring a concurrent transit affords greater accuracy to do this (D. Valentine et al. 2024b), whereas ephemeris propagation from older observations has proved to hinder mapping efforts (E. Schlawin et al. 2024).

(iv) **SNR increase and variability calibration:** By observing two eclipses, we gain a $\sqrt{2}$ SNR improvement during ingress/egress, which increases the EMM of any given target (S. Boone et al. 2024). Conversely, any *changes* to the eclipse depth and/or shape would be indicative of short-term variability, whether that be astrophysical or systematic, and allow us to diagnose this and correct for it. This is much more challenging using individual observations due to calibration differences (M. Hammond et al. 2024; M. Lally et al. 2025).

(v) **Wealth of ancillary science:** Finally, whilst an eclipse baseline extension is helpful for eclipse mapping, it does not provide enough ancillary science to justify the cost for such a large sample size. With a full phase curve, on the other hand, a wealth of ancillary science becomes available. This includes our ability to map not only the dayside, but the *global* emission profile, in addition to facilitating other mapping techniques such as transmission mapping (D. Grant & H. R. Wakeford 2023).

In order to show the quantitative improvement gained by adopting this observing strategy, we finally test simulating and recovering on a 1.2×period phase curve *Ariel* observation of WASP-17b (shown in Fig. 10, compared to the 20-eclipse case from Section 3.3.2). The recovered map is shown in the bottom row of Fig. 7, and the hotspot posterior is shown in Fig. 8. With only this single observation now, the hotspot is the most accurately and precisely recovered at $18.7^{+1.2^\circ}_{-3.0}$. This high precision is primarily driven by the addition of the phase signal, with the measurement of the phase curve peak heavily anchoring this constraint. This demonstrates the advantages of combining phase and eclipse mapping information for deriving precise constraints on the atmospheric structure. We note that a four-component (N4) model is now required to fit the additional phase signal, but that the derived structure matches the complexity of the input N2 map derived from eclipse-only.

We also recover the input dayside temperature profile better than we could using a reasonable number of eclipses with *Ariel*, driven by our characterization of the shape of the phase curve. For ease of comparison, we only show the same longitudes for this map as those observed from the original eclipse-only observation timings, but note that such an observation would in fact produce a map of the global profile. The looser contour structure around the hotspot now much more closely resembles that of the input map, and the steeper day–night temperature contrast of order 1000 K is now successfully recovered compared to the eclipse-only Ariel maps, which erroneously indicate a more uniform dayside. The flux profile, and therefore so too the temperature profile, is also much more tightly constrained, with a median precision of 30 K across the dayside compared to 60 K for the *JWST* map.

The difference map shows that there are still some discrepancies at high latitudes, primarily at the limbs. These are primarily artefacts introduced by the higher order eigenmaps (N3+) required to fit

the phase signal. However, as previously discussed, latitudinal information is not constrained by phase maps, whilst the limbs are not tightly constrained by eclipse maps. Thus, when comparing eclipse-only maps versus phase-and-eclipse maps, close agreement is only expected in the equatorial latitudes of the central dayside longitudes. The difference map shows this to be true, with close, high-precision agreement between the *JWST* and *Ariel* maps here. The high-latitude discrepancies at the limbs are therefore of least concern, particularly since they contribute negligible flux to the overall map regardless.

Comparing between the best-case eclipse-only scenario, which required 20 observations, and this phase curve scenario, it is evident that the latter is the more efficient mapping strategy. In terms of time efficiency, ∼200 h of observing time would be required to observe 20 eclipses, without even accounting for the inordinate slewing and waiting time that these repeat observations would generate. The phase curve scenario, on the other hand, amounts to only ∼100 h. Without even factoring in time efficiency gained from only having to perform one observation, this is equivalent to only 10 standard-baseline eclipses, which is well within the limit of 20 for high-ranking *Ariel* targets like WASP-17b (B. Edwards & G. Tinetti 2022).

Hence, the primary conclusion of this test case is that *Ariel* also has the potential to map dimmer, lower ranking mapping targets, and that the most practical and efficient way to do this is through the use of phase curves. As such, we conclude at this point that *Ariel* is in fact capable of facilitating a population-level mapping survey.

3.4 WASP-43b

Here, we consider what parameters *Ariel* would be most suited to constraining with a population-level mapping survey. Our previous test cases have shown that *Ariel* is capable of mapping the longitudinal profile of targets spanning two orders of magnitude in EMM (S. Boone et al. 2024, and see Appendix). However, we have not yet tested *Ariel*'s ability to recover latitudinal signals.

Longitudinal signals are more observable for two reasons. First, they are present in the entire phase curve, whilst latitudinal signals are only measurable from ingress/egress. Secondly, the amplitude of longitudinal signals are inherently larger for tidally locked gas giants: the atmospheric dynamics tend to be dominated by rotational circulation regimes, resulting in substantial east–west hotspot offsets with large limb-to-limb temperature contrasts, whilst we expect a generally symmetric north–south profile with much shallower pole-to-pole temperature contrasts (M. Hammond & N. T. Lewis 2021; H. Beltz et al. 2022). For these reasons, the majority of *JWST* eclipse maps have not yet been able to robustly measure latitudinal signals (e.g. L.-P. Coulombe et al. 2023; D. Valentine et al. 2024b; M. Lally et al. 2025).

The MIRI/LRS eclipse map of WASP-43b constituted the first robust detection of the latitudinal profile of an exoplanet atmosphere (M. Hammond et al. 2024), with tentative indications of a latitudinal hotspot offset of $\sim 10^{\circ}$. This latitudinal offset was later confirmed with a 4σ detection in a NIRSpec/G395H eclipse map of WASP-43b; the detection of this signal was attributed as only being made possible by the exquisite data quality of *JWST* (R. C. Challener et al. 2024). We therefore use these final two test cases to determine the limits of Ariel's eclipse mapping abilities by assessing its ability to also recover this latitudinal signal.

The primary WASP-43b MIRI/LRS analysis was conducted using spherical harmonic mapping, but an alternative eigenmapping analysis was also conducted with `ThERESA`, yielding an L2N6 mapping model (M. Hammond et al. 2024). The large number of basis components required to fit this mapping signal is a testament to the data quality, resulting in a complex mapping profile with a high degree of asymmetric structure. A similar but higher degree L3N6 model was used to fit the mapping signal of the NIRSpec/G395H phase curve (R. C. Challener et al. 2024), yielding a similarly complex morphology which is consistent between the *JWST* instruments (see the top row of Fig. 11). Hence, we are also testing the synergy of different *Ariel* spectrographs with this test case by establishing whether they can similarly derive consistent morphologies. Such synergies are even more important for *Ariel* since it simultaneously measures with all of its instruments at once for every observation (G. Tinetti et al. 2018), facilitating inherent 3D mapping for every target.

3.4.1 *The latitude problem*

We post-process the *JWST* MIRI/LRS and NIRSpec/G395H maps of WASP-43b into *Ariel* AIRS Ch1 and Ch0 phase curves, respectively, using the methodology outlined in Section 2.1. The same as for our other WASP cases, the saturation times surpassed the maximal cadence for adequate spatial scanning of the dayside atmosphere for both spectrographs. We therefore rescaled the cadence per the methods of Section 2.1, thereby decreasing the flux precision of the light curves. Given the small-scale nature of latitudinal signals, it is perhaps then not surprising that with single observation *Ariel* phase curves, we are unable to recover these signals.

Whilst we recover a consistent temperature range (see Table 3), with the same median dayside precision achieved with *Ariel* as with *JWST*, we recover only four-component (N4) mapping models, with eastward hotspot offsets of $10.9 \pm 0.8^{\circ}$ and $11.3^{+0.7^{\circ}}_{-0.6}$ for AIRS Ch1 and Ch0, respectively. The same as in the WASP-17b phase curve case, an N4 mapping model corresponds to no constrained latitudinal structure for maps derived from full phase curves. Whilst these longitudinal hotspot offsets are discrepant from the eclipse mapping values due to the small uncertainties, they interestingly align with the prior phase-mapping only results of K. B. Stevenson et al. (2014) and M. M. Murphy et al. (2023), who find offsets of $12.3 \pm 1.0^{\circ}$ and $10.4 \pm 1.8^{\circ}$ from *HST*/WFC3 and *Spitzer*/IRAC phase curves, respectively.[4] R. C. Challener et al. (2024) also post-processed from their eclipse mapping posteriors the phase mapping-only value they would have measured (i.e. assuming no eclipse mapping signal), and found a similarly consistent phase-curve offset of $10.0 \pm 0.8^{\circ}$.

This discrepancy between hotspot offsets derived from phase maps versus eclipse maps signals is a known effect. R. C. Challener & E. Rauscher (2023) showed through numerical simulations that the values can differ due to the different observing methods used to derive them: as discussed in Section 3.3.3, phase mapping exploits hemispherically averaged rotational measurements and therefore constrains only large-scale, longitudinal structure, whereas eclipse mapping finely samples the dayside profile in both longitude and latitude. For WASP-17b, these two measurements (i.e. phase mapping versus eclipse mapping offsets) give equivalent results both in our simulations and the original data (D. Valentine et al. 2024b) because the eclipse map contains no small-scale or latitudinal structure. The WASP-43b maps, on the other hand, contain a degree of small-scale structure, and the high impact parameter of $b = 0.66$ (M. Hammond et al. 2024) means that the latitudinal structure is robustly measured. The phase mapping signal is blind to both this small-scale and latitudinal information therefore for higher order maps like these, the

[4]Note that hotspot offsets can differ as a function of pressure, but the high gravity of WASP-43b means that we expect to see similar offsets across all observable pressures for this planet (T. Kataria et al. 2015).

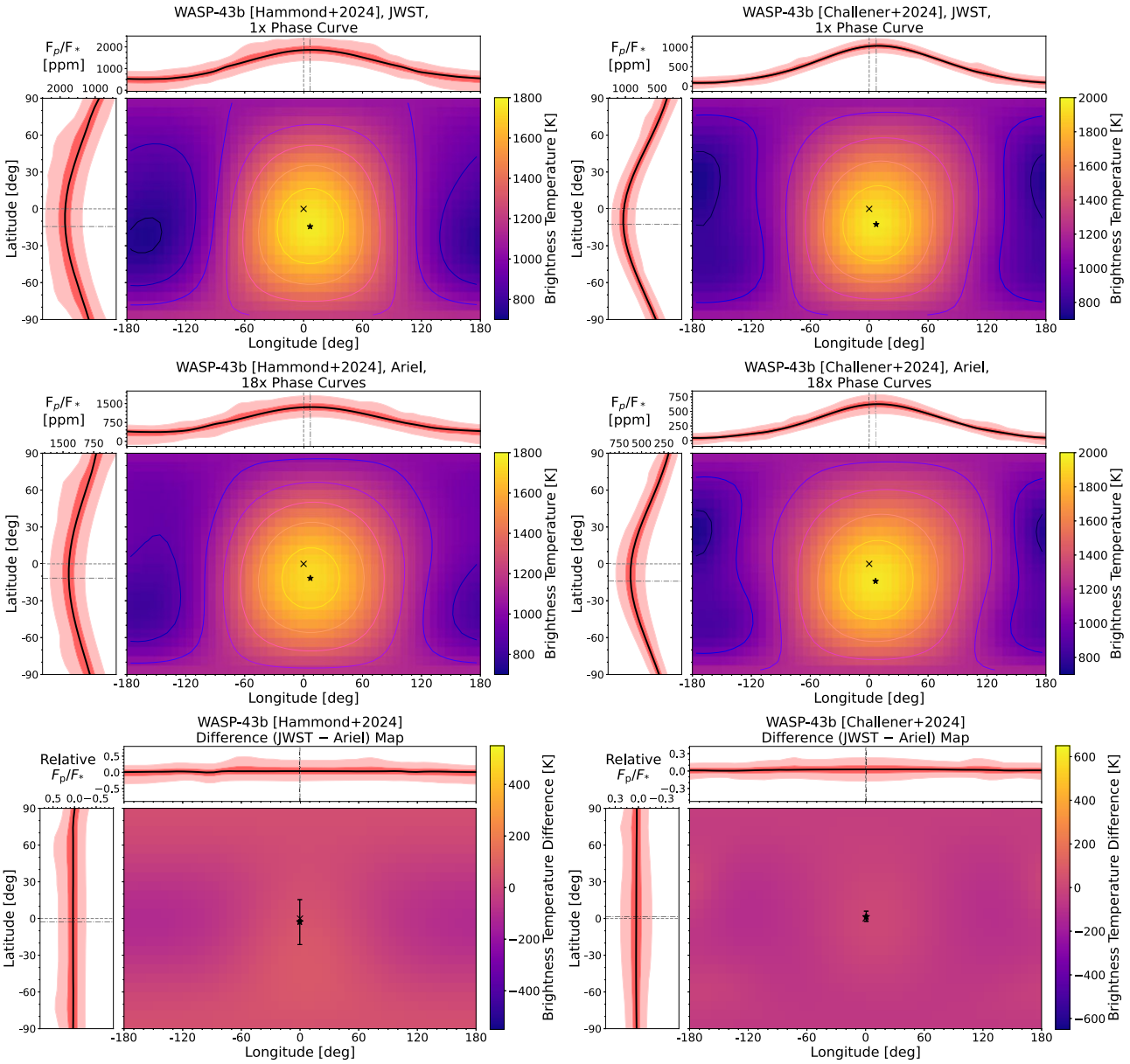

Figure 11. WASP-43b (*left:*) M. Hammond et al. (2024) and (*right:*) R. C. Challener et al. (2024) eclipse maps, with the longitudinal and latitudinal flux profiles shown above and on the left, respectively. The cross and dashed lines mark the location of the substellar point; the star and dash-dotted lines mark the location of the hotspot. *Top:* Simulated versions of the *JWST* (left) MIRI/LRS and (right) NIRSpec/G395H maps, derived from single phase curve observations. *Middle:* Equivalent *Ariel* AIRS Ch1 and Ch0 maps, respectively, each derived from 18 simulated phase curve observations. *Bottom:* Difference maps (*JWST*−*Ariel*). The flat structures show that we accurately recover the complex input profile in both cases. The overlap of the differenced hotspots with the substellar points show that we recover this parameter accurately in both longitude and latitude. However, latitudinal characterization with *Ariel* is incredibly time costly.

two methods may begin to diverge. As such, they no longer anchor each other as they did for WASP-17b, with the longer duration and higher amplitude phase mapping signal beginning to dominate.

We simulate increasing our number of phase curve observations in both bandpasses until we recover the higher component, latitudinally inclusive models. We find that in both cases, at least 10 repeated phase curve observations are required in order to recover the latitudinal signal, and that the exact number is dependent on the random scatter of the data, varying upwards to 25 repeat observations. The same mapping model and thermal structure is derived in each case, verifying that the astrophysical signal is indeed being correctly identified therefore the random scatter of the data is not affecting our ability to characterize the signal, but rather the noise threshold at which point we are able to resolve it.

The much higher data quantity required for *Ariel* to compete with *JWST* here can be attributed to the fact that, whilst *JWST* light curves far supersede the quality threshold for *longitudinal* eclipse mapping, they do not for *latitudinal* eclipse mapping, due to the inherently greater challenge of measuring the latter. Hence, we must stack far more *Ariel* observations in order to achieve the same latitudinal constraints as *JWST* compared to the number required to achieve the same longitudinal constraints.

The reason that the number of observations required is so heavily dependent on the random noise properties of the data is twofold. First,

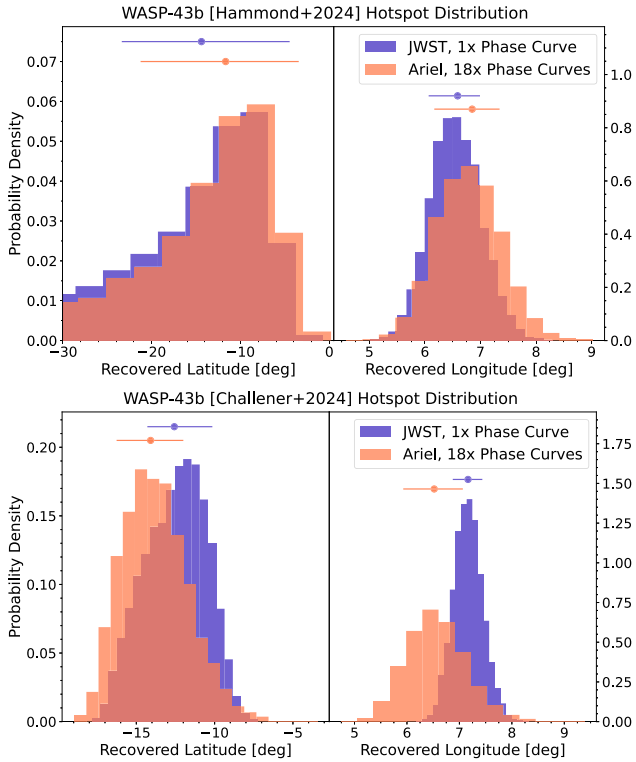

Figure 12. WASP-43b (*top*:) M. Hammond et al. (2024) and (*bottom*:) R. C. Challener et al. (2024) hotspot location posteriors. In blue is what we recover from the *JWST* (*top*:) MIRI/LRS and (*bottom*:) NIRSpec/G395H single phase curve maps, and in orange is what we recover from the 18 *Ariel* (*top*:) AIRS Ch1 and (*bottom*:) Ch0 phase curve maps, respectively. We recover consistent results, even in terms of latitude, but this test case highlights the time-costly nature of measuring such signals with a smaller observatories like *Ariel*.

going from 10 to 25 observations only in fact increases the SNR by 11.6 per cent, which is comparable to what is achieved by going from 2 to 3 observations (13.0 per cent). This is due to the inherent quadratic drop-off of SNR increase with repeat N observations, resulting in a wider spread in the number of required observations in this high-N regime that seemingly exacerbates the issue.

Secondly, *Ariel*'s lower collecting area results in longer integration times than *JWST*, and therefore fewer data points during ingress/egress. Since latitudinal signals are small-scale and localized to ingress/egress, this means that small modulations to individual data points here has a far greater impact on our ability to measure them with *Ariel* than it does with *JWST*. We tested whether increasing our sampling of ingress/egress beyond the optimized cadence could alleviate this issue, but found that the sacrifice in flux precision led to the same results. Conversely, when using the native integration times rather than the optimized cadence, the enhanced flux precision is unable to compensate for the reduced spatial scanning. We thus conclude that this is an inherent problem associated with latitudinal eclipse mapping using smaller observatories.

3.4.2 *Comparison between Ariel and JWST*

We discuss the median *Ariel* phase curve scenario for each test case, comprising 18 repeated observations. In both cases, we recover highly consistent latitudinal hotspot offsets with *Ariel* as we do with *JWST*, as evidenced by the overlapping posteriors in Fig. 12, with values of $-11.8^{+8.2\circ}_{-9.6}$ and $-14.1^{+2.1\circ}_{-2.2}$ for the AIRS Ch1 and Ch0 maps, respectively. We also recover longitudinal hotspot offsets which are now consistent with the eclipse mapping values of $6.9^{+0.5\circ}_{-0.7}$ and $6.5^{+0.5\circ}_{-0.6}$, respectively, indicating that our modelling framework is now correctly identifying both the phase and eclipse mapping signals. The flat difference maps in the bottom row of Fig. 11 support this, showing that we recover highly consistent thermal profiles now with the same degree of small-scale structure.

The median dayside temperature is constrained at comparable precision with *Ariel* as it is with *JWST*, at 50 K for AIRS Ch1 and 25 K for AIRS Ch0. Interestingly, the precision is the same for these *Ariel* maps derived from 18 phase curves as it is for the *Ariel* maps derived from single phase curves, despite the increased flux precision. This is due to the added uncertainty that the additional basis components (N5+) add to the higher order models; the eigenmaps are ranked in order of visibility, therefore higher order basis maps correspond to smaller scale signals which will naturally be less constrained (R. C. Challener & E. Rauscher 2022). The four-component mapping models derived in the single phase curve cases, on the other hand, are made up only of the highest magnitude signals, resulting in precise constraints even at lower flux precision. For more nuances of eclipse mapping temperature uncertainties, see R. C. Challener & E. Rauscher (2023).

Comparing between *JWST* and *Ariel* in Fig. 11 and Table 3, the AIRS Ch1 map shows the same trend as observed for previous test cases: a consistent median dayside temperature to what is observed with MIRI/LRS, but over a narrower temperature range. AIRS Ch0 has a more comparable bandwidth to its *JWST* equivalent, NIRSpec/G395H (see Fig. 1), therefore we find not only a comparable median dayside temperature in this case, but also a comparable temperature range.

3.4.3 *Phase curves versus eclipses*

In an attempt to overcome the prohibitive observing time of $\geq$10 phase curves, we tested whether the same number of eclipse-only observations would be sufficient to recover the input mapping model in this case. WASP-43b is one of the top 10 highest ranking mapping targets for both MIRI/LRS and NIRSpec/G395H (S. Boone et al. 2024), therefore we would expect to be able to map it from eclipse-only observations. Critically, latitudinal signals are only present during ingress/egress, therefore the phase information, which only constrains longitudinal signals, may not be necessary in order to measure them. We simulated these eclipses with standard 1:1 baseline, with an additional one hour pre-eclipse for systematic characterization, and a buffer of half an hour post-eclipse for a scheduling window.

We found that with a similar number (i.e. 10–25) of eclipse-only observations of each respective test case, *Ariel* is only able to recover the large-scale longitudinal profile through two-component maps, which is equivalent to what was found from single phase curves (but with N4 to also fit the phase signal). For comparison with the maps derived from 18 phase curves, we discuss the median case of 18 eclipse-only observations.

We recover a similar median dayside temperature and range in these eclipse-only maps as we do in the phase curve maps; note that the minimum temperatures quoted in Table 3 are higher than the phase curve cases because with eclipse-only observations, we no longer measure the entirety of the nightside. Whilst the median dayside temperatures agree between the maps, they are constrained at higher precisions in these eclipse-only maps of 15 K and 10 K for AIRS Ch1 and Ch0, respectively, compared to 50 K and 25 K for the phase curve maps. The higher precision compared to the

comparably low-order maps derived from single phase curves (N4, with the N3+ fitting the phase signal in these cases) can be attributed to the $\sqrt{18}$ SNR increase winning out over the added phase signal on the dayside. The better precision compared to the higher order maps derived from 18 phase curves (N6) can again be attributed to the higher order (N5+) basis maps contributing larger uncertainties.

Interestingly, we also recover consistent hotspot offsets in these eclipse-only maps as was recovered from the single phase curve cases of $9.6 \pm 1.0^\circ$ and $10.9 \pm 1.0^\circ$, respectively. This indicates that, even for this high-ranking target, the phase signal is in fact imperative in order to soundly anchor the large-scale, longitudinal structure, break ingress/egress signal degeneracies, and thus constrain the latitudinal structure. This same conclusion was reached in the original MIRI/LRS analysis by removing the phase information and fitting only the two eclipses (M. Hammond et al. 2024). For *Ariel*, without the phase information, we only recover the large-scale longitudinal structure, bringing the eclipse mapping hotspot offsets in-line with the phase mapping offsets. This test case is therefore another advocate for the need to use full phase curves in order to holistically map a large sample of planets.

The primary conclusion of this test case is therefore that latitudinal signal characterization is better left to *JWST* for the most optimal, individual case targets, since it requires an observatory with a large enough collecting area to simultaneously facilitate high flux precision and high cadence. Although these test cases have shown that *Ariel* can do the same, the data quantity needed to do so compared to *JWST* is unjustifiable. We recommend that what *Ariel* focus on is leveraging its greater dedicated observing time to model the longitudinal profiles of a large number of targets spanning a range of EMMs.

As proven by our test cases, *Ariel* has the capability to do this using single phase curve observations. In this regime of large-scale longitudinal signals, phase mapping and eclipse mapping offsets are equivalent, facilitating this observing strategy (R. C. Challener & E. Rauscher 2023). In particular, the day–night temperature contrast and east–west hotspot offset are measurable from such maps, which, as proven by a number of recent studies (e.g. D. Valentine et al. 2024b; M. Lally et al. 2025), are enough to constrain the first-order atmospheric dynamics. We therefore recommend that a population-level mapping survey with *Ariel* focus primarily on characterizing these signals.

3.5 Summary of test cases

We used these test cases in order to provide an assessment of *Ariel*'s eclipse mapping capabilities. Below, we group the questions that we set out to address, and the test cases that answered them.

(i) **Does *Ariel* have eclipse mapping capabilities?** The HD 189733b and HD 209458b test cases showed that *Ariel* has at least baseline eclipse mapping capabilities, since we were able to eclipse map these planets using all three of the *Ariel* spectrographs using only 1–2 eclipse observations.

(ii) **How does *Ariel* compare against *JWST*?** The WASP-18b test case showed that, whilst more data may be required to map even high-ranking targets due to *Ariel*'s lower collecting area, the amount is not exorbitant and in fact perfectly feasible for a dedicated exoplanet mission. Using as few as three eclipse observations, *Ariel* could eclipse map many of the highest ranking mapping targets.

(iii) **What is the best way to design these observations?** The WASP-17b test case showed that the data quantity required to map planets with lower EMMs does in fact start to become unfeasible using eclipse-only observations. However, the incorporation of phase information can help anchor our longitudinal signal in order to better identify signals in ingress/egress, and recover the mapping signal. For lower ranking targets, the use of phase curves is in fact the most time-efficient way to conduct these observations, and allows for a homogeneous data set from which the signal can always be robustly identified no matter the specific morphology of the phase curve.

(iv) **What should be *Ariel*'s primary mapping focus?** The WASP-43b test cases showed that, whilst *Ariel* can compete with *JWST* for longitudinal signals using a reasonable amount of data, it struggles to recover the more notorious latitudinal signals, requiring a much larger data set. Hence, we conclude that latitudinal studies, which require simultaneously high SNR and cadence, be left to the likes of *JWST*. What we recommend *Ariel* would be better focusing on is its ability to dedicate a great deal of observing time to a large population of planets.

By observing phase curves of a large and diverse sample, we have shown that *Ariel* has the ability to map all of their longitudinal profiles, from which their east–west hotspot offsets and day–night temperature contrasts are measurable. These parameters are enough to diagnose the first-order atmospheric dynamics (T. D. Komacek & A. N. Youdin 2017; A. Roth et al. 2024) and facilitate the largest scale assessment of exoplanet atmospheric dynamics to date.

4 RANKING THE BEST MAPPING TARGETS FOR ARIEL

Based on the results of our test cases, we now repeat the methodology that S. Boone et al. (2024) applied to determine the best eclipse mapping targets for *JWST* in order to do the same for *Ariel*. In this way, we provide a target list of the most advantageous targets for a population-level mapping survey with *Ariel*, designed to map the large-scale longitudinal profile and constrain the first-order atmospheric dynamics of these targets.

S. Boone et al. (2024) used analytic methods to derive a quantitative metric that assesses the eclipse mapping potential of a target observed using a specific instrument, based on the orbital parameters of the target and the performance of the instrument. This metric is therefore generalizable to any target observed using any observatory. Two quantities of interest are derived that encapsulate the eclipse mapping potential of a target.

The first quantity is the EMM itself. This corresponds to the minimum resolution element observable with eclipse mapping for a given planet observed using a given instrument, which is essentially the maximum resolution to which we can spatially resolve the planet, in units of degrees. This quantity is first calculated in a decomposed manner for the longitudinal and latitudinal components, EMM_x and EMM_y, respectively, which are defined as

$$\mathrm{EMM_x} = 180^\circ \times \left[\frac{2\sqrt{6\ln 2}}{\pi^2\sqrt{1-b^2}} \left(\left(\frac{F_0}{\sigma} \frac{1}{\pi} \sqrt{\frac{2R_\mathrm{p}}{\pi a\sqrt{1-b^2}}} \right)^{1/3} + \frac{1}{2} \right)^{-1} \right], \tag{3}$$

and

$$\mathrm{EMM_y} = 180^\circ \times \left[\frac{2\sqrt{6\ln 2}}{\pi^2 b} \left(\left(\frac{F_0}{\sigma} \frac{1}{\pi} \sqrt{\frac{2R_\mathrm{p}}{\pi a\sqrt{1-b^2}}} \right)^{1/3} + \frac{1}{2} \right)^{-1} \right], \tag{4}$$

with the overall EMM defined as the root sum of their quadrature,

$$\mathrm{EMM} = \sqrt{\mathrm{EMM_x}^2 + \mathrm{EMM_y}^2}. \tag{5}$$

Here, F_0 is the phase-averaged flux from the planet (carrying the system brightness and planetary temperature dependence), σ is the full-orbit integrated error on the phase-averaged flux (carrying the precision and cadence dependence), b is the impact parameter, a is the semimajor axis of the orbit, and R_p is the planetary radius (the combination of which carry the dependence of the stellar-edge angle and ingress/egress duration).

The second parameter of interest is N_{max}, which is the highest spherical harmonic order detectable. This parameter essentially defines the complexity of the signal that we can recover for a specific planet measured with a specific instrument using eclipse mapping. It is defined as

$$N_{max} = \left[\frac{F_0}{\sigma} \frac{1}{\pi} \sqrt{\frac{2R_p}{\pi a \cos\theta_0}} \right]^{\frac{1}{\gamma+1}} |_{\gamma=2}, \quad (6)$$

where the already defined parameters carry the same dependence as previous, and $\cos\theta_0 = \sqrt{1-b^2}$ carries the impact parameter dependence in this case.

Because this method is purely analytical, no input planetary models are used in order to calculate these metrics; however, some assumption must be made on the expected morphology of the planetary emission profiles in order to derive a quantitative metric, in particular the expected feature sizes. This dependence is incorporated via the γ factor, which carries the scaling of the assumed spatial power spectrum of these profiles as $F_N \sim N^{-\gamma}$. Similarly to S. Boone et al. (2024), we assume $\gamma = 2$ based on the predictions of numerous benchmarked GCM simulations of hot Jupiters [see A. P. Showman et al. (2020) for a comprehensive summary], which are our primary targets of interest for eclipse mapping purposes. Note that N_{max} is used in the derivation of the EMM quantities therefore this feature-scale assumption is folded into those metrics.

We calculate these quantities for all planets in the *Ariel* Mission Candidate Sample[5] (MCS; B. Edwards & G. Tinetti 2022) for the three *Ariel* spectrographs: NIRSpec, AIRS Ch0, and AIRS Ch1. We define a planet to be 'eclipse mappable' if it scores EMM$< 90°$, meaning it can be mapped at better than hemispheric resolution. We also require that $N_{max} \geq 1$, meaning that we can resolve higher order features than would be possible from only a phase signal.

Because these metrics are dependent on the precision and cadence of the observing instrument, the observations must be simulated in order to predict these quantities. We again use `ArielRad` (L. V. Mugnai et al. 2020) to simulate these observations, using the same methodology as that outlined in Section 2.1: we adopt the minimum saturation time within a spectrograph's wavelength channels as the cadence, unless this saturation time exceeds the time to obtain 32 samples across ingress/egress, which is required to maximize the spatial information content of the maps (R. C. Challener & E. Rauscher 2023). In such cases, we adopt a shorter cadence value that ensures this criterion, and degrade the flux precision accordingly by substituting this value back into `ArielRad`. For all observations, we then increase the flux precision by $\sqrt{2}$ as we are assuming $1.2\times$period phase curve observations of each target bracketed by two eclipses either side, motivated by the results of our test cases (see Section 3.5).

We note that these mapping metrics account only for ingress/egress signals, and therefore do not account for the additional phase information in the phase curve outside of eclipse. However, this would not increase either the EMM nor the N_{max} since phase information cannot provide smaller scale information than is already possible with eclipse mapping. The addition of this phase information therefore may seek to include more targets in our rankings, but would not increase the rankings of those that already meet our criteria. Since we are already dealing with large quantities of targets which we will eventually seek to limit to only the most optimal for our survey criteria, the addition of these lower ranking targets is therefore unnecessary.

4.1 *Ariel–JWST* comparison

We tabulate all of the *Ariel* 'eclipse mappable' targets identified by our calculations in Tables A1, A2, and A3 for Ariel NIRSpec, AIRS Ch0, and AIRS Ch1, respectively, listed in order of their EMM. In total, we find that 66 targets are mappable with Ariel NIRSpec, 113 with AIRS Ch0, and 136 with AIRS Ch1. The preceding tables are essentially subsets of one another, with every target but one in both NIRSpec (HATS-67b) and AIRS Ch0 (K2-107b) also contained within AIRS Ch1, totalling 138 unique targets overall.

As previously mentioned in Section 3.3, we also repeated the *JWST* analysis of S. Boone et al. (2024) in order to expand their rankings and encourage future eclipse mapping studies of more targets. Like S. Boone et al. (2024), we used `PandExo` (N. E. Batalha et al. 2017) to simulate the flux precision and cadence of each *JWST* observation. We tabulate the top 100 eclipse mapping targets for *JWST* NIRISS/SOSS, NIRSpec/G395H, and MIRI/LRS in Tables B1, B2, and B3, but here assuming the SNR of one eclipse since *JWST* has a much larger collecting area and time-constrained nature than *Ariel*. For comparison with our *Ariel* findings, we find 200 targets to be mappable with *JWST* NIRISS/SOSS, 362 with NIRSpec/G395H, and 296 with MIRI/LRS (the full rankings of these instruments can be found on Zenodo at 10.5281/zenodo.17245372). These lists are again subsets of one another, with nine targets unique to MIRI/LRS, 66 to NIRISS/SOSS, and none to G395H, for a total of 437 unique targets overall. With our proposed observational design, *Ariel* therefore has the capabilities to map up to a third of the total number of targets that *JWST* could. However, we highlight that a single *Ariel* observation would measure these planets across its entire wavelength range ($0.5 - 7.8$ μm), whereas *JWST* can only observe using one instrument at a time.

These rankings for each of the *Ariel* spectrographs contain many similar targets to their *JWST* equivalents, with the top-ranking targets being largely the same between the equivalent instruments (see Fig. 1) of each observatory. This is to be expected since the overall sample selection is dominated by the system parameter dependence, which carry the greatest weighting in the metric calculations (see equations 3, 4, and 6). The specific scaling of where planets rank, on the other hand, is more dependent on the wavelength range, precision, and cadence of the instrument, hence why we see targets fall in different positions between the *Ariel* and *JWST* results (see Appendix tables).

The most notable difference between the *JWST* and *Ariel* rankings is not in the targets themselves, but in the distribution that they span in EMM parameter space. Figs 7, 8, and 9 of S. Boone et al. (2024) show the EMM parameter space of the top 100 targets for *JWST* NIRISS/SOSS, NIRSpec/G395H, and MIRI/LRS. These plots show a clustering of targets at small EMM_x (increased longitudinal resolution), whilst being more widely distributed in EMM_y. In Fig. 13, we plot the equivalent EMM parameter space of all the *Ariel* eclipse mappable targets for its three spectrographs. Conversely to the *JWST* parameter space, these plots show a similarly broad distribution of targets in both EMM_x and EMM_y.

[5] https://github.com/arielmission-space/Mission_Candidate_Sample, v. 2024-07-09.

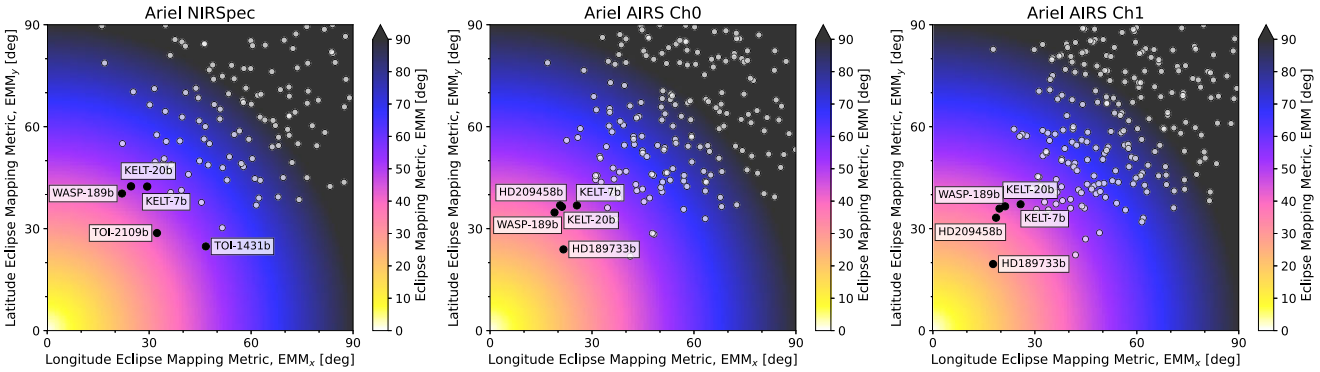

Figure 13. The eclipse mapping metric (EMM) parameter space for the three *Ariel* spectrographs: (left) NIRSpec, (middle) AIRS Ch0, and (right) AIRS Ch1. Targets increase in ranking going to the bottom left of the plots. The top five highest ranking targets for each instrument are labelled.

This can be explained by the inherent observability of each signal. The assumed power law used to derive the EMM carries the higher amplitude nature of longitudinal signals compared to the lower amplitude latitudinal signals, which is consistent with what we see from our test cases. Hence, longitudinal signals are naturally easier to measure. As such, the longitudinal eclipse mapping signals of even lower ranking targets are easily identifiable by both *JWST* and *Ariel*. With increasingly higher precision, increasingly smaller scale longitudinal signals therefore become easily observable for many targets. Because S. Boone et al. (2024) only plot the top 100 targets for each *JWST* spectrograph, we therefore observe a clustering of these targets at small, high-ranking EMM$_x$ below ∼40–50°. Due to the lower collecting area and therefore flux precision of *Ariel*, this limit is not as easily reached for as many of the top-ranking targets, resulting in a wider distribution of targets in EMM$_x$ for approximately the same number of plotted targets as *JWST*, extending to EMM$_x$∼80–90°. To showcase this, we re-plot the EMM parameter space of the *JWST* spectrographs in Fig. B1, including all targets with EMM< 90°. When additionally including these lower ranking targets, we see that the EMM$_x$ target distribution is now as widely dispersed as that of *Ariel*, confirming that this apparent EMM$_x$ bias arises from the primary dependence of longitudinal signal observability being tied to the precision of the observing instrument.

The geometry of eclipse also means that the longitudinal profile itself is optimally scanned over for most targets, whereas the latitudinal profile is only well sampled for planets with high impact parameters. Due to the cosine relationship between inclination and impact parameter ($b \propto \cos i$), this skews the observability of the latitudinal profile to the small fraction of planets that orbit far from the stellar equator. Hence, even with infinitely high flux precision, latitudinal signals are still unrecoverable if the orbital geometry is suboptimal. The observability of latitudinal signals is therefore set primarily not by the flux precision of the instrument, but by the orbital geometry of the system, particularly the impact parameter of eclipse. Hence, the distribution of targets in EMM$_y$ is similarly broad for both *JWST* and *Ariel*.

4.2 Target selection

Fig. 14 shows the period-temperature parameter space of the *Ariel* 'eclipse mappable' targets. They span irradiation temperatures between 850−4350 K, periods up to ∼22 d, and radii from 0.65−2.1 R$_J$. A population-level eclipse mapping survey of irradiated gas giants, ranging from warm to ultra-hot Jupiters, is therefore possible using *Ariel*. However, we calculate that to observe each of these 138 eclipse mappable targets using a 1.2×period phase curve observing strategy would require 600 d of observing time. With a 4-yr primary mission lifetime and a projected ∼70 per cent observing efficiency (B. Edwards & G. Tinetti 2022), *Ariel* is expected to have 24 800 h, or ∼1033 d, of science time available. Hence, approximately 60 per cent of this science time would be needed to adopt this strategy. Given that *Ariel* aims to observe ∼1000 targets, this amount of science time is clearly unfeasible. To reduce this overly large fraction, we therefore apply selection cuts in order to craft the most time-effective survey which would maximize the scientific returns whilst still maintaining the diversity of the sample.

We begin by excluding targets that are mappable using only one of the *Ariel* spectrographs, as this would not maximize the scientific returns of the mission. There is only one target each that is mappable with the NIRSpec and AIRS Ch0 instruments that are not mappable with AIRS Ch1: these are HATS-67b and K2-107b, respectively. Additionally, there are 24 targets that are mappable with AIRS Ch1 but not the other two spectrographs. After removing all of these, we are left with 112 targets which are mappable in at least 2/3 of the *Ariel* spectrographs. This brings the science observing time down to 432 d, or 42 per cent of the projected available science time.

In Fig. 15, we plot the number of these potential targets and the percentage of the projected *Ariel* science time that would be required to observe them, as a function of different maximum period cut-offs. At $P > 1$ d, we see a steadily increasing rate in the number of targets in the survey for small added increments in period cut-off, which fully plateaus by P∼15 d, at which point we include all 112 of the targets that are mappable in at least 2/3 of the *Ariel* spectrographs. This plateau begins at P∼6.4 d (purple dashed line), signifying a reduction in time efficiency to include targets with periods longer than this. Excluding such targets leaves us with 109 planets observable in 394 d, or ∼ 38 per cent of the projected science time of the mission. The additional three targets above this cut-off therefore require a substantial 38 d, or ∼4 per cent of the total available science time, to be observed. This highlights the greater cost of including longer period planets, and that a period cut-off is required to prevent this.

There is an earlier plateau in the time efficiency curve in the form of a step function which extends from $4 \lesssim P \lesssim 4.2$ d (pink dashed line), which is also in the inset of Fig. 14. Establishing a period cut-off of 4.2 d at this first point of reduction in time efficiency leaves us with 87 targets, for which full 1.2× period phase curves would be observable using only 26 per cent (269 d) of the projected mission science time, a substantial improvement over that acquired using the later period cut-off. The targets with periods below this cut-off span $T_{\rm irr}$ ∼ 1350−4400 K, which still well samples the boundaries of the warm

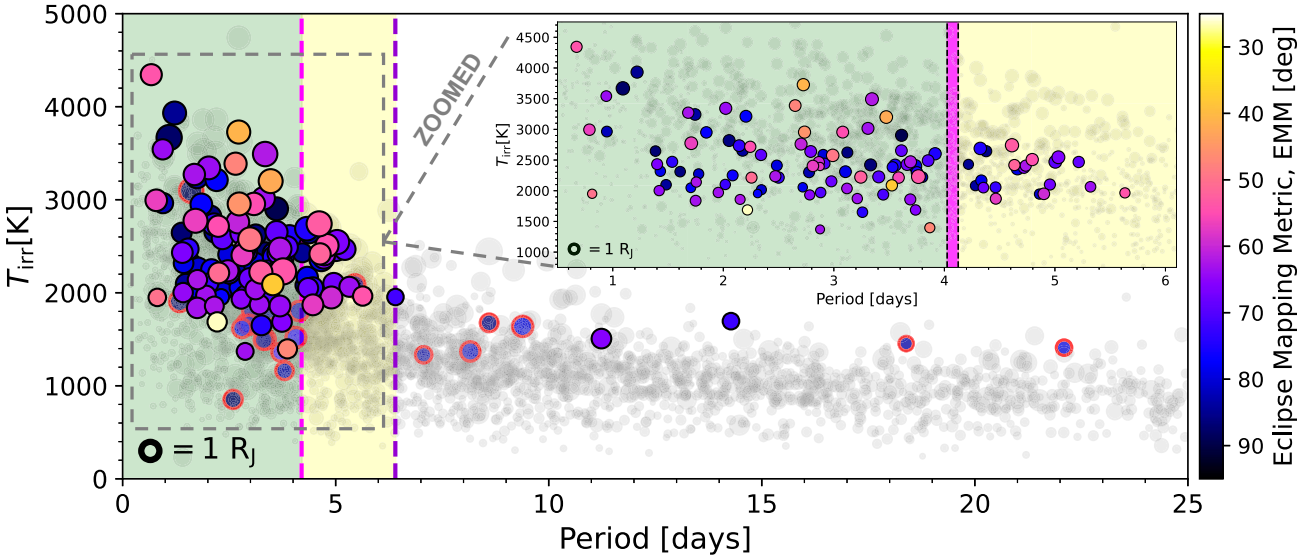

Figure 14. *Ariel* 'eclipse mappable' targets. The data points are scaled according to the radius of the planet, and shaded according to their AIRS Ch1 EMM values (except HATS-67b and K2-107b, for which we use their NIRSpec and AIRS Ch0, values, respectively – see Section 4.2 for details). Outlined in red are targets which are only mappable with 1/3 of the *Ariel* spectrographs, which we exclude from our survey design due to their lower scientific contribution. In grey is the total population for a sense of demographics. The dotted lines mark the different period cut-offs discussed in the text, and the inset shows a zoom-in of these shorter period targets. Targets outlined in black in the green shaded region ($P \leq 4.2$ d) are the ones that we ultimately adopt.

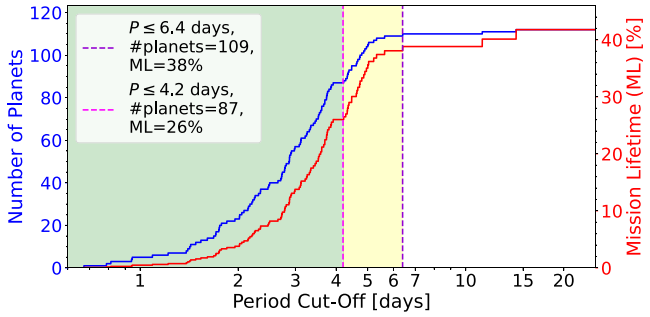

Figure 15. Number of 'eclipse mappable' targets that are mappable in at least 2/3 *Ariel* spectrographs, versus the percentage of projected *Ariel* science time available (24 800 h, B. Edwards & G. Tinetti 2022) that would be required to observe them, as a function of different period cut-offs. We highlight with dotted lines two plateaus of these curves at $P = 4.2$ and $P = 6.4$ d.

to ultra-hot Jupiter parameter space. The additional 22 targets with $4.2 \lesssim P \lesssim 6.4$ d span a narrower range of $T_{irr} \sim 2000-3000$ K, with similar radii and other non-plotted parameters, including mass and gravity, and therefore provide no significant additional diversity to our sample beyond period. Hence, we elect to exclude these less time-efficient, longer periods targets, and adopt a period cut-off of 4.2 d. However, we note that we explore the benefits of including select long-period cases to test extreme case effects on the atmospheric dynamics in Section 4.3.

We tabulate the 87 targets that ultimately meet our suggested survey criteria in Table 4, listed in alphabetical order. The *Ariel* MCS is divided into a tiered system from Tiers 1−3, with increasingly in-depth characterization and observing time for higher tier targets (B. Edwards & G. Tinetti 2022). A fourth tier is currently dedicated to ancillary science, including phase curves, using ∼10 per cent of the mission lifetime (B. Charnay et al. 2022). Most of the targets in our curated survey are already designated as high-ranking Tier 3 targets (B. Edwards & G. Tinetti 2022), designated for in-depth characterization using increased observing time, to which our proposed observing strategy is highly conducive.

With phase curve observations, both the transit and eclipse are observed, which facilitate transmission and emission spectroscopy; hence, while phase curves formally fall in Tier 4 of the current *Ariel* formulation, these observations would also meet Tier 3 criteria, enabling a hybridized approach between the two and thus sharing of designated observing time. A current *Ariel* phase curve working group report (priv. comm.) estimates that by following this hybrid-tier approach, ∼25 per cent of the primary mission lifetime could be dedicated to phase curve observations, which would be enough to observe all of our Table 4 targets. The use of phase curves for observations also reduces slewing and waiting time compared to repeat transits and/or eclipse observations, which increases the mission efficiency and thus science time available (B. Charnay et al. 2022), further facilitating the practicality and advantages of this strategy.

We note that an alternative analysis focusing only on the EMM_x metric could be conducted since we advocate that *Ariel* should primarily focus on characterizing the longitudinal profile rather than the latitudinal. However, when dealing with such a large quantity of targets, whilst the ranking order would change, the overall target list would remain largely invariant therefore our overall survey and the parameter space it samples would not significantly change.

4.3 Survey demographics

Fig. 16 shows the demographics of our suggested survey targets compared to the total population, in particular the periods, masses, radii, gravities, and irradiation temperatures that they span. Here, we explore the five parameters that are expected to dominate atmospheric dynamics at first order (A. Roth et al. 2024), and how this large-scale survey with *Ariel* would diagnose their exact influence.

Table 4. Suggested targets for a population-level mapping survey with *Ariel*. These have EMM $< 90^\circ$ and $N_{\max} \geq 1$ in at least 2/3 of the *Ariel* spectrographs, and $P \leq 4.2$ d. We list the targets alphabetically, with relevant system parameters, and provide their eclipse mapping ranking for each of the *Ariel* spectrographs.

Planet name	$T_{\rm eq}$ (K)	$R_{\rm p}$ ($R_{\rm J}$)	$M_{\rm p}$ ($M_{\rm J}$)	P (d)	b	K (mag)	NIRSpec Ranking	AIRS Ch0 Ranking	AIRS Ch1 Ranking
GPX-1b	2293	1.47	19.7	1.74	0.82	11.18	38	79	109
Gaia-2b	1314	1.32	0.82	3.69	0.79	9.74	/	55	45
HAT-P−13b	1727	1.27	0.85	2.92	0.62	8.98	49	59	66
HAT-P−16b	1627	1.29	4.19	2.78	0.42	9.55	/	104	106
HAT-P−20b	969	0.87	7.25	2.88	0.63	8.6	/	88	38
HAT-P−22b	1324	1.15	2.47	3.21	0.43	7.84	/	57	41
HAT-P−30b	1699	1.44	0.83	2.81	0.77	9.15	22	20	23
HAT-P−50b	1855	1.29	1.35	3.12	0.63	10.5	/	101	122
HAT-P−56b	1866	1.51	2.31	2.79	0.85	9.83	29	39	53
HAT-P−6b	1761	1.48	1.32	3.85	0.54	9.31	47	56	64
HAT-P−7b	2272	1.51	1.84	2.2	0.47	9.33	28	64	85
HATS-1b	1370	1.3	1.86	3.45	0.7	10.58	/	74	65
HATS-65b	1633	1.5	0.82	3.11	0.67	11.1	/	84	89
HD149026b	1693	0.74	0.38	2.88	0.63	6.82	43	23	25
HD189733b	1193	1.13	1.13	2.22	0.67	5.54	16	1	1
HD202772Ab	2133	1.54	1.02	3.31	0.41	6.96	27	31	39
HD209458b	1477	1.39	0.73	3.52	0.49	6.31	18	4	2
K2-29b	1167	1.19	0.73	3.26	0.62	10.06	/	102	75
KELT-14b	1961	1.74	1.28	1.71	0.86	9.42	12	17	22
KELT-17b	2090	1.52	1.31	3.08	0.57	8.65	13	15	19
KELT-20b	2263	1.74	3.38	3.47	0.5	7.42	3	3	4
KELT-21b	2053	1.59	3.91	3.61	0.42	10.09	/	111	135
KELT-23Ab	1565	1.32	0.94	2.26	0.57	8.9	21	9	10
KELT-3b	1952	1.56	1.94	2.7	0.53	8.66	17	26	28
KELT-4Ab	1822	1.7	0.9	2.99	0.69	8.69	7	8	8
KELT-7b	2089	1.6	1.39	2.73	0.57	7.54	4	5	5
KELT-8b	1571	1.62	0.66	3.24	0.86	9.18	24	16	12
KPS-1b	1448	1.03	1.09	1.71	0.75	10.93	/	89	86
Qatar-1b	1416	1.14	1.29	1.42	0.65	10.41	64	46	46
TOI-1194b	1382	0.78	0.38	2.31	0.8	9.34	/	97	84
TOI-1431b	2395	1.49	3.12	2.65	0.88	7.44	5	6	7
TOI-157b	1591	1.29	1.18	2.08	0.8	10.89	/	78	82
TOI-1937Ab	2096	1.25	2.01	0.95	0.87	11.23	40	76	103
TOI-2109b	3072	1.35	5.02	0.67	0.75	9.07	1	7	16
TOI-2236b	1687	1.28	1.58	3.53	0.77	9.96	63	73	80
TOI-3331Ab	1487	1.16	2.27	2.02	0.57	9.91	/	69	70
TOI-4137b	1570	1.21	1.44	3.8	0.58	10.0	/	105	105
TOI-4463Ab	1394	1.18	0.79	2.88	0.88	9.4	/	72	63
TOI-905b	1192	1.17	0.67	3.74	0.82	9.45	/	70	50
TrES-2b	1581	1.36	1.49	2.47	0.77	9.85	41	35	34
TrES-4b	1708	1.61	0.78	3.55	0.82	10.33	56	71	81
TrES-5b	1483	1.19	1.79	1.48	0.61	11.59	/	107	113
WASP-101b	1566	1.43	0.51	3.59	0.72	9.07	30	21	20
WASP-104b	1514	1.14	1.27	1.76	0.73	9.88	48	37	32
WASP-119b	1566	1.4	1.23	2.5	0.57	10.54	/	68	72
WASP-120b	1876	1.47	4.85	3.61	0.77	9.88	33	44	58
WASP-123b	1522	1.32	0.9	2.98	0.53	9.36	/	58	57
WASP-12b	2594	1.94	1.46	1.09	0.34	10.19	32	86	130
WASP-135b	1720	1.3	1.9	1.4	0.76	11.04	34	38	52
WASP-142b	1992	1.53	0.84	2.05	0.77	11.44	54	95	123
WASP-14b	1920	1.38	8.84	2.24	0.56	8.62	15	14	18
WASP-153b	1712	1.55	0.39	3.33	0.61	11.05	/	106	125
WASP-15b	1626	1.41	0.54	3.75	0.53	9.69	/	75	76
WASP-163b	1634	1.2	1.87	1.61	0.45	10.15	/	108	121
WASP-164b	1608	1.13	2.13	1.78	0.82	10.96	/	93	99
WASP-167b	2363	1.58	8.0	2.02	0.77	9.76	10	28	44
WASP-16b	1440	1.22	1.24	3.12	0.65	9.59	58	42	40
WASP-170b	1426	1.1	1.6	2.34	0.69	10.72	/	100	98
WASP-173Ab	1871	1.2	3.69	1.39	0.4	10.0	/	103	127
WASP-178b	2469	1.81	1.66	3.34	0.54	9.7	9	24	29
WASP-17b	1699	1.93	0.48	3.74	0.35	10.22	/	85	91
WASP-189b	2636	1.62	1.99	2.72	0.48	6.06	2	2	3
WASP-18b	2504	1.24	10.2	0.94	0.37	8.13	11	25	43

Table 4 – *continued*

Planet name	T_{eq} (K)	R_p (R_J)	M_p (M_J)	P (d)	b	K (mag)	NIRSpec Ranking	AIRS Ch0 Ranking	AIRS Ch1 Ranking
WASP-19b	2117	1.42	1.15	0.79	0.67	10.48	6	10	21
WASP-24b	1827	1.38	1.24	2.34	0.61	10.15	36	45	60
WASP-2b	1314	1.08	0.93	2.15	0.75	9.63	/	49	31
WASP-31b	1574	1.55	0.48	3.41	0.78	10.65	55	60	62
WASP-32b	1454	0.96	2.63	2.72	0.76	10.16	/	96	87
WASP-33b	2781	1.59	2.09	1.22	0.21	7.47	44	83	116
WASP-36b	1747	1.33	2.36	1.54	0.69	11.29	46	63	74
WASP-3b	2086	1.42	2.43	1.85	0.41	9.36	39	66	83
WASP-43b	1379	0.93	1.78	0.81	0.66	9.27	25	12	9
WASP-46b	1639	1.17	1.91	1.43	0.73	11.4	/	80	90
WASP-48b	1933	1.5	0.8	2.14	0.81	10.37	35	53	73
WASP-49b	1366	1.11	0.37	2.78	0.75	9.75	/	54	47
WASP-50b	1394	1.17	1.47	1.96	0.67	9.97	66	43	37
WASP-52b	1299	1.27	0.46	1.75	0.6	10.09	/	50	36
WASP-54b	1747	1.58	0.59	3.69	0.53	9.04	31	32	30
WASP-69b	988	1.11	0.29	3.87	0.65	7.46	/	30	6
WASP-71b	1830	1.18	1.39	2.9	0.55	9.32	61	82	96
WASP-75b	1705	1.27	1.07	2.48	0.89	10.06	/	87	95
WASP-79b	1716	1.53	0.85	3.66	0.5	9.06	45	48	55
WASP-87b	2313	1.38	2.18	1.68	0.6	9.55	8	22	35
WASP-90b	1840	1.63	0.63	3.92	0.84	10.25	51	67	79
WASP-92b	1879	1.46	0.8	2.17	0.61	11.52	57	94	112
XO-6b	1577	2.07	4.4	3.77	0.63	9.25	26	19	14
XO-7b	1744	1.37	0.71	2.86	0.73	9.24	23	29	27

(i) **Irradiation temperature:** This is one of the dominant factors that controls atmospheric dynamics, affecting both the heat circulation regime and resultant shaping of the temperature profile through factors like the hotspot offset (A. P. Showman et al. 2020). The irradiated gas giant population transitions from a rotationally dominated regime with efficient recirculation at the cooler end of the spectrum (i.e. for warm Jupiters), where advective time-scales win out over radiative, to a divergence-dominated, inefficient recirculation regime at the hotter end, where radiative time-scales win out over advective (i.e. for ultra-hot Jupiters). Both of these effects result in the lack of a hotspot offset, due to the lack of a hotspot for the former and a localization of the hotspot at the substellar point for the latter. In the regime between these two, there exists a complex, non-monotonic relationship between the irradiation temperature and hotspot offset due to the competing influence of both rotational and divergent components (T. G. Beatty et al. 2019). Fig. 16 shows that our survey targets span a range of irradiation temperatures, with a median value of 2400 K ($T_{eq} = 1700$ K) between a range of 1370 K and 4350 K. Hence, with this survey, we would be able to robustly diagnose the impact of irradiation temperature on the atmospheric dynamics in the critical transition regime between advective- and radiative-dominated environments.

(ii) **Period and rotation rate:** All of our targets of interest are on short orbits and are therefore expected to be both highly irradiated and tidally locked, often leading to the formation of a super-rotating equatorial jet. Whether this jet dominates the circulation regime is influenced by the rotation rate (T. Kataria et al. 2016). Faster rotation rates can seek to narrow jet widths, forming decoupled latitudinal banding in the atmosphere akin to the solar system gas giants, and lead to the formation of additional high-latitude jets. In this regime, latitudinal recirculation over the poles is expected to become the dominant circulation regime, with expected shallow longitudinal temperature gradients. Conversely, slower rotation rates lead to a single wide equatorial jet dominating the circulation regime, resulting in shallow latitudinal temperature gradients and heat primarily being recirculated around the equator (A. P. Showman, N. K. Lewis & J. J. Fortney 2014). The exact quantitative balance and transition between these regimes as a function of rotational and orbital period have not been observationally benchmarked, and their effect on observables like the hotspot offset is expected to be non-trivial. Fig. 16 shows that with our proposed survey, which samples planets with periods between 0.7 and 3.9 d, such an analysis could be facilitated by measuring the longitudinal temperature gradients.

As a dedicated exoplanet mission, *Ariel* also has the potential to test more extreme cases in this rotational period regime by observing planets with periods too long to be feasible with the likes of *JWST*. Beyond our discussed period cut-offs of 4.2 and 6.4 d, there are two longer period planets that meet the criterion of being mappable in at least 2/3 *Ariel* spectrographs (see Fig. 14): these are TOI-677b and HD 221416b, with periods of 11.2 and 14.3 d, respectively. Including targets such as this in the sample would allow *Ariel* to push the boundaries of our data-driven knowledge of how rotational and orbital periods affect exoplanet atmospheric dynamics, including testing the tidal locking radius itself (see H. R. Wakeford et al. 2025).

(iii) **Gravity:** We expect higher gravity planets to have weaker day–night recirculation regimes as a consequence of damped circulation patterns (A. Roth et al. 2024), which would manifest itself as a smaller hotspot offset, as was observed for WASP-43b (M. Hammond et al. 2024; R. C. Challener et al. 2024). However, there is no general consensus on the magnitude or dominance of this effect. Mapping and comparing planets with similar characteristics, but different gravities, would therefore allow us to diagnose the quantitative impact of gravity on the atmospheric dynamics. Gravity also contributes in setting the opacity and pressure level of the photosphere, which influences the balance between radiative and advective time-scales, and therefore the nature of the circulation regime (A. P. Showman et al. 2020).

Fig. 16 shows that our proposed survey spans planetary radii of $0.74 - 2.07$ R_J (median $= 1.36$ R_J) and planetary masses of 0.3–19.7 M_J (median $=1.31$ M_J), and therefore also probes a wide range

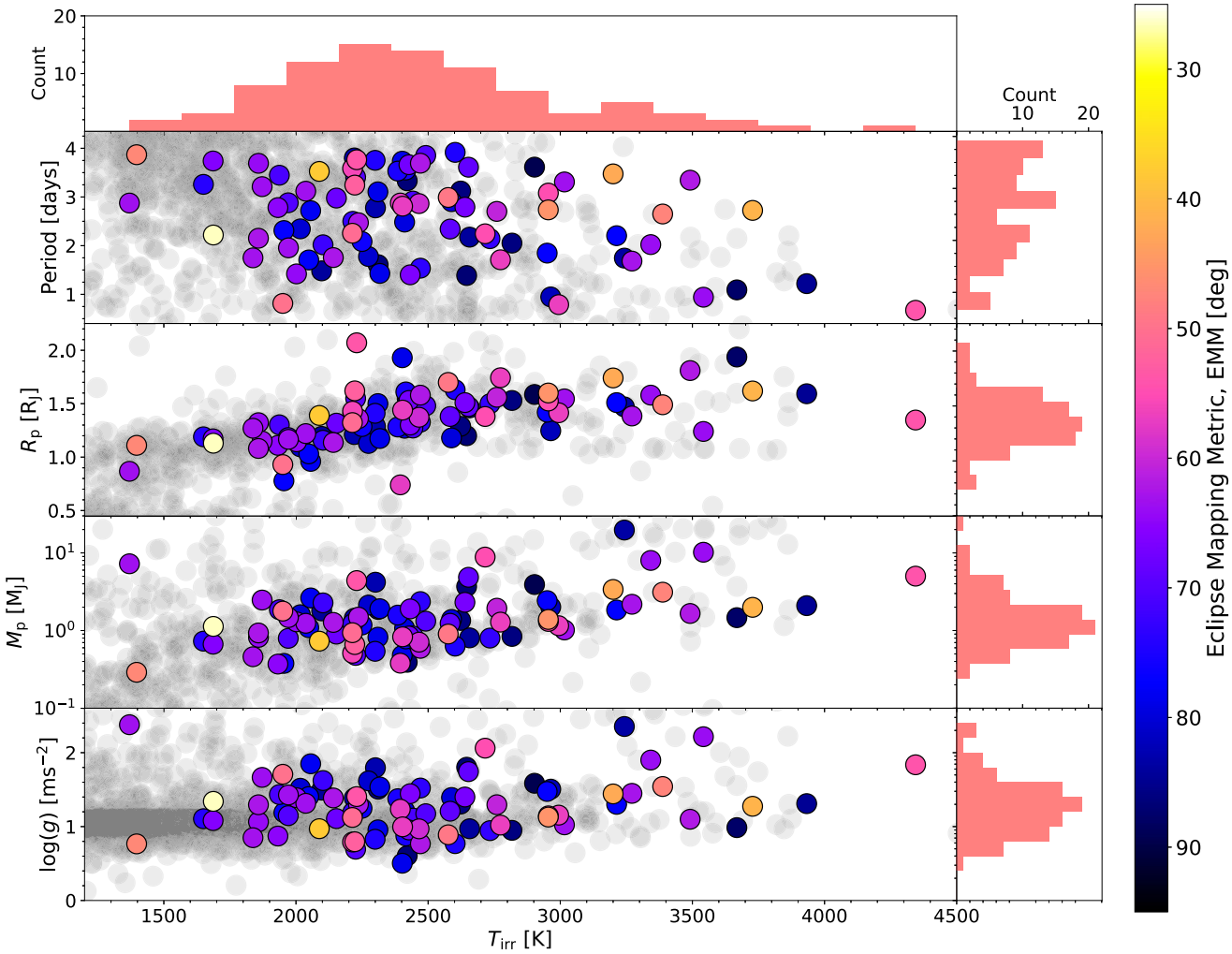

Figure 16. Population demographics of our 87 selected targets. We shade the targets according to their AIRS Ch1 EMM values, and show the total population in the background in grey. We plot the periods, radii, masses, and gravities of these targets against their irradiation temperatures. A survey such as this would well sample the parameter space of irradiated gas giants, enabling a comprehensive assessment of their thermal structures and atmospheric dynamics.

of surface gravities, from log(g) = 0.5–2.4 ms^{-2} (median = 1.3 ms^{-2}), including targets in the brown dwarf mass regime. These can effectively be treated as high-mass hot Jupiters, allowing *Ariel* to probe the extreme effects of gravity on the atmospheric dynamics. We note that mass does not factor into our EMM calculations, and therefore the upper mass of our survey is largely a consequence of the artificial 30 M_J cut-off of the NASA Exoplanet Archive (J. L. Christiansen et al. 2025), from which the MCS is derived. Higher mass brown dwarfs may therefore also be mappable; such work is being explored in D. Lewis et al. (in preparation).

(iv) **Metallicity:** We have thus far discussed the impact of system parameters on the atmospheric dynamics. Such parameters tend to be known a priori for most targets. However, atmospheric parameters themselves, which are not often known a priori, are also expected to have first-order effects on the atmospheric dynamics. Similar to gravity, the metallicity also contributes in setting the photospheric pressure and therefore circulation regime, with metallicity and hotspot offsets expected to be inversely related (A. Roth et al. 2024). Similarly, enhanced metallicities seek to reduce atmospheric flow and jet speeds, resulting in more inefficient day–night heat recirculation. Hence, knowledge of the atmospheric metallicity is imperative for interpreting the atmospheric dynamics, and may inhibit definitive constraints if not accounted for (D. Valentine et al. 2024b).

Ariel's chemical census will be particularly conducive to such an assessment. The use of phase curves to perform these measurements is also beneficial since the shape of the phase curve can itself be used to measure the metallicity, with metallicity expected to be proportional to the phase curve amplitude and inversely proportional to the phase curve offset (V. Parmentier & I. J. M. Crossfield 2018). With such a large data set, these measurements can also be used in a data-model feedback loop to qualitatively benchmark the assumptions made in deriving these quantitative proportionalities. Atmospheric metallicity is expected to be somewhat correlated with mass (L. Welbanks et al. 2019), and since our survey samples a wide mass range of 0.3–19.7 M_J (Fig. 16), we expect to also survey a wide range of metallicities. Hence, this large-scale phase curve survey with *Ariel* would provide the most precise and comprehensive diagnostic assessment of the effect of metallicity on the atmospheric dynamics to date.

(v) **Atmospheric chemistry and clouds:** Beyond the generalized metallicity, individual chemical species can also carry first-order implications on the atmospheric dynamics. The presence of strong

optical absorbers like TiO and VO in the photosphere can lead to thermal inversions, which may alter the thermal structure (A. Roth et al. 2024). Condensates in the forms of clouds are already known to have a significant impact on flux maps through their modulation of the spatial thermal emission profile (V. Parmentier et al. 2016; T. G. Beatty et al. 2019); such effects have already been observed for *JWST* eclipse maps (M. Hammond et al. 2024; T. J. Bell et al. 2024). *Ariel*'s photometric filters will allow the presence of these clouds to be identified, and their spatial distribution potentially mapped using our survey design. Synergistic observations with *JWST* MIRI/LRS may also allow the vibrational mode of the cloud to be measured for even better characterization (H. R. Wakeford & D. K. Sing 2015; D. Grant et al. 2023; J. Inglis et al. 2024). Our proposed survey targets span a large temperature range over which we expect to see significant transitions in the cloud species and properties (P. Gao et al. 2021), enabling *Ariel* to comprehensively diagnose the impact of clouds on the atmospheric dynamics.

In summary, a survey such as this with *Ariel* would well sample the parameter space of irradiated gas giants, which ensures the diversity needed in order to derive statistically significant population-level trends of their atmospheric dynamics. Crucially, it is evident from the above descriptions of these parameters that they often have degenerate impacts on the atmospheric dynamics. Inspection of the Rossby number equation, for example, shows that as far as atmospheric dynamics are concerned, decreasing the planetary radius and increasing the rotation rate have the same effect (N. T. Lewis & M. Hammond 2022). Similarly, whilst higher irradiation temperature can result in smaller hotspot offsets, so too can higher metallicities, gravity, and even morning limb clouds (A. P. Showman et al. 2020). These degeneracies are why the population-level trends of exoplanet atmospheric dynamics have to date been unable to be constrained using the data quantity available, and why quantitative target-by-target comparisons often suffer from attribution degeneracies since an ensemble of different parameter combinations can produce the same atmospheric dynamics (D. Valentine et al. 2024b).

This survey with *Ariel* would constitute the largest assessment of exoplanet atmospheric dynamics to date, superseding the previous largest attempt using 29 *Spitzer* 4.5 μm phase curves (L. Dang et al. 2025) by a factor of three. That survey found indications of population-level trends, but could not draw statistically significant conclusions due to both the small survey size, which inhibited their ability to control for all the aforementioned degenerate parameters, and problems with lack of uniformity between the data sets and analyses. Our three-times larger *Ariel* survey would allow for adequate sample sizes whilst still being able to control for all these parameters, whilst our uniform observing strategy would enable holistic interpretation. As such, this survey would revolutionize our understanding of exoplanet atmospheric dynamics and provide the most comprehensive data-driven benchmarking of model predictions ever performed.

5 CONCLUSIONS

Multidimensional characterization of exoplanet atmospheres is rising in applicability and wide-spread application with the advent of new techniques and increase in data quality (e.g. K. Jones & N. Espinoza 2020; R. C. Challener & E. Rauscher 2022; D. Grant & H. R. Wakeford 2023; L.-P. Coulombe et al. 2023; M. Hammond et al. 2024; M. M. Murphy et al. 2024, 2025; N. Espinoza et al. 2024; R. C. Challener et al. 2024; D. Valentine et al. 2024b; M. Lally et al. 2025; S. Mukherjee et al. 2025). Eclipse mapping is one such technique which can be used to map the dayside spatial emission profiles of transiting exoplanets, from which we can characterize their 3D (longitude–latitude–pressure) thermal patterns and constrain their atmospheric dynamics (E. Rauscher et al. 2007).

JWST is currently spearheading the application of this technique, but as an oversubscribed general observatory, its ability to do this on a population-level is time-limited. Hence, we assessed the eclipse mapping potential of the upcoming ESA *Ariel* mission (G. Tinetti et al. 2018). *Ariel* is a dedicated exoplanet mission set to observe ∼1000 transiting exoplanets over a four-year mission lifetime, making it a perfect candidate to facilitate population-level studies.

To assess *Ariel*'s eclipse mapping potential, we began by taking existing *JWST* eclipse maps [WASP-18b, L.-P. Coulombe et al. (2023); WASP-43b, M. Hammond et al. (2024) and R. C. Challener et al. (2024); WASP-17b, D. Valentine et al. (2024b); and HD 189733b, M. Lally et al. (2025)], along with a GCM output of HD 209458b for completeness of the canonical hot Jupiters (M. Hammond & D. S. Abbot 2022), and used them as test cases. By post-processing these maps into simulated *Ariel* light curves and retrieving on them, we benchmarked the data quantity needed for *Ariel* to derive qualitatively comparable maps to *JWST*, and compared the quantitative constraints achieved with each observatory. We outline the results of our test cases below.

(i) HD 189733b and HD 209458b are two of the highest ranking eclipse mapping targets (S. Boone et al. 2024). We found that *Ariel* will be able to recover the same qualitative map as *JWST* using the same amount of data for both of these bright targets, while also expanding the wavelength coverage over which they are mappable.

(ii) WASP-18b ranks as 22nd best eclipse mapping target for *JWST* (S. Boone et al. 2024). We found that *Ariel* will be able to map it using three eclipse observations, compared to one for *JWST*. Hence, we determined that *Ariel* will be capable of mapping all of *JWST*'s highest ranking targets using a feasible number of observations.

(iii) WASP-17b is the lowest ranking eclipse mapping target in our sample. We found that while *Ariel* will not be able to eclipse map it with adequate quantitative constraints using a reasonable number of repeated eclipse observations (≤20), the use of single phase curve observations can map lower ranking targets in a more time-efficient way. Hence, for *Ariel* to obtain a uniform data set of all of these best mapping targets, phase curves are the most advantageous strategy in order to facilitate a population-level study of adequate size.

(iv) WASP-43b is the only planet in our sample with eclipse maps constrained in latitude as well as longitude. We found that due to the small amplitude and short duration of latitudinal signals, smaller observatories like *Ariel* will not have the ability to robustly measure them in eclipse maps using a reasonable amount of data, requiring at minimum ten phase curves for this test case.

From these test cases, we determined that the most advantageous focus of a mapping survey with *Ariel* would be in constraining the longitudinal profiles of a large population of planets using a mixture of phase and eclipse mapping applied to full phase curves. From this, we would be able to characterize the first-order atmospheric dynamics of these targets and diagnose population-level trends.

In order to determine which targets would be best suited to such a survey, we used the methods of S. Boone et al. (2024) to rank all the best mapping targets for *Ariel*. We determined that there are 138 unique targets that are mappable with *Ariel* using our proposed observing strategy. By applying selection criteria, we devised a survey of 87 targets with $P \leq 4.2$ d that are mappable in at least 2/3 of the spectrographs, for which full phase curves would be observable

using only a quarter of the *Ariel* mission lifetime (B. Edwards & G. Tinetti 2022).

These survey targets span a range of irradiation temperatures (1370 − 4350 K), planetary radii (0.74 − 2.07 R_J), masses (0.3 − 19.7 M_J), and gravities [$\log(g) = 0.5 - 2.4$ ms^{-2}], which would enable us to both sample and control for the number of degenerate parameters that influence atmospheric dynamics at first-order. These 87 targets would supersede the previous largest survey of exoplanet atmospheric dynamics with *Spitzer* using 29 phase curves (L. Dang et al. 2025) by a factor of three. Hence, this survey would enable the most wide-ranging and comprehensive assessment of the population-level trends of transiting exoplanet atmospheric dynamics to date.

ACKNOWLEDGEMENTS

We thank the anonymous referee for their helpful and constructive review. DV acknowledges support from the European Space Agency (ESA) Archival Research Visitor Programme,[6] which is designed to increase the scientific return from ESA space science missions by twice a year funding six archival research projects. DV also acknowledges funding from the Science and Technology Facilities Council (STFC) grant ST/X508263/1 and the University of Bristol School of Physics HH Potter PhD Scholarship Fund. HRW was funded by UK Research and Innovation (UKRI) framework under the UK government's Horizon Europe funding guarantee for a European Research Council (ERC) Starter Grant [grant number EP/Y006313/1]. DV also acknowledges the input and encouragement of the *Ariel* Science Team and Ariel Consortium Phase Curve Working Group.

DATA AVAILABILITY

The simulation code and data products are available at 10.5281/zenodo.17245372, in addition to machine-readable versions of the full EMM rankings for *JWST* and *Ariel*, and the proposed survey targets.

REFERENCES

Batalha N. E. et al., 2017, PASP, 129, 064501
Beatty T. G., Marley M. S., Gaudi B. S., Colón K. D., Fortney J. J., Showman A. P., 2019, AJ, 158, 166
Bell T. J. et al., 2024, Nat. Astron., 8, 879
Beltz H., Rauscher E., Roman M. T., Guilliat A., 2022, AJ, 163, 35
Boone S., Grant D., Hammond M., 2024, MNRAS, 528, 596
Bouchy F. et al., 2005, A&A, 444, L15
Brown T. M., Charbonneau D., Gilliland R. L., Noyes R. W., Burrows A., 2001, ApJ, 552, 699
Challener R. C., Rauscher E., 2022, AJ, 163, 117
Challener R. C., Rauscher E., 2023, AJ, 166, 176
Challener R. C. et al., 2024, ApJ, 969, L32
Charbonneau D., Brown T. M., Latham D. W., Mayor M., 2000, ApJ, 529, L45
Charnay B. et al., 2022, Exp. Astron., 53, 417
Christiansen J. L. et al., 2025, Planet. Sci. J., 6, 186
Coulombe L.-P. et al., 2023, Nature, 620, 292
Cowan N. B., Agol E., 2008, ApJ, 678, L129
Dang L. et al., 2018, Nat. Astron., 2, 220
Dang L. et al., 2025, AJ, 169, 32
de Wit J., Gillon M., Demory B. O., Seager S., 2012, A&A, 548, A128
Deming D., Harrington J., Seager S., Richardson L. J., 2006, ApJ, 644, 560
Deming D. et al., 2013, ApJ, 774, 95
Dobbs-Dixon I., Agol E., Deming D., 2015, ApJ, 815, 60
Dyrek A., Ducrot E., Lagage P. O., Tremblin P., Kendrew S., Bouwman J., Bouffet R., 2024, A&A, 683, A212
Edwards B., Tinetti G., 2022, AJ, 164, 15
Espinoza N. et al., 2024, Nature, 632, 1017
Flowers E., Brogi M., Rauscher E., Kempton E. M. R., Chiavassa A., 2019, AJ, 157, 209
Gao P., Wakeford H. R., Moran S. E., Parmentier V., 2021, J. Geophys. Res. (Planets), 126, e06655
Grant D., Wakeford H. R., 2023, MNRAS, 519, 5114
Grant D., Wakeford H. R., 2024, J. Open Source Softw., 9, 6816
Grant D. et al., 2023, ApJ, 956, L32
Hammond M., Abbot D. S., 2022, MNRAS, 511, 2313
Hammond M., Lewis N. T., 2021, PNAS, 118, e2022705118
Hammond M. et al., 2024, AJ, 168, 4
Husser T.-O., Wende-von Berg S., Dreizler S., Homeier D., Reiners A., Barman T., Hauschildt P. H., 2013, A&A, 553, A6
Inglis J. et al., 2024, ApJ, 973, L41
Jones K., Espinoza N., 2020, J. Open Source Softw., 7, 2382
Kataria T., Showman A. P., Fortney J. J., Stevenson K. B., Line M. R., Kreidberg L., Bean J. L., Désert J.-M., 2015, ApJ, 801, 86
Kataria T., Sing D. K., Lewis N. K., Visscher C., Showman A. P., Fortney J. J., Marley M. S., 2016, ApJ, 821, 9
Kilpatrick B. M. et al., 2020, AJ, 159, 51
Knutson H. A. et al., 2007, Nature, 447, 183
Knutson H. A. et al., 2012, ApJ, 754, 22
Komacek T. D., Youdin A. N., 2017, ApJ, 844, 94
Lally M. et al., 2025, ApJ, 983, L13
Lewis N. T., Hammond M., 2022, ApJ, 941, 171
Luger R., Agol E., Foreman-Mackey D., Fleming D. P., Lustig-Yaeger J., Deitrick R., 2019, AJ, 157, 64
Majeau C., Agol E., Cowan N. B., 2012, ApJ, 747, L20
Mugnai L. V., Pascale E., Edwards B., Papageorgiou A., Sarkar S., 2020, Exp. Astron., 50, 303
Mukherjee S. et al., 2025, preprint (arXiv:2505.10910)
Murphy M. M. et al., 2023, AJ, 165, 107
Murphy M. M. et al., 2024, Nat. Astron., 8, 1562
Murphy M. M. et al., 2025, AJ, 170, 61
Parmentier V., Crossfield I. J. M., 2018, in Deeg H. J., Belmonte J. A., eds, Handbook of Exoplanets. Springer, Cham, p. 116
Parmentier V., Fortney J. J., Showman A. P., Morley C., Marley M. S., 2016, ApJ, 828, 22
Raftery A. E., 1995, Sociolog. Method., 25, 111
Rauscher E., Menou K., Seager S., Deming D., Cho J. Y. K., Hansen B. M. S., 2007, ApJ, 664, 1199
Rauscher E., Suri V., Cowan N. B., 2018, AJ, 156, 235
Roth A., Parmentier V., Hammond M., 2024, MNRAS, 531, 1056
Schlawin E., Challener R., Mansfield M., Rauscher E., Adams A., Lustig-Yaeger J., 2023, AJ, 165, 210
Schlawin E. et al., 2024, AJ, 168, 104
Showman A. P., Cooper C. S., Fortney J. J., Marley M. S., 2008, ApJ, 682, 559
Showman A. P., Lewis N. K., Fortney J. J., 2014, ApJ, 801, 95
Showman A. P., Tan X., Parmentier V., 2020, Space Sci. Rev., 216, 139
Sing D. K. et al., 2011, MNRAS, 416, 1443
Stevenson K. B. et al., 2014, Science, 346, 838
Tinetti G. et al., 2018, Exp. Astron., 46, 135
Valentine D., Challener R., Grant D., Hammond M., Lewis N., Taylor J., Wakeford H., 2024a, Unlocking New Dimensions in Eclipse Mapping with KELT-8b, JWST Proposal. Cycle 3, ID. #5687
Valentine D. et al., 2024b, AJ, 168, 123
Wakeford H. R., Sing D. K., 2015, A&A, 573, A122
Wakeford H. R. et al., 2025, preprint (arXiv:2506.22839)
Welbanks L., Madhusudhan N., Allard N. F., Hubeny I., Spiegelman F., Leininger T., 2019, ApJ, 887, L20
Xue Q., Bean J. L., Zhang M., Welbanks L., Lunine J., August P., 2024, ApJ, 963, L5
Zellem R. T. et al., 2014, ApJ, 790, 53
Zellem R. T. et al., 2019, PASP, 131, 094401

[6] https://www.cosmos.esa.int/web/esdc/visitor-programme

APPENDIX A: BEST ECLIPSE MAPPING TARGETS FOR ARIEL

Here, we tabulate the best eclipse mapping targets for the three *Ariel* spectrographs (NIRSpec, Table A1; AIRS Ch0, Table A2; and AIRS Ch1, Table A3) as identified by their analytically calculated eclipse mapping metrics (EMMs, S. Boone et al. 2024). We define a target to be 'eclipse mappable' if it has an EMM$< 90^\circ$ and $N_{\rm max} \geq 1$. We list the targets in order of their overall EMM.

Table A1. Best eclipse mapping targets for Ariel NIRSpec. These have EMM $< 90^\circ$ and $N_{\rm max} \geq 1$ for this spectrograph. We list these targets in order of their overall EMM ranking, include relevant system parameters, along with our calculated EMM$_x$, EMM$_x$, and $N_{\rm max}$ values (see the text for details).

Planet name	Rank	$T_{\rm eq}$ (K)	$R_{\rm p}$ ($R_{\rm J}$)	$M_{\rm p}$ ($M_{\rm J}$)	P (d)	b	K (mag)	$N_{\rm max}$	EMM$_x$ (deg)	EMM$_y$ (deg)	EMM (deg)
TOI-2109b	1	3072	1.35	5.02	0.67	0.75	9.07	3.0	32.3	28.7	43.2
WASP-189b	2	2636	1.62	1.99	2.72	0.48	6.06	3.4	22.0	40.3	45.9
KELT-20b	3	2263	1.74	3.38	3.47	0.5	7.42	3.0	24.7	42.4	49.1
KELT-7b	4	2089	1.6	1.39	2.73	0.57	7.54	2.6	29.4	42.4	51.6
TOI-1431b	5	2395	1.49	3.12	2.65	0.88	7.44	2.9	46.7	24.8	52.8
WASP-19b	6	2117	1.42	1.15	0.79	0.67	10.48	2.2	36.3	40.7	54.5
KELT-4Ab	7	1822	1.7	0.9	2.99	0.69	8.69	2.1	39.5	41.3	57.1
WASP-87b	8	2313	1.38	2.18	1.68	0.6	9.55	2.1	35.5	46.9	58.8
WASP-178b	9	2469	1.81	1.66	3.34	0.54	9.7	2.3	31.8	49.6	58.9
WASP-167b	10	2363	1.58	8.0	2.02	0.77	9.76	2.1	45.4	37.7	59.0
WASP-18b	11	2504	1.24	10.2	0.94	0.37	8.13	3.1	22.1	55.0	59.3
KELT-14b	12	1961	1.74	1.28	1.71	0.86	9.42	2.4	51.5	30.3	59.7
KELT-17b	13	2090	1.52	1.31	3.08	0.57	8.65	2.2	34.0	49.2	59.8
KELT-19Ab	14	1938	1.91	4.07	4.61	0.6	9.2	2.0	36.5	48.8	61.0
WASP-14b	15	1920	1.38	8.84	2.24	0.56	8.62	2.1	34.4	50.6	61.2
HD189733b	16	1193	1.13	1.13	2.22	0.67	5.54	1.9	41.6	46.0	62.0
KELT-3b	17	1952	1.56	1.94	2.7	0.53	8.66	2.0	35.0	55.6	65.7
HD209458b	18	1477	1.39	0.73	3.52	0.49	6.31	2.1	32.2	57.6	66.0
HAT-P−60b	19	1773	1.63	0.57	4.79	0.67	8.37	1.7	44.8	49.9	67.1
TOI-778b	20	1710	1.37	2.8	4.63	0.7	8.06	1.7	47.4	48.7	68.0
KELT-23Ab	21	1565	1.32	0.94	2.26	0.57	8.9	1.8	39.0	55.8	68.1
HAT-P−30b	22	1699	1.44	0.83	2.81	0.77	9.15	1.7	52.9	44.3	69.0
XO-7b	23	1744	1.37	0.71	2.86	0.73	9.24	1.6	51.6	47.9	70.4
KELT-8b	24	1571	1.62	0.66	3.24	0.86	9.18	1.9	61.5	36.9	71.7
WASP-43b	25	1379	0.93	1.78	0.81	0.66	9.27	1.6	47.8	55.0	72.8
XO-6b	26	1577	2.07	4.4	3.77	0.63	9.25	1.6	46.2	56.4	72.8
HD202772Ab	27	2133	1.54	1.02	3.31	0.41	6.96	2.2	30.2	66.4	73.0
HAT-P−7b	28	2272	1.51	1.84	2.2	0.47	9.33	1.9	34.7	64.5	73.3
HAT-P−56b	29	1866	1.51	2.31	2.79	0.85	9.83	1.8	62.3	39.0	73.5
WASP-101b	30	1566	1.43	0.51	3.59	0.72	9.07	1.5	53.6	51.1	74.1
WASP-54b	31	1747	1.58	0.59	3.69	0.53	9.04	1.7	39.7	62.8	74.3
WASP-12b	32	2594	1.94	1.46	1.09	0.34	10.19	2.6	25.3	70.3	74.7
WASP-120b	33	1876	1.47	4.85	3.61	0.77	9.88	1.5	57.7	48.2	75.2
WASP-135b	34	1720	1.3	1.9	1.4	0.76	11.04	1.5	57.1	49.2	75.4
WASP-48b	35	1933	1.5	0.8	2.14	0.81	10.37	1.6	61.1	44.7	75.7
WASP-24b	36	1827	1.38	1.24	2.34	0.61	10.15	1.5	46.5	60.0	75.9
KELT-12b	37	1799	1.78	0.95	5.03	0.59	9.36	1.6	44.7	61.7	76.2
GPX-1b	38	2293	1.47	19.7	1.74	0.82	11.18	1.6	62.7	44.2	76.7
WASP-3b	39	2086	1.42	2.43	1.85	0.41	9.36	2.1	31.6	71.2	77.9
TOI-1937Ab	40	2096	1.25	2.01	0.95	0.87	11.23	1.7	68.0	39.3	78.5
TrES-2b	41	1581	1.36	1.49	2.47	0.77	9.85	1.4	60.4	50.6	78.8
HATS-56b	42	1901	1.69	0.6	4.32	0.69	10.25	1.4	55.0	57.7	79.7
HD149026b	43	1693	0.74	0.38	2.88	0.63	6.82	1.4	50.8	62.3	80.4
WASP-33b	44	2781	1.59	2.09	1.22	0.21	7.47	4.0	16.9	78.7	80.5
WASP-79b	45	1716	1.53	0.85	3.66	0.5	9.06	1.6	40.7	70.0	81.0
WASP-36b	46	1747	1.33	2.36	1.54	0.69	11.29	1.3	56.6	58.7	81.6
HAT-P−6b	47	1761	1.48	1.32	3.85	0.54	9.31	1.5	44.5	68.5	81.6
WASP-104b	48	1514	1.14	1.27	1.76	0.73	9.88	1.3	59.3	56.3	81.8
HAT-P−13b	49	1727	1.27	0.85	2.92	0.62	8.98	1.4	50.9	65.2	82.7
WASP-136b	50	1745	1.38	1.51	5.22	0.59	8.8	1.4	49.2	66.5	82.7
WASP-90b	51	1840	1.63	0.63	3.92	0.84	10.25	1.5	69.5	45.0	82.8
TOI-640b	52	1747	1.77	0.88	5.0	0.89	9.24	1.7	74.1	38.5	83.5
TOI-1333b	53	1680	1.4	2.37	4.72	0.52	8.27	1.5	43.8	71.3	83.7
WASP-142b	54	1992	1.53	0.84	2.05	0.77	11.44	1.3	66.2	54.1	85.5
WASP-31b	55	1574	1.55	0.48	3.41	0.78	10.65	1.2	68.1	54.4	87.2
TrES-4b	56	1708	1.61	0.78	3.55	0.82	10.33	1.3	72.1	49.5	87.4
WASP-92b	57	1879	1.46	0.8	2.17	0.61	11.52	1.3	53.4	69.7	87.8

Table A1 – *continued*

Planet name	Rank	T_{eq} (K)	R_p (R_J)	M_p (M_J)	P (d)	b	K (mag)	N_{max}	EMM_x (deg)	EMM_y (deg)	EMM (deg)
WASP-16b	58	1440	1.22	1.24	3.12	0.65	9.59	1.2	57.7	67.1	88.5
HATS-67b	59	2191	1.68	1.45	1.61	0.86	12.33	1.4	76.4	45.0	88.7
KELT-11b	60	1703	1.35	0.17	4.74	0.41	6.12	1.8	36.2	81.0	88.7
WASP-71b	61	1830	1.18	1.39	2.9	0.55	9.32	1.3	49.0	74.0	88.7
HAT-P−2b	62	1389	1.13	9.02	5.63	0.71	7.6	1.2	62.6	62.8	88.7
TOI-2236b	63	1687	1.28	1.58	3.53	0.77	9.96	1.2	68.1	56.9	88.7
Qatar-1b	64	1416	1.14	1.29	1.42	0.65	10.41	1.2	57.5	67.8	88.9
WASP-20b	65	1378	1.46	0.31	4.9	0.72	9.39	1.2	64.1	62.0	89.1
WASP-50b	66	1394	1.17	1.47	1.96	0.67	9.97	1.2	60.1	66.6	89.7

Table A2. Best eclipse mapping targets for Ariel AIRS Ch0. These have EMM $< 90^\circ$ and $N_{max} \geq 1$ for this spectrograph. We list these targets in order of their overall EMM ranking, include relevant system parameters, along with our calculated EMM_x, EMM_x, and N_{max} values (see text for details).

Planet name	Rank	T_{eq} (K)	R_p (R_J)	M_p (M_J)	P (d)	b	K (mag)	N_{max}	EMM_x (deg)	EMM_y (deg)	EMM (deg)
HD189733b	1	1193	1.13	1.13	2.22	0.67	5.54	4.1	21.6	23.9	32.2
WASP-189b	2	2636	1.62	1.99	2.72	0.48	6.06	4.0	19.0	34.8	39.6
KELT-20b	3	2263	1.74	3.38	3.47	0.5	7.42	3.6	21.2	36.4	42.1
HD209458b	4	1477	1.39	0.73	3.52	0.49	6.31	3.6	20.6	36.9	42.2
KELT-7b	5	2089	1.6	1.39	2.73	0.57	7.54	3.0	25.6	36.8	44.8
TOI-1431b	6	2395	1.49	3.12	2.65	0.88	7.44	3.3	41.2	21.9	46.7
TOI-2109b	7	3072	1.35	5.02	0.67	0.75	9.07	2.5	36.8	32.7	49.3
KELT-4Ab	8	1822	1.7	0.9	2.99	0.69	8.69	2.5	34.6	36.1	50.0
KELT-23Ab	9	1565	1.32	0.94	2.26	0.57	8.9	2.4	31.1	44.4	54.2
WASP-19b	10	2117	1.42	1.15	0.79	0.67	10.48	2.3	36.2	40.4	54.3
TOI-778b	11	1710	1.37	2.8	4.63	0.7	8.06	2.2	37.9	39.0	54.4
WASP-43b	12	1379	0.93	1.78	0.81	0.66	9.27	2.3	35.8	41.2	54.5
KELT-19Ab	13	1938	1.91	4.07	4.61	0.6	9.2	2.3	32.7	43.7	54.6
WASP-14b	14	1920	1.38	8.84	2.24	0.56	8.62	2.4	31.0	45.6	55.1
KELT-17b	15	2090	1.52	1.31	3.08	0.57	8.65	2.4	31.5	45.6	55.4
KELT-8b	16	1571	1.62	0.66	3.24	0.86	9.18	2.5	47.8	28.6	55.7
KELT-14b	17	1961	1.74	1.28	1.71	0.86	9.42	2.5	48.3	28.3	56.0
HAT-P−60b	18	1773	1.63	0.57	4.79	0.67	8.37	2.2	37.6	41.8	56.2
XO-6b	19	1577	2.07	4.4	3.77	0.63	9.25	2.1	36.5	44.6	57.6
HAT-P−30b	20	1699	1.44	0.83	2.81	0.77	9.15	2.1	45.3	37.9	59.1
WASP-101b	21	1566	1.43	0.51	3.59	0.72	9.07	2.0	43.2	41.2	59.7
WASP-87b	22	2313	1.38	2.18	1.68	0.6	9.55	2.1	36.2	47.8	60.0
HD149026b	23	1693	0.74	0.38	2.88	0.63	6.82	2.0	38.1	46.6	60.2
WASP-178b	24	2469	1.81	1.66	3.34	0.54	9.7	2.2	32.4	50.7	60.2
WASP-18b	25	2504	1.24	10.2	0.94	0.37	8.13	3.1	22.5	56.0	60.3
KELT-3b	26	1952	1.56	1.94	2.7	0.53	8.66	2.2	32.3	51.3	60.6
HAT-P−2b	27	1389	1.13	9.02	5.63	0.71	7.6	1.9	42.9	43.0	60.7
WASP-167b	28	2363	1.58	8.0	2.02	0.77	9.76	2.0	47.0	39.0	61.1
XO-7b	29	1744	1.37	0.71	2.86	0.73	9.24	1.9	44.9	41.6	61.2
WASP-69b	30	988	1.11	0.29	3.87	0.65	7.46	1.9	40.0	46.9	61.6
HD202772Ab	31	2133	1.54	1.02	3.31	0.41	6.96	2.7	25.8	56.8	62.4
WASP-54b	32	1747	1.58	0.59	3.69	0.53	9.04	2.1	34.2	54.1	64.0
HAT-P−1b	33	1322	1.32	0.52	4.47	0.78	8.86	1.8	50.6	40.8	65.0
KELT-11b	34	1703	1.35	0.17	4.74	0.41	6.12	2.6	26.6	59.4	65.1
TrES-2b	35	1581	1.36	1.49	2.47	0.77	9.85	1.8	50.2	42.1	65.6
WASP-20b	36	1378	1.46	0.31	4.9	0.72	9.39	1.7	47.6	46.0	66.2
WASP-104b	37	1514	1.14	1.27	1.76	0.73	9.88	1.7	48.1	45.6	66.3
WASP-135b	38	1720	1.3	1.9	1.4	0.76	11.04	1.7	50.8	43.7	67.0
HAT-P−56b	39	1866	1.51	2.31	2.79	0.85	9.83	2.0	57.0	35.7	67.2
KELT-12b	40	1799	1.78	0.95	5.03	0.59	9.36	1.8	39.5	54.6	67.4
TOI-1333b	41	1680	1.4	2.37	4.72	0.52	8.27	1.9	35.9	58.5	68.6
WASP-16b	42	1440	1.22	1.24	3.12	0.65	9.59	1.7	44.9	52.2	68.9
WASP-50b	43	1394	1.17	1.47	1.96	0.67	9.97	1.7	46.2	51.2	68.9
WASP-120b	44	1876	1.47	4.85	3.61	0.77	9.88	1.7	53.0	44.3	69.1
WASP-24b	45	1827	1.38	1.24	2.34	0.61	10.15	1.7	42.5	54.8	69.3
Qatar-1b	46	1416	1.14	1.29	1.42	0.65	10.41	1.7	44.9	52.9	69.4
WASP-131b	47	1460	1.22	0.27	5.32	0.74	8.57	1.7	51.6	46.4	69.4
WASP-79b	48	1716	1.53	0.85	3.66	0.5	9.06	2.0	35.0	60.2	69.6
WASP-2b	49	1314	1.08	0.93	2.15	0.75	9.63	1.6	52.1	46.4	69.8

Table A2 – *continued*

Planet name	Rank	T_{eq} (K)	R_p (R_J)	M_p (M_J)	P (d)	b	K (mag)	N_{max}	EMM$_x$ (deg)	EMM$_y$ (deg)	EMM (deg)
WASP-52b	50	1299	1.27	0.46	1.75	0.6	10.09	1.7	42.3	56.3	70.4
WASP-136b	51	1745	1.38	1.51	5.22	0.59	8.8	1.7	42.2	57.1	71.0
TOI-640b	52	1747	1.77	0.88	5.0	0.89	9.24	2.0	63.3	32.9	71.4
WASP-48b	53	1933	1.5	0.8	2.14	0.81	10.37	1.7	57.9	42.4	71.8
WASP-49b	54	1366	1.11	0.37	2.78	0.75	9.75	1.6	53.8	47.6	71.9
Gaia-2b	55	1314	1.32	0.82	3.69	0.79	9.74	1.6	57.0	44.0	72.0
HAT-P−6b	56	1761	1.48	1.32	3.85	0.54	9.31	1.8	39.3	60.5	72.1
HAT-P−22b	57	1324	1.15	2.47	3.21	0.43	7.84	2.1	31.3	65.0	72.1
WASP-123b	58	1522	1.32	0.9	2.98	0.53	9.36	1.8	38.3	61.6	72.5
HAT-P−13b	59	1727	1.27	0.85	2.92	0.62	8.98	1.6	44.7	57.2	72.6
WASP-31b	60	1574	1.55	0.48	3.41	0.78	10.65	1.6	57.1	45.7	73.1
WASP-7b	61	1486	1.33	0.96	4.95	0.48	8.4	1.9	35.2	64.2	73.3
WASP-13b	62	1450	1.22	0.36	4.35	0.67	9.12	1.5	49.3	54.5	73.5
WASP-36b	63	1747	1.33	2.36	1.54	0.69	11.29	1.5	51.2	53.1	73.8
HAT-P−7b	64	2272	1.51	1.84	2.2	0.47	9.33	1.9	35.2	65.3	74.2
HATS-56b	65	1901	1.69	0.6	4.32	0.69	10.25	1.5	51.4	53.9	74.5
WASP-3b	66	2086	1.42	2.43	1.85	0.41	9.36	2.2	30.5	68.9	75.3
WASP-90b	67	1840	1.63	0.63	3.92	0.84	10.25	1.7	63.4	41.1	75.5
WASP-119b	68	1566	1.4	1.23	2.5	0.57	10.54	1.6	43.1	62.6	76.0
TOI-3331Ab	69	1487	1.16	2.27	2.02	0.57	9.91	1.6	43.8	63.0	76.7
TOI-905b	70	1192	1.17	0.67	3.74	0.82	9.45	1.6	63.3	43.9	77.1
TrES-4b	71	1708	1.61	0.78	3.55	0.82	10.33	1.6	63.6	43.7	77.2
TOI-4463Ab	72	1394	1.18	0.79	2.88	0.88	9.4	1.8	68.1	36.5	77.3
TOI-2236b	73	1687	1.28	1.58	3.53	0.77	9.96	1.5	59.4	49.6	77.4
HATS-1b	74	1370	1.3	1.86	3.45	0.7	10.58	1.4	54.7	55.1	77.7
WASP-15b	75	1626	1.41	0.54	3.75	0.53	9.69	1.6	41.2	66.1	77.9
TOI-1937Ab	76	2096	1.25	2.01	0.95	0.87	11.23	1.7	67.8	39.2	78.3
HAT-P−46b	77	1453	1.28	0.49	4.46	0.7	9.92	1.4	54.5	56.3	78.4
TOI-157b	78	1591	1.29	1.18	2.08	0.8	10.89	1.5	62.9	46.9	78.4
GPX-1b	79	2293	1.47	19.7	1.74	0.82	11.18	1.5	64.9	45.8	79.4
WASP-46b	80	1639	1.17	1.91	1.43	0.73	11.4	1.4	58.3	54.2	79.6
TOI-622b	81	1382	0.82	0.3	6.4	0.63	7.86	1.4	50.6	62.0	80.0
WASP-71b	82	1830	1.18	1.39	2.9	0.55	9.32	1.5	44.4	67.1	80.5
WASP-33b	83	2781	1.59	2.09	1.22	0.21	7.47	4.0	16.9	78.8	80.6
HATS-65b	84	1633	1.5	0.82	3.11	0.67	11.1	1.4	53.8	60.2	80.7
WASP-17b	85	1699	1.93	0.48	3.74	0.35	10.22	1.8	35.4	73.0	81.1
WASP-12b	86	2594	1.94	1.46	1.09	0.34	10.19	2.4	27.6	76.6	81.4
WASP-75b	87	1705	1.27	1.07	2.48	0.89	10.06	1.8	72.6	37.0	81.5
HAT-P−20b	88	969	0.87	7.25	2.88	0.63	8.6	1.4	51.5	63.8	82.0
KPS-1b	89	1448	1.03	1.09	1.71	0.75	10.93	1.3	61.8	54.1	82.1
TOI-677b	90	1066	1.17	1.24	11.24	0.72	8.43	1.3	59.3	56.9	82.2
TOI-615b	91	1668	1.69	0.44	4.66	0.48	9.67	1.6	39.6	72.1	82.3
TOI-3894b	92	1531	1.36	0.82	4.33	0.72	10.48	1.3	59.3	57.4	82.5
WASP-164b	93	1608	1.13	2.13	1.78	0.82	10.96	1.4	68.2	46.8	82.7
WASP-92b	94	1879	1.46	0.8	2.17	0.61	11.52	1.4	50.4	65.8	82.9
WASP-142b	95	1992	1.53	0.84	2.05	0.77	11.44	1.3	64.6	52.7	83.4
WASP-32b	96	1454	0.96	2.63	2.72	0.76	10.16	1.3	64.1	54.4	84.1
TOI-1194b	97	1382	0.78	0.38	2.31	0.8	9.34	1.3	67.4	50.7	84.3
HD221416b	98	1198	0.84	0.19	14.28	0.67	6.04	1.3	56.3	63.1	84.5
TOI-4377b	99	1870	1.35	0.96	4.38	0.6	9.15	1.3	50.7	68.3	85.0
WASP-170b	100	1426	1.1	1.6	2.34	0.69	10.72	1.2	59.1	62.0	85.7
HAT-P−50b	101	1855	1.29	1.35	3.12	0.63	10.5	1.3	54.5	66.5	85.9
K2-29b	102	1167	1.19	0.73	3.26	0.62	10.06	1.3	53.0	68.0	86.2
WASP-173Ab	103	1871	1.2	3.69	1.39	0.4	10.0	1.8	34.8	79.2	86.5
HAT-P−16b	104	1627	1.29	4.19	2.78	0.42	9.55	1.7	36.8	78.4	86.6
TOI-4137b	105	1570	1.21	1.44	3.8	0.58	10.0	1.3	50.9	70.5	87.0
WASP-153b	106	1712	1.55	0.39	3.33	0.61	11.05	1.3	53.7	69.1	87.5
TrES-5b	107	1483	1.19	1.79	1.48	0.61	11.59	1.3	53.2	69.6	87.6
WASP-163b	108	1634	1.2	1.87	1.61	0.45	10.15	1.6	40.0	78.9	88.4
HATS-58Ab	109	1718	1.1	1.03	4.22	0.66	10.29	1.2	58.1	67.0	88.7
TOI-1820b	110	1375	1.14	2.3	4.86	0.85	9.51	1.4	75.6	47.3	89.2
KELT-21b	111	2053	1.59	3.91	3.61	0.42	10.09	1.7	37.9	81.2	89.6
TOI-4791b	112	1472	1.11	2.31	4.28	0.66	10.02	1.2	58.9	67.6	89.7
K2-107b	113	1804	1.43	0.84	3.31	0.75	11.21	1.2	67.4	59.4	89.8

Table A3. Best eclipse mapping targets for Ariel AIRS Ch1. These have EMM $< 90^\circ$ and $N_{\rm max} \geq 1$ for this spectrograph. We list these targets in order of their overall EMM ranking, include relevant system parameters, along with our calculated EMM_x, EMM_x, and $N_{\rm max}$ values (see the text for details).

Planet name	Rank	$T_{\rm eq}$ (K)	$R_{\rm p}$ ($\mathrm{R_J}$)	$M_{\rm p}$ ($\mathrm{M_J}$)	P (d)	b	K (mag)	$N_{\rm max}$	EMM_x (deg)	EMM_y (deg)	EMM (deg)
HD189733b	1	1193	1.13	1.13	2.22	0.67	5.54	5.2	17.7	19.6	26.4
HD209458b	2	1477	1.39	0.73	3.52	0.49	6.31	4.1	18.6	33.2	38.1
WASP-189b	3	2636	1.62	1.99	2.72	0.48	6.06	3.8	19.6	35.9	40.9
KELT-20b	4	2263	1.74	3.38	3.47	0.5	7.42	3.5	21.3	36.6	42.3
KELT-7b	5	2089	1.6	1.39	2.73	0.57	7.54	3.0	25.8	37.2	45.2
WASP-69b	6	988	1.11	0.29	3.87	0.65	7.46	2.7	30.5	35.7	46.9
TOI-1431b	7	2395	1.49	3.12	2.65	0.88	7.44	3.3	42.0	22.3	47.5
KELT-4Ab	8	1822	1.7	0.9	2.99	0.69	8.69	2.5	34.0	35.5	49.2
WASP-43b	9	1379	0.93	1.78	0.81	0.66	9.27	2.5	32.8	37.8	50.1
KELT-23Ab	10	1565	1.32	0.94	2.26	0.57	8.9	2.6	29.2	41.7	50.9
TOI-778b	11	1710	1.37	2.8	4.63	0.7	8.06	2.4	36.2	37.3	52.0
KELT-8b	12	1571	1.62	0.66	3.24	0.86	9.18	2.7	44.9	26.9	52.4
KELT-19Ab	13	1938	1.91	4.07	4.61	0.6	9.2	2.4	31.8	42.5	53.1
XO-6b	14	1577	2.07	4.4	3.77	0.63	9.25	2.3	34.0	41.6	53.7
HAT-P−2b	15	1389	1.13	9.02	5.63	0.71	7.6	2.3	38.1	38.2	54.0
TOI-2109b	16	3072	1.35	5.02	0.67	0.75	9.07	2.3	40.5	36.0	54.2
HAT-P−60b	17	1773	1.63	0.57	4.79	0.67	8.37	2.2	36.6	40.7	54.7
WASP-14b	18	1920	1.38	8.84	2.24	0.56	8.62	2.4	30.9	45.3	54.8
KELT-17b	19	2090	1.52	1.31	3.08	0.57	8.65	2.4	31.3	45.2	54.9
WASP-101b	20	1566	1.43	0.51	3.59	0.72	9.07	2.2	40.5	38.6	56.0
WASP-19b	21	2117	1.42	1.15	0.79	0.67	10.48	2.1	37.8	42.3	56.8
KELT-14b	22	1961	1.74	1.28	1.71	0.86	9.42	2.5	49.0	28.8	56.8
HAT-P−30b	23	1699	1.44	0.83	2.81	0.77	9.15	2.1	43.8	36.7	57.1
HAT-P−1b	24	1322	1.32	0.52	4.47	0.78	8.86	2.2	44.6	36.0	57.3
HD149026b	25	1693	0.74	0.38	2.88	0.63	6.82	2.1	36.3	44.5	57.4
WASP-20b	26	1378	1.46	0.31	4.9	0.72	9.39	2.0	42.8	41.4	59.6
XO-7b	27	1744	1.37	0.71	2.86	0.73	9.24	2.0	43.7	40.6	59.6
KELT-3b	28	1952	1.56	1.94	2.7	0.53	8.66	2.2	32.4	51.4	60.8
WASP-178b	29	2469	1.81	1.66	3.34	0.54	9.7	2.1	33.5	52.3	62.1
WASP-54b	30	1747	1.58	0.59	3.69	0.53	9.04	2.1	33.3	52.7	62.3
WASP-2b	31	1314	1.08	0.93	2.15	0.75	9.63	1.9	46.7	41.6	62.6
WASP-104b	32	1514	1.14	1.27	1.76	0.73	9.88	1.9	45.4	43.1	62.6
KELT-11b	33	1703	1.35	0.17	4.74	0.41	6.12	2.7	25.5	57.1	62.6
TrES-2b	34	1581	1.36	1.49	2.47	0.77	9.85	1.9	48.0	40.3	62.7
WASP-87b	35	2313	1.38	2.18	1.68	0.6	9.55	2.0	37.9	50.1	62.8
WASP-52b	36	1299	1.27	0.46	1.75	0.6	10.09	2.0	37.9	50.5	63.2
WASP-50b	37	1394	1.17	1.47	1.96	0.67	9.97	1.9	42.4	47.1	63.3
HAT-P−20b	38	969	0.87	7.25	2.88	0.63	8.6	1.9	39.8	49.3	63.4
HD202772Ab	39	2133	1.54	1.02	3.31	0.41	6.96	2.6	26.3	57.8	63.5
WASP-16b	40	1440	1.22	1.24	3.12	0.65	9.59	1.9	41.4	48.1	63.5
HAT-P−22b	41	1324	1.15	2.47	3.21	0.43	7.84	2.5	27.6	57.3	63.6
WASP-131b	42	1460	1.22	0.27	5.32	0.74	8.57	1.8	47.4	42.6	63.7
WASP-18b	43	2504	1.24	10.2	0.94	0.37	8.13	2.9	23.9	59.3	63.9
WASP-167b	44	2363	1.58	8.0	2.02	0.77	9.76	1.9	49.3	40.9	64.0
Gaia-2b	45	1314	1.32	0.82	3.69	0.79	9.74	1.9	50.8	39.2	64.2
Qatar-1b	46	1416	1.14	1.29	1.42	0.65	10.41	1.8	41.8	49.3	64.6
WASP-49b	47	1366	1.11	0.37	2.78	0.75	9.75	1.8	48.8	43.2	65.2
TOI-1333b	48	1680	1.4	2.37	4.72	0.52	8.27	2.0	34.3	55.9	65.6
TOI-677b	49	1066	1.17	1.24	11.24	0.72	8.43	1.8	47.4	45.5	65.7
TOI-905b	50	1192	1.17	0.67	3.74	0.82	9.45	1.9	54.0	37.5	65.8
KELT-12b	51	1799	1.78	0.95	5.03	0.59	9.36	1.9	38.8	53.6	66.1
WASP-135b	52	1720	1.3	1.9	1.4	0.76	11.04	1.8	50.3	43.4	66.4
HAT-P−56b	53	1866	1.51	2.31	2.79	0.85	9.83	2.0	56.7	35.5	66.9
WASP-7b	54	1486	1.33	0.96	4.95	0.48	8.4	2.1	32.3	58.9	67.2
WASP-79b	55	1716	1.53	0.85	3.66	0.5	9.06	2.0	33.8	58.1	67.2
WASP-13b	56	1450	1.22	0.36	4.35	0.67	9.12	1.7	45.5	50.3	67.8
WASP-123b	57	1522	1.32	0.9	2.98	0.53	9.36	1.9	35.9	57.8	68.1
WASP-120b	58	1876	1.47	4.85	3.61	0.77	9.88	1.7	52.8	44.1	68.8
WASP-136b	59	1745	1.38	1.51	5.22	0.59	8.8	1.8	41.0	55.5	69.0
WASP-24b	60	1827	1.38	1.24	2.34	0.61	10.15	1.7	42.3	54.6	69.0
TOI-640b	61	1747	1.77	0.88	5.0	0.89	9.24	2.1	61.5	32.0	69.3
WASP-31b	62	1574	1.55	0.48	3.41	0.78	10.65	1.7	54.6	43.7	69.9
TOI-4463Ab	63	1394	1.18	0.79	2.88	0.88	9.4	2.0	61.9	33.1	70.2

Table A3 – *continued*

Planet name	Rank	T_{eq} (K)	R_p (R_J)	M_p (M_J)	P (d)	b	K (mag)	N_{max}	EMM$_x$ (deg)	EMM$_y$ (deg)	EMM (deg)
HAT-P−6b	64	1761	1.48	1.32	3.85	0.54	9.31	1.8	38.3	59.0	70.3
HATS-1b	65	1370	1.3	1.86	3.45	0.7	10.58	1.6	50.0	50.4	71.0
HAT-P−13b	66	1727	1.27	0.85	2.92	0.62	8.98	1.7	43.8	56.0	71.1
TOI-1811b	67	962	0.99	0.97	3.71	0.75	9.64	1.6	53.8	47.0	71.4
TOI-622b	68	1382	0.82	0.3	6.4	0.63	7.86	1.6	45.3	55.5	71.7
HD221416b	69	1198	0.84	0.19	14.28	0.67	6.04	1.6	48.0	53.8	72.1
TOI-3331Ab	70	1487	1.16	2.27	2.02	0.57	9.91	1.7	41.2	59.3	72.2
HAT-P−46b	71	1453	1.28	0.49	4.46	0.7	9.92	1.6	50.5	52.2	72.6
WASP-119b	72	1566	1.4	1.23	2.5	0.57	10.54	1.7	41.3	60.0	72.8
WASP-48b	73	1933	1.5	0.8	2.14	0.81	10.37	1.6	59.0	43.2	73.1
WASP-36b	74	1747	1.33	2.36	1.54	0.69	11.29	1.5	51.1	53.0	73.6
K2-29b	75	1167	1.19	0.73	3.26	0.62	10.06	1.6	45.5	58.4	74.0
WASP-15b	76	1626	1.41	0.54	3.75	0.53	9.69	1.7	39.4	63.3	74.5
HATS-56b	77	1901	1.69	0.6	4.32	0.69	10.25	1.5	51.6	54.0	74.7
TOI-4145Ab	78	1075	1.19	0.43	4.07	0.8	10.29	1.6	59.8	44.9	74.7
WASP-90b	79	1840	1.63	0.63	3.92	0.84	10.25	1.7	63.0	40.8	75.0
TOI-2236b	80	1687	1.28	1.58	3.53	0.77	9.96	1.5	57.7	48.2	75.2
TrES-4b	81	1708	1.61	0.78	3.55	0.82	10.33	1.6	62.3	42.8	75.6
TOI-157b	82	1591	1.29	1.18	2.08	0.8	10.89	1.5	61.1	45.5	76.2
WASP-3b	83	2086	1.42	2.43	1.85	0.41	9.36	2.1	31.2	70.5	77.1
TOI-1194b	84	1382	0.78	0.38	2.31	0.8	9.34	1.5	61.6	46.4	77.1
HAT-P−7b	85	2272	1.51	1.84	2.2	0.47	9.33	1.8	36.7	68.1	77.4
KPS-1b	86	1448	1.03	1.09	1.71	0.75	10.93	1.4	58.4	51.1	77.6
WASP-32b	87	1454	0.96	2.63	2.72	0.76	10.16	1.4	59.6	50.7	78.3
TOI-3894b	88	1531	1.36	0.82	4.33	0.72	10.48	1.4	56.4	54.6	78.5
HATS-65b	89	1633	1.5	0.82	3.11	0.67	11.1	1.4	52.4	58.6	78.6
WASP-46b	90	1639	1.17	1.91	1.43	0.73	11.4	1.4	57.6	53.6	78.6
WASP-17b	91	1699	1.93	0.48	3.74	0.35	10.22	1.9	34.4	70.8	78.8
TOI-615b	92	1668	1.69	0.44	4.66	0.48	9.67	1.7	38.0	69.3	79.0
WASP-91b	93	1144	1.03	1.34	2.8	0.52	9.71	1.6	41.0	67.9	79.3
WASP-185b	94	1159	1.25	0.98	9.39	0.72	9.51	1.4	57.5	54.8	79.4
WASP-75b	95	1705	1.27	1.07	2.48	0.89	10.06	1.8	70.9	36.1	79.5
WASP-71b	96	1830	1.18	1.39	2.9	0.55	9.32	1.5	44.1	66.5	79.8
TOI-4641b	97	997	0.73	3.87	22.09	0.79	6.58	1.4	63.3	48.7	79.8
WASP-170b	98	1426	1.1	1.6	2.34	0.69	10.72	1.4	55.4	58.2	80.3
WASP-164b	99	1608	1.13	2.13	1.78	0.82	10.96	1.5	66.4	45.5	80.5
TOI-1820b	100	1375	1.14	2.3	4.86	0.85	9.51	1.5	68.7	43.0	81.0
WASP-98b	101	1170	1.14	0.92	2.96	0.69	11.28	1.3	56.1	58.8	81.3
WASP-8b	102	968	1.13	2.54	8.16	0.42	8.09	1.9	34.5	73.9	81.5
TOI-1937Ab	103	2096	1.25	2.01	0.95	0.87	11.23	1.6	71.0	41.1	82.0
HAT-P−59b	104	1276	1.12	1.54	4.14	0.83	10.21	1.5	68.6	45.8	82.5
TOI-4137b	105	1570	1.21	1.44	3.8	0.58	10.0	1.4	48.5	67.2	82.9
HAT-P−16b	106	1627	1.29	4.19	2.78	0.42	9.55	1.8	35.2	75.1	82.9
HAT-P−54b	107	821	0.94	0.76	3.8	0.74	10.33	1.3	61.4	56.3	83.3
TOI-257b	108	1028	0.64	0.14	18.39	0.64	6.26	1.3	53.5	64.0	83.4
GPX-1b	109	2293	1.47	19.7	1.74	0.82	11.18	1.4	68.4	48.2	83.7
TOI-1173b	110	943	0.82	0.09	7.06	0.78	9.13	1.3	65.3	52.7	83.9
TOI-4791b	111	1472	1.11	2.31	4.28	0.66	10.02	1.3	55.1	63.3	83.9
WASP-92b	112	1879	1.46	0.8	2.17	0.61	11.52	1.3	51.2	66.8	84.2
TrES-5b	113	1483	1.19	1.79	1.48	0.61	11.59	1.3	51.2	67.0	84.3
Gaia-1b	114	1278	1.23	1.68	3.05	0.68	11.27	1.3	57.6	61.8	84.5
WASP-96b	115	1286	1.2	0.48	3.43	0.71	10.91	1.3	60.2	59.4	84.6
WASP-33b	116	2781	1.59	2.09	1.22	0.21	7.47	3.8	17.8	82.8	84.6
HATS-58Ab	117	1718	1.1	1.03	4.22	0.66	10.29	1.3	55.6	64.1	84.8
HAT-P−27b	118	1188	1.02	0.62	3.04	0.87	10.11	1.6	74.1	41.6	85.0
WASP-53b	119	1055	1.07	2.13	3.31	0.56	10.39	1.4	47.9	70.5	85.2
TOI-4377b	120	1870	1.35	0.96	4.38	0.6	9.15	1.3	51.0	68.8	85.6
WASP-163b	121	1634	1.2	1.87	1.61	0.45	10.15	1.6	39.0	76.9	86.2
HAT-P−50b	122	1855	1.29	1.35	3.12	0.63	10.5	1.3	54.6	66.7	86.2
WASP-142b	123	1992	1.53	0.84	2.05	0.77	11.44	1.3	66.8	54.5	86.2
TOI-2158b	124	1186	0.96	0.82	8.6	0.86	9.07	1.5	74.0	44.3	86.3
WASP-153b	125	1712	1.55	0.39	3.33	0.61	11.05	1.3	53.1	68.4	86.6
HAT-P−34b	126	1476	1.2	3.33	5.45	0.48	9.25	1.5	41.8	76.1	86.8

Table A3 – *continued*

Planet name	Rank	T_{eq} (K)	R_p (R_J)	M_p (M_J)	P (d)	b	K (mag)	N_{max}	EMM$_x$ (deg)	EMM$_y$ (deg)	EMM (deg)
WASP-173Ab	127	1871	1.2	3.69	1.39	0.4	10.0	1.8	35.0	79.7	87.0
Qatar-2b	128	1348	1.25	2.49	1.34	0.4	10.62	1.8	35.2	80.3	87.7
TOI-3235b	129	604	1.02	0.66	2.59	0.51	10.82	1.4	44.9	75.5	87.8
WASP-12b	130	2594	1.94	1.46	1.09	0.34	10.19	2.2	29.8	82.7	87.9
TOI-3321b	131	1620	1.39	0.55	3.65	0.42	9.67	1.7	37.1	80.8	88.9
HAT-P−3b	132	1186	0.94	0.65	2.9	0.46	9.45	1.5	41.0	79.0	89.0
TOI-2587Ab	133	1450	1.08	0.22	5.46	0.71	9.99	1.2	63.6	62.3	89.0
NGTS-5b	134	1058	1.14	0.23	3.36	0.66	11.61	1.2	58.8	67.2	89.3
KELT-21b	135	2053	1.59	3.91	3.61	0.42	10.09	1.7	37.9	81.1	89.5
K2-34b	136	1686	1.23	1.7	3.0	0.91	10.19	1.7	81.4	38.2	89.9

APPENDIX B: BEST ECLIPSE MAPPING TARGETS FOR JWST

Here, we tabulate the best eclipse mapping targets for three *JWST* spectrographs (NIRISS/SOSS, Table B1; NIRSpec/G395H, Table B2; and MIRI/LRS, Table B3) as identified by their analytically calculated eclipse mapping metrics (EMMs, S. Boone et al. 2024). We define a target to be 'eclipse mappable' if it has an EMM$< 90^\circ$ and $N_{max} \geq 1$. We list the targets in order of their overall EMM. These tables are expanded versions of those presented in S. Boone et al. (2024), who present the top 15 targets for each of these spectrographs. We expand on them here to encourage future eclipse mapping work with *JWST* of a greater number of targets.

Table B1. 100 best eclipse mapping targets for *JWST* NIRISS/SOSS. We list these targets in order of their overall EMM ranking, include relevant system parameters, along with our calculated EMM$_x$, EMM$_x$, and N_{max} values (see the text for details). The full list of best eclipse mapping targets for each instrument can be found on Zenodo at 10.5281/zenodo.17245372.

Planet name	Rank	T_{eq} (K)	R_p (R_J)	M_p (M_J)	P (d)	b	K (mag)	N_{max}	EMM$_x$ (deg)	EMM$_y$ (deg)	EMM (deg)
TOI-2109 b	1	3072	1.35	5.02	0.67	0.75	9.07	4.3	23.2	20.6	31.0
HAT-P−70 b	2	2552	1.87	6.78	2.74	0.62	8.96	4.1	20.5	26.0	33.1
WASP-19 b	3	2117	1.42	1.15	0.79	0.67	10.48	3.8	23.4	26.1	35.0
WASP-189 b	4	2636	1.62	1.99	2.72	0.48	6.06	4.4	17.2	31.5	35.8
KELT-20 b	5	2263	1.74	3.38	3.47	0.5	7.42	4.1	18.5	31.9	36.9
WASP-167 b	6	2363	1.58	8.0	2.02	0.77	9.76	3.4	29.7	24.7	38.6
KELT-14 b	7	1961	1.74	1.28	1.71	0.86	9.42	3.9	33.3	19.6	38.7
KELT-4 A b	8	1822	1.7	0.9	2.99	0.69	8.69	3.3	26.7	28.0	38.7
KELT-7 b	9	2089	1.6	1.39	2.73	0.57	7.54	3.5	22.8	32.8	40.0
WASP-178 b	10	2469	1.81	1.66	3.34	0.54	9.7	3.6	21.6	33.7	40.0
TOI-1431 b	11	2395	1.49	3.12	2.65	0.88	7.44	3.9	35.9	19.1	40.7
WASP-87 b	12	2313	1.38	2.18	1.68	0.6	9.55	3.3	24.6	32.6	40.8
KELT-19 A b	13	1938	1.91	4.07	4.61	0.6	9.2	3.2	25.4	33.9	42.4
KELT-17 b	14	2090	1.52	1.31	3.08	0.57	8.65	3.2	24.2	35.0	42.6
WASP-14 b	15	1920	1.38	8.84	2.24	0.56	8.62	3.1	24.8	36.5	44.1
TOI-2046 b	16	2029	1.44	2.3	1.5	0.53	10.09	3.2	23.5	37.7	44.4
KELT-3 b	17	1952	1.56	1.94	2.7	0.53	8.66	3.2	23.7	37.7	44.6
HAT-P−30 b	18	1699	1.44	0.83	2.81	0.77	9.15	2.9	34.6	28.9	45.1
HD 189733 b	19	1193	1.13	1.13	2.22	0.67	5.54	2.8	30.7	33.9	45.7
WASP-18 b	20	2504	1.24	10.2	0.94	0.37	8.13	4.1	17.5	43.5	46.9
KELT-23 A b	21	1565	1.32	0.94	2.26	0.57	8.9	2.8	27.3	39.0	47.5
WASP-48 b	22	1933	1.5	0.8	2.14	0.81	10.37	2.8	38.4	28.1	47.6
HAT-P−56 b	23	1866	1.51	2.31	2.79	0.85	9.83	2.9	40.7	25.5	48.0
XO-7 b	24	1744	1.37	0.71	2.86	0.73	9.24	2.6	35.4	32.9	48.3
GPX-1 b	25	2293	1.47	19.7	1.74	0.82	11.18	2.8	39.5	27.9	48.3
HAT-P−60 b	26	1773	1.63	0.57	4.79	0.67	8.37	2.6	32.4	36.1	48.5
WASP-43 b	27	1379	0.93	1.78	0.81	0.66	9.27	2.6	32.0	36.9	48.9
WASP-12 b	28	2594	1.94	1.46	1.09	0.34	10.19	4.3	16.6	46.0	48.9

Table B1 – *continued*

Planet name	Rank	T_{eq} (K)	R_p (R_J)	M_p (M_J)	P (d)	b	K (mag)	N_{max}	EMM$_x$ (deg)	EMM$_y$ (deg)	EMM (deg)
TOI-1937 A b	29	2096	1.25	2.01	0.95	0.87	11.23	3.0	42.5	24.6	49.1
WASP-187 b	30	1952	1.64	0.8	5.15	0.76	8.79	2.6	37.4	32.0	49.2
WASP-135 b	31	1720	1.3	1.9	1.4	0.76	11.04	2.6	37.3	32.1	49.2
HD 209458 b	32	1477	1.39	0.73	3.52	0.49	6.31	3.0	24.2	43.2	49.5
HAT-P−7 b	33	2272	1.51	1.84	2.2	0.47	9.33	3.1	23.5	43.6	49.6
TrES-2 b	34	1581	1.36	1.49	2.47	0.77	9.85	2.5	38.2	32.0	49.8
WASP-100 b	35	1949	1.33	1.26	2.85	0.81	9.67	2.6	40.3	29.5	49.9
TOI-778 b	36	1710	1.37	2.8	4.63	0.7	8.06	2.5	34.8	35.8	49.9
WASP-101 b	37	1566	1.43	0.51	3.59	0.72	9.07	2.5	36.5	34.8	50.4
KELT-8 b	38	1571	1.62	0.66	3.24	0.86	9.18	2.8	43.8	26.3	51.1
WASP-24 b	39	1827	1.38	1.24	2.34	0.61	10.15	2.5	31.4	40.5	51.2
WASP-36 b	40	1747	1.33	2.36	1.54	0.69	11.29	2.4	35.6	36.9	51.3
WASP-120 b	41	1876	1.47	4.85	3.61	0.77	9.88	2.4	39.6	33.1	51.6
HAT-P−14 b	42	1758	1.42	3.44	4.63	0.8	8.85	2.5	41.2	31.2	51.7
WASP-54 b	43	1747	1.58	0.59	3.69	0.53	9.04	2.7	27.9	44.1	52.2
HATS-56 b	44	1901	1.69	0.6	4.32	0.69	10.25	2.3	36.6	38.4	53.0
WASP-142 b	45	1992	1.53	0.84	2.05	0.77	11.44	2.4	41.1	33.6	53.1
KELT-12 b	46	1799	1.78	0.95	5.03	0.59	9.36	2.4	31.6	43.6	53.9
OGLE2-TR-L9 b	47	2356	1.61	4.5	2.49	0.77	13.12	2.3	41.3	34.6	53.9
HATS-67 b	48	2191	1.68	1.45	1.61	0.86	12.33	2.7	46.5	27.4	53.9
WASP-3 b	49	2086	1.42	2.43	1.85	0.41	9.36	3.2	21.9	49.4	54.0
HAT-P−6 b	50	1761	1.48	1.32	3.85	0.54	9.31	2.5	29.6	45.5	54.3
WASP-104 b	51	1514	1.14	1.27	1.76	0.73	9.88	2.2	39.6	37.6	54.6
XO-6 b	52	1577	2.07	4.4	3.77	0.63	9.25	2.3	34.6	42.3	54.7
WASP-79 b	53	1716	1.53	0.85	3.66	0.5	9.06	2.6	27.5	47.3	54.7
WASP-46 b	54	1639	1.17	1.91	1.43	0.73	11.4	2.2	40.3	37.5	55.0
HD 202772 A b	55	2133	1.54	1.02	3.31	0.41	6.96	3.1	22.9	50.3	55.2
WASP-31 b	56	1574	1.55	0.48	3.41	0.78	10.65	2.3	43.2	34.6	55.3
TrES-4 b	57	1708	1.61	0.78	3.55	0.82	10.33	2.4	45.7	31.4	55.4
HAT-P−13 b	58	1727	1.27	0.85	2.92	0.62	8.98	2.3	34.2	43.7	55.5
TOI-640 b	59	1747	1.77	0.88	5.0	0.89	9.24	2.7	49.7	25.8	56.0
WASP-90 b	60	1840	1.63	0.63	3.92	0.84	10.25	2.4	47.1	30.5	56.1
WASP-92 b	61	1879	1.46	0.8	2.17	0.61	11.52	2.2	34.3	44.7	56.3
WASP-50 b	62	1394	1.17	1.47	1.96	0.67	9.97	2.1	38.4	42.6	57.3
Qatar-1 b	63	1416	1.14	1.29	1.42	0.65	10.41	2.1	37.4	44.1	57.8
HATS-65 b	64	1633	1.5	0.82	3.11	0.67	11.1	2.0	39.2	43.8	58.8
TOI-2236 b	65	1687	1.28	1.58	3.53	0.77	9.96	2.1	45.3	37.9	59.0
TOI-157 b	66	1591	1.29	1.18	2.08	0.8	10.89	2.1	47.5	35.4	59.3
WASP-136 b	67	1745	1.38	1.51	5.22	0.59	8.8	2.1	35.6	48.1	59.9
CoRoT-11 b	68	1741	1.43	2.33	2.99	0.81	11.25	2.1	48.8	34.8	59.9
HAT-P−50 b	69	1855	1.29	1.35	3.12	0.63	10.5	2.0	38.0	46.4	60.0
WASP-164 b	70	1608	1.13	2.13	1.78	0.82	10.96	2.2	49.6	34.0	60.1
TOI-2669 b	71	1771	1.76	0.61	6.2	0.86	8.49	2.3	51.6	30.9	60.2
WASP-119 b	72	1566	1.4	1.23	2.5	0.57	10.54	2.1	34.1	49.6	60.2
WASP-17 b	73	1699	1.93	0.48	3.74	0.35	10.22	2.6	26.4	54.2	60.3
KELT-21 b	74	2053	1.59	3.91	3.61	0.42	10.09	2.7	25.5	54.7	60.3
WASP-16 b	75	1440	1.22	1.24	3.12	0.65	9.59	2.0	39.4	45.8	60.4
TOI-3331 A b	76	1487	1.16	2.27	2.02	0.57	9.91	2.1	34.6	49.7	60.5
WASP-52 b	77	1299	1.27	0.46	1.75	0.6	10.09	2.0	36.6	48.7	60.9
TOI-1333 b	78	1680	1.4	2.37	4.72	0.52	8.27	2.2	31.9	51.9	60.9
WASP-75 b	79	1705	1.27	1.07	2.48	0.89	10.06	2.5	54.3	27.7	61.0
WASP-20 b	80	1378	1.46	0.31	4.9	0.72	9.39	1.9	44.2	42.8	61.6
WASP-131 b	81	1460	1.22	0.27	5.32	0.74	8.57	1.9	46.1	41.4	62.0
HAT-P−1 b	82	1322	1.32	0.52	4.47	0.78	8.86	2.0	48.3	39.0	62.1
WASP-123 b	83	1522	1.32	0.9	2.98	0.53	9.36	2.2	32.9	52.9	62.3
WASP-15 b	84	1626	1.41	0.54	3.75	0.53	9.69	2.2	33.0	52.9	62.4
K2-107 b	85	1804	1.43	0.84	3.31	0.75	11.21	1.9	46.9	41.3	62.5
WASP-13 b	86	1450	1.22	0.36	4.35	0.67	9.12	1.9	42.0	46.4	62.6
WASP-153 b	87	1712	1.55	0.39	3.33	0.61	11.05	1.9	38.5	49.6	62.8
WASP-71 b	88	1830	1.18	1.39	2.9	0.55	9.32	2.1	34.7	52.4	62.8
WASP-173 A b	89	1871	1.2	3.69	1.39	0.4	10.0	2.7	25.3	57.6	62.9
WASP-2 b	90	1314	1.08	0.93	2.15	0.75	9.63	1.9	47.0	41.9	62.9

Table B1 – *continued*

Planet name	Rank	T_{eq} (K)	R_p (R_J)	M_p (M_J)	P (d)	b	K (mag)	N_{max}	EMM$_x$ (deg)	EMM$_y$ (deg)	EMM (deg)
WASP-33 b	91	2781	1.59	2.09	1.22	0.21	7.47	5.2	13.3	62.1	63.5
WASP-49 b	92	1366	1.11	0.37	2.78	0.75	9.75	1.9	47.7	42.3	63.8
HD 149026 b	93	1693	0.74	0.38	2.88	0.63	6.82	1.9	40.4	49.5	63.9
TOI-615 b	94	1668	1.69	0.44	4.66	0.48	9.67	2.2	30.9	56.3	64.2
WASP-163 b	95	1634	1.2	1.87	1.61	0.45	10.15	2.4	29.0	57.2	64.2
Gaia-2 b	96	1314	1.32	0.82	3.69	0.79	9.74	1.9	50.9	39.4	64.4
WASP-114 b	97	2028	1.34	1.77	1.55	0.45	11.07	2.4	29.1	57.5	64.5
WASP-78 b	98	2470	1.93	1.11	2.18	0.36	11.01	2.9	23.4	60.3	64.7
TOI-3894 b	99	1531	1.36	0.82	4.33	0.72	10.48	1.8	46.6	45.1	64.8
KELT-16 b	100	2452	1.42	2.75	0.97	0.32	10.64	3.3	20.6	61.9	65.2

Table B2. 100 best eclipse mapping targets for *JWST* NIRSpec/G395H. We list these targets in order of their overall EMM ranking, include relevant system parameters, along with our calculated EMM$_x$, EMM$_x$, and N_{max} values (see the text for details). The full list of best eclipse mapping targets for each instrument can be found on Zenodo at 10.5281/zenodo.17245372.

Planet name	Rank	T_{eq} (K)	R_p (R_J)	M_p (M_J)	P (d)	b	K (mag)	N_{max}	EMM$_x$ (deg)	EMM$_y$ (deg)	EMM (deg)
HD 189733 b	1	1193	1.13	1.13	2.22	0.67	5.54	5.5	16.6	18.4	24.8
KELT-4 A b	2	1822	1.7	0.9	2.99	0.69	8.69	4.5	20.5	21.5	29.7
KELT-20 b	3	2263	1.74	3.38	3.47	0.5	7.42	5.2	15.0	25.8	29.9
WASP-19 b	4	2117	1.42	1.15	0.79	0.67	10.48	4.4	20.2	22.6	30.3
HAT-P−70 b	5	2552	1.87	6.78	2.74	0.62	8.96	4.5	18.9	24.0	30.5
KELT-7 b	6	2089	1.6	1.39	2.73	0.57	7.54	4.6	17.6	25.4	30.9
WASP-43 b	7	1379	0.93	1.78	0.81	0.66	9.27	4.3	20.4	23.5	31.1
TOI-2109 b	8	3072	1.35	5.02	0.67	0.75	9.07	4.3	23.5	20.9	31.5
KELT-14 b	9	1961	1.74	1.28	1.71	0.86	9.42	4.9	27.4	16.1	31.7
KELT-23 A b	10	1565	1.32	0.94	2.26	0.57	8.9	4.3	18.9	27.0	32.9
HAT-P−30 b	11	1699	1.44	0.83	2.81	0.77	9.15	4.0	25.6	21.4	33.3
HD 209458 b	12	1477	1.39	0.73	3.52	0.49	6.31	4.7	16.3	29.1	33.4
KELT-19 A b	13	1938	1.91	4.07	4.61	0.6	9.2	4.1	20.4	27.3	34.1
TOI-1431 b	14	2395	1.49	3.12	2.65	0.88	7.44	4.8	30.2	16.0	34.2
WASP-14 b	15	1920	1.38	8.84	2.24	0.56	8.62	4.1	19.6	28.8	34.9
WASP-101 b	16	1566	1.43	0.51	3.59	0.72	9.07	3.8	25.3	24.2	35.0
WASP-189 b	17	2636	1.62	1.99	2.72	0.48	6.06	4.5	16.8	30.8	35.1
WASP-167 b	18	2363	1.58	8.0	2.02	0.77	9.76	3.8	27.1	22.5	35.2
TrES-2 b	19	1581	1.36	1.49	2.47	0.77	9.85	3.8	27.1	22.7	35.3
KELT-17 b	20	2090	1.52	1.31	3.08	0.57	8.65	4.0	20.1	29.1	35.4
TOI-778 b	21	1710	1.37	2.8	4.63	0.7	8.06	3.7	24.8	25.5	35.6
KELT-8 b	22	1571	1.62	0.66	3.24	0.86	9.18	4.2	30.6	18.4	35.7
KELT-3 b	23	1952	1.56	1.94	2.7	0.53	8.66	4.1	19.1	30.4	35.9
HAT-P−60 b	24	1773	1.63	0.57	4.79	0.67	8.37	3.6	24.1	26.8	36.1
WASP-52 b	25	1299	1.27	0.46	1.75	0.6	10.09	3.7	22.0	29.3	36.7
XO-7 b	26	1744	1.37	0.71	2.86	0.73	9.24	3.6	26.9	25.0	36.7
WASP-178 b	27	2469	1.81	1.66	3.34	0.54	9.7	4.0	19.8	31.0	36.8
WASP-50 b	28	1394	1.17	1.47	1.96	0.67	9.97	3.6	24.7	27.4	36.8
WASP-87 b	29	2313	1.38	2.18	1.68	0.6	9.55	3.7	22.3	29.4	36.9
WASP-69 b	30	988	1.11	0.29	3.87	0.65	7.46	3.6	24.0	28.1	37.0
WASP-135 b	31	1720	1.3	1.9	1.4	0.76	11.04	3.5	28.2	24.3	37.2
HAT-P−1 b	32	1322	1.32	0.52	4.47	0.78	8.86	3.6	29.1	23.5	37.4
TOI-2046 b	33	2029	1.44	2.3	1.5	0.53	10.09	3.9	19.8	31.8	37.4
WASP-104 b	34	1514	1.14	1.27	1.76	0.73	9.88	3.5	27.3	25.9	37.7
Qatar-1 b	35	1416	1.14	1.29	1.42	0.65	10.41	3.5	24.5	28.9	37.8
HAT-P−56 b	36	1866	1.51	2.31	2.79	0.85	9.83	3.8	32.4	20.3	38.3
XO-6 b	37	1577	2.07	4.4	3.77	0.63	9.25	3.5	24.3	29.7	38.3
WASP-2 b	38	1314	1.08	0.93	2.15	0.75	9.63	3.4	28.7	25.6	38.5
HAT-P−14 b	39	1758	1.42	3.44	4.63	0.8	8.85	3.5	31.0	23.5	38.9
WASP-20 b	40	1378	1.46	0.31	4.9	0.72	9.39	3.3	28.1	27.2	39.1

Table B2 – *continued*

Planet name	Rank	T_{eq} (K)	R_p (R_J)	M_p (M_J)	P (d)	b	K (mag)	N_{max}	EMM$_x$ (deg)	EMM$_y$ (deg)	EMM (deg)
WASP-48 b	41	1933	1.5	0.8	2.14	0.81	10.37	3.5	31.6	23.1	39.1
WASP-36 b	42	1747	1.33	2.36	1.54	0.69	11.29	3.3	27.1	28.2	39.1
Gaia-2 b	43	1314	1.32	0.82	3.69	0.79	9.74	3.4	31.0	24.0	39.2
WASP-31 b	44	1574	1.55	0.48	3.41	0.78	10.65	3.4	30.6	24.5	39.2
HAT-P−2 b	45	1389	1.13	9.02	5.63	0.71	7.6	3.3	27.9	27.9	39.5
WASP-54 b	46	1747	1.58	0.59	3.69	0.53	9.04	3.7	21.2	33.5	39.6
WASP-16 b	47	1440	1.22	1.24	3.12	0.65	9.59	3.3	26.1	30.4	40.1
WASP-46 b	48	1639	1.17	1.91	1.43	0.73	11.4	3.2	29.4	27.4	40.1
WASP-187 b	49	1952	1.64	0.8	5.15	0.76	8.79	3.2	30.5	26.1	40.2
WASP-49 b	50	1366	1.11	0.37	2.78	0.75	9.75	3.2	30.3	26.8	40.5
WASP-131 b	51	1460	1.22	0.27	5.32	0.74	8.57	3.2	30.2	27.1	40.6
WASP-24 b	52	1827	1.38	1.24	2.34	0.61	10.15	3.3	24.9	32.1	40.7
WASP-79 b	53	1716	1.53	0.85	3.66	0.5	9.06	3.7	20.5	35.2	40.8
WASP-100 b	54	1949	1.33	1.26	2.85	0.81	9.67	3.3	33.1	24.2	41.0
TOI-3331 A b	55	1487	1.16	2.27	2.02	0.57	9.91	3.4	23.5	33.8	41.2
HAT-P−6 b	56	1761	1.48	1.32	3.85	0.54	9.31	3.4	22.6	34.8	41.5
WASP-120 b	57	1876	1.47	4.85	3.61	0.77	9.88	3.1	31.9	26.7	41.6
WASP-18 b	58	2504	1.24	10.2	0.94	0.37	8.13	4.7	15.5	38.6	41.6
WASP-13 b	59	1450	1.22	0.36	4.35	0.67	9.12	3.1	27.9	30.9	41.6
TOI-905 b	60	1192	1.17	0.67	3.74	0.82	9.45	3.3	34.2	23.7	41.6
TrES-4 b	61	1708	1.61	0.78	3.55	0.82	10.33	3.3	34.6	23.7	41.9
KELT-12 b	62	1799	1.78	0.95	5.03	0.59	9.36	3.2	24.6	34.0	42.0
HAT-P−13 b	63	1727	1.27	0.85	2.92	0.62	8.98	3.1	25.9	33.1	42.0
TOI-1937 A b	64	2096	1.25	2.01	0.95	0.87	11.23	3.6	36.4	21.1	42.1
HATS-1 b	65	1370	1.3	1.86	3.45	0.7	10.58	3.0	29.8	30.0	42.3
TOI-640 b	66	1747	1.77	0.88	5.0	0.89	9.24	3.8	37.7	19.6	42.5
TOI-157 b	67	1591	1.29	1.18	2.08	0.8	10.89	3.1	34.2	25.5	42.7
WASP-119 b	68	1566	1.4	1.23	2.5	0.57	10.54	3.2	24.3	35.3	42.8
HATS-65 b	69	1633	1.5	0.82	3.11	0.67	11.1	3.0	28.7	32.0	43.0
WASP-123 b	70	1522	1.32	0.9	2.98	0.53	9.36	3.4	22.7	36.5	43.0
HATS-56 b	71	1901	1.69	0.6	4.32	0.69	10.25	2.9	29.8	31.3	43.2
GPX-1 b	72	2293	1.47	19.7	1.74	0.82	11.18	3.1	35.5	25.0	43.4
WASP-164 b	73	1608	1.13	2.13	1.78	0.82	10.96	3.2	35.9	24.6	43.5
TOI-4463 A b	74	1394	1.18	0.79	2.88	0.88	9.4	3.6	38.5	20.6	43.7
K2-29 b	75	1167	1.19	0.73	3.26	0.62	10.06	3.0	26.9	34.5	43.8
TOI-1333 b	76	1680	1.4	2.37	4.72	0.52	8.27	3.3	23.0	37.4	43.9
WASP-142 b	77	1992	1.53	0.84	2.05	0.77	11.44	2.9	34.3	28.0	44.2
WASP-170 b	78	1426	1.1	1.6	2.34	0.69	10.72	2.9	30.6	32.1	44.4
HAT-P−7 b	79	2272	1.51	1.84	2.2	0.47	9.33	3.5	21.1	39.1	44.4
TOI-2236 b	80	1687	1.28	1.58	3.53	0.77	9.96	2.9	34.1	28.5	44.5
WASP-90 b	81	1840	1.63	0.63	3.92	0.84	10.25	3.1	37.5	24.3	44.7
WASP-7 b	82	1486	1.33	0.96	4.95	0.48	8.4	3.4	21.7	39.5	45.0
TrES-5 b	83	1483	1.19	1.79	1.48	0.61	11.59	2.9	27.4	35.8	45.1
WASP-17 b	84	1699	1.93	0.48	3.74	0.35	10.22	3.7	19.7	40.5	45.1
HAT-P−20 b	85	969	0.87	7.25	2.88	0.63	8.6	2.9	28.3	35.1	45.1
HAT-P−46 b	86	1453	1.28	0.49	4.46	0.7	9.92	2.8	31.4	32.4	45.1
KPS-1 b	87	1448	1.03	1.09	1.71	0.75	10.93	2.8	34.0	29.7	45.1
HAT-P−22 b	88	1324	1.15	2.47	3.21	0.43	7.84	3.7	19.6	40.7	45.2
WASP-92 b	89	1879	1.46	0.8	2.17	0.61	11.52	2.9	27.5	35.9	45.2
WASP-15 b	90	1626	1.41	0.54	3.75	0.53	9.69	3.1	24.0	38.6	45.4
WASP-136 b	91	1745	1.38	1.51	5.22	0.59	8.8	2.9	27.1	36.6	45.6
TOI-3894 b	92	1531	1.36	0.82	4.33	0.72	10.48	2.8	32.8	31.8	45.7
CoRoT-11 b	93	1741	1.43	2.33	2.99	0.81	11.25	2.9	37.3	26.6	45.8
WASP-75 b	94	1705	1.27	1.07	2.48	0.89	10.06	3.5	40.9	20.9	45.9
HD 202772 A b	95	2133	1.54	1.02	3.31	0.41	6.96	3.8	19.0	41.9	46.0
WASP-3 b	96	2086	1.42	2.43	1.85	0.41	9.36	3.9	18.6	42.1	46.0
HATS-67 b	97	2191	1.68	1.45	1.61	0.86	12.33	3.2	39.9	23.5	46.3
TOI-4145 A b	98	1075	1.19	0.43	4.07	0.8	10.29	2.8	37.1	27.9	46.4
WASP-98 b	99	1170	1.14	0.92	2.96	0.69	11.28	2.7	32.1	33.7	46.5
HD 149026 b	100	1693	0.74	0.38	2.88	0.63	6.82	2.8	29.5	36.1	46.6

Table B3. 100 best eclipse mapping targets for *JWST* MIRI/LRS. We list these targets in order of their overall EMM ranking, include relevant system parameters, along with our calculated EMM_x, EMM_x, and N_{max} values (see the text for details). The full list of best eclipse mapping targets for each instrument can be found on Zenodo at 10.5281/zenodo.17245372.

Planet Name	Rank	T_{eq} (K)	R_p (R_J)	M_p (M_J)	P (d)	b	K (mag)	N_{max}	EMM_x (deg)	EMM_y (deg)	EMM (deg)
HD 189733 b	1	1193	1.13	1.13	2.22	0.67	5.54	5.9	15.6	17.2	23.2
HD 209458 b	2	1477	1.39	0.73	3.52	0.49	6.31	5.0	15.4	27.5	31.5
WASP-69 b	3	988	1.11	0.29	3.87	0.65	7.46	4.1	21.4	25.1	33.0
KELT-20 b	4	2263	1.74	3.38	3.47	0.5	7.42	4.7	16.7	28.7	33.2
KELT-4 A b	5	1822	1.7	0.9	2.99	0.69	8.69	3.9	23.5	24.6	34.1
KELT-7 b	6	2089	1.6	1.39	2.73	0.57	7.54	4.1	19.7	28.4	34.6
WASP-43 b	7	1379	0.93	1.78	0.81	0.66	9.27	3.8	22.7	26.2	34.7
KELT-23 A b	8	1565	1.32	0.94	2.26	0.57	8.9	3.8	21.1	30.2	36.9
HAT-P−70 b	9	2552	1.87	6.78	2.74	0.62	8.96	3.6	23.1	29.2	37.2
WASP-189 b	10	2636	1.62	1.99	2.72	0.48	6.06	4.1	18.2	33.4	38.1
HAT-P−30 b	11	1699	1.44	0.83	2.81	0.77	9.15	3.4	29.4	24.6	38.4
KELT-14 b	12	1961	1.74	1.28	1.71	0.86	9.42	3.9	33.2	19.5	38.5
TOI-1431 b	13	2395	1.49	3.12	2.65	0.88	7.44	4.2	34.0	18.1	38.5
TOI-778 b	14	1710	1.37	2.8	4.63	0.7	8.06	3.3	27.1	27.9	38.9
WASP-101 b	15	1566	1.43	0.51	3.59	0.72	9.07	3.3	28.5	27.2	39.4
HAT-P−1 b	16	1322	1.32	0.52	4.47	0.78	8.86	3.3	30.8	24.9	39.6
TOI-2109 b	17	3072	1.35	5.02	0.67	0.75	9.07	3.3	29.8	26.5	39.9
HAT-P−2 b	18	1389	1.13	9.02	5.63	0.71	7.6	3.2	28.2	28.3	40.0
WASP-14 b	19	1920	1.38	8.84	2.24	0.56	8.62	3.5	22.6	33.2	40.2
KELT-19 A b	20	1938	1.91	4.07	4.61	0.6	9.2	3.3	24.1	32.3	40.3
HAT-P−60 b	21	1773	1.63	0.57	4.79	0.67	8.37	3.2	27.0	30.1	40.4
KELT-8 b	22	1571	1.62	0.66	3.24	0.86	9.18	3.7	34.7	20.8	40.5
WASP-19 b	23	2117	1.42	1.15	0.79	0.67	10.48	3.2	27.0	30.2	40.6
KELT-17 b	24	2090	1.52	1.31	3.08	0.57	8.65	3.4	23.5	33.9	41.3
KELT-3 b	25	1952	1.56	1.94	2.7	0.53	8.66	3.5	22.2	35.3	41.7
TrES-2 b	26	1581	1.36	1.49	2.47	0.77	9.85	3.1	32.1	26.9	41.9
WASP-52 b	27	1299	1.27	0.46	1.75	0.6	10.09	3.2	25.3	33.7	42.1
HAT-P−20 b	28	969	0.87	7.25	2.88	0.63	8.6	3.1	26.5	32.8	42.1
XO-7 b	29	1744	1.37	0.71	2.86	0.73	9.24	3.0	31.1	28.9	42.5
WASP-50 b	30	1394	1.17	1.47	1.96	0.67	9.97	3.0	28.6	31.7	42.7
WASP-2 b	31	1314	1.08	0.93	2.15	0.75	9.63	3.0	31.9	28.5	42.8
WASP-20 b	32	1378	1.46	0.31	4.9	0.72	9.39	2.9	31.1	30.1	43.2
XO-6 b	33	1577	2.07	4.4	3.77	0.63	9.25	3.0	27.5	33.6	43.4
WASP-131 b	34	1460	1.22	0.27	5.32	0.74	8.57	2.9	32.5	29.2	43.7
Gaia-2 b	35	1314	1.32	0.82	3.69	0.79	9.74	3.0	34.6	26.8	43.8
TOI-905 b	36	1192	1.17	0.67	3.74	0.82	9.45	3.1	36.1	25.1	44.0
WASP-104 b	37	1514	1.14	1.27	1.76	0.73	9.88	2.9	32.0	30.3	44.1
HAT-P−14 b	38	1758	1.42	3.44	4.63	0.8	8.85	3.0	35.3	26.7	44.3
WASP-167 b	39	2363	1.58	8.0	2.02	0.77	9.76	2.9	34.3	28.5	44.6
WASP-16 b	40	1440	1.22	1.24	3.12	0.65	9.59	2.8	29.7	34.5	45.5
WASP-54 b	41	1747	1.58	0.59	3.69	0.53	9.04	3.1	24.4	38.6	45.7
Qatar-1 b	42	1416	1.14	1.29	1.42	0.65	10.41	2.8	29.6	34.9	45.7
WASP-49 b	43	1366	1.11	0.37	2.78	0.75	9.75	2.8	34.2	30.3	45.7
HAT-P−22 b	44	1324	1.15	2.47	3.21	0.43	7.84	3.7	19.9	41.2	45.8
WASP-13 b	45	1450	1.22	0.36	4.35	0.67	9.12	2.8	30.9	34.1	46.0
TOI-677 b	46	1066	1.17	1.24	11.24	0.72	8.43	2.7	33.3	32.0	46.1
WASP-87 b	47	2313	1.38	2.18	1.68	0.6	9.55	2.8	27.9	36.8	46.2
WASP-178 b	48	2469	1.81	1.66	3.34	0.54	9.7	3.0	25.0	39.0	46.3
WASP-187 b	49	1952	1.64	0.8	5.15	0.76	8.79	2.7	35.5	30.4	46.7
WASP-79 b	50	1716	1.53	0.85	3.66	0.5	9.06	3.2	23.5	40.4	46.8
HAT-P−56 b	51	1866	1.51	2.31	2.79	0.85	9.83	3.0	39.7	24.9	46.9
TOI-1811 b	52	962	0.99	0.97	3.71	0.75	9.64	2.7	35.8	31.3	47.6
HD 149026 b	53	1693	0.74	0.38	2.88	0.63	6.82	2.7	30.1	36.9	47.7
TOI-2046 b	54	2029	1.44	2.3	1.5	0.53	10.09	3.0	25.2	40.5	47.7
K2-29 b	55	1167	1.19	0.73	3.26	0.62	10.06	2.7	29.6	37.9	48.0
HAT-P−13 b	56	1727	1.27	0.85	2.92	0.62	8.98	2.7	29.6	37.9	48.0
TOI-3331 A b	57	1487	1.16	2.27	2.02	0.57	9.91	2.8	27.5	39.5	48.1
WASP-7 b	58	1486	1.33	0.96	4.95	0.48	8.4	3.2	23.2	42.3	48.3
TOI-1333 b	59	1680	1.4	2.37	4.72	0.52	8.27	3.0	25.3	41.2	48.3
TOI-4463 A b	60	1394	1.18	0.79	2.88	0.88	9.4	3.2	42.7	22.8	48.4
HAT-P−6 b	61	1761	1.48	1.32	3.85	0.54	9.31	2.9	26.4	40.7	48.5

Table B3 – *continued*

Planet Name	Rank	T_{eq} (K)	R_p (R_J)	M_p (M_J)	P (d)	b	K (mag)	N_{max}	EMM$_x$ (deg)	EMM$_y$ (deg)	EMM (deg)
WASP-123 b	62	1522	1.32	0.9	2.98	0.53	9.36	2.9	25.8	41.5	48.8
WASP-84 b	63	801	0.96	0.69	8.52	0.65	8.86	2.6	31.8	37.4	49.1
HD 202772 A b	64	2133	1.54	1.02	3.31	0.41	6.96	3.5	20.4	44.8	49.2
WASP-18 b	65	2504	1.24	10.2	0.94	0.37	8.13	3.9	18.4	45.7	49.3
KELT-12 b	66	1799	1.78	0.95	5.03	0.59	9.36	2.7	29.0	40.0	49.4
WASP-31 b	67	1574	1.55	0.48	3.41	0.78	10.65	2.6	38.6	30.8	49.4
TOI-640 b	68	1747	1.77	0.88	5.0	0.89	9.24	3.2	43.9	22.8	49.5
WASP-100 b	69	1949	1.33	1.26	2.85	0.81	9.67	2.6	40.2	29.4	49.8
HD 17156 b	70	899	1.1	3.51	21.22	0.86	6.76	2.9	42.8	25.5	49.9
WASP-135 b	71	1720	1.3	1.9	1.4	0.76	11.04	2.5	37.9	32.6	50.0
TOI-4145 A b	72	1075	1.19	0.43	4.07	0.8	10.29	2.6	40.1	30.1	50.2
WASP-48 b	73	1933	1.5	0.8	2.14	0.81	10.37	2.6	40.7	29.8	50.5
WASP-24 b	74	1827	1.38	1.24	2.34	0.61	10.15	2.5	31.1	40.2	50.8
HATS-1 b	75	1370	1.3	1.86	3.45	0.7	10.58	2.4	35.8	36.1	50.9
WASP-120 b	76	1876	1.47	4.85	3.61	0.77	9.88	2.5	39.1	32.7	51.0
GJ 436 b	77	687	0.37	0.07	2.64	0.84	6.07	2.7	43.5	27.6	51.5
WASP-136 b	78	1745	1.38	1.51	5.22	0.59	8.8	2.5	30.7	41.5	51.6
HAT-P−46 b	79	1453	1.28	0.49	4.46	0.7	9.92	2.4	36.2	37.4	52.0
TrES-4 b	80	1708	1.61	0.78	3.55	0.82	10.33	2.5	43.1	29.6	52.3
KELT-11 b	81	1703	1.35	0.17	4.74	0.41	6.12	3.3	21.5	48.0	52.6
HAT-P−54 b	82	821	0.94	0.76	3.8	0.74	10.33	2.3	38.9	35.6	52.8
TOI-2669 b	83	1771	1.76	0.61	6.2	0.86	8.49	2.7	45.5	27.2	53.0
WASP-119 b	84	1566	1.4	1.23	2.5	0.57	10.54	2.5	30.2	43.9	53.3
WASP-15 b	85	1626	1.41	0.54	3.75	0.53	9.69	2.6	28.2	45.3	53.4
TOI-2236 b	86	1687	1.28	1.58	3.53	0.77	9.96	2.3	41.0	34.3	53.5
TOI-622 b	87	1382	0.82	0.3	6.4	0.63	7.86	2.3	33.9	41.6	53.7
WASP-36 b	88	1747	1.33	2.36	1.54	0.69	11.29	2.3	37.3	38.7	53.8
WASP-185 b	89	1159	1.25	0.98	9.39	0.72	9.51	2.3	39.1	37.3	54.1
TOI-3235 b	90	604	1.02	0.66	2.59	0.51	10.82	2.6	27.7	46.6	54.2
WASP-91 b	91	1144	1.03	1.34	2.8	0.52	9.71	2.6	28.0	46.4	54.2
WASP-170 b	92	1426	1.1	1.6	2.34	0.69	10.72	2.2	37.4	39.3	54.3
HATS-56 b	93	1901	1.69	0.6	4.32	0.69	10.25	2.2	37.6	39.4	54.5
HAT-P−7 b	94	2272	1.51	1.84	2.2	0.47	9.33	2.8	25.9	48.0	54.6
TOI-1194 b	95	1382	0.78	0.38	2.31	0.8	9.34	2.3	43.6	32.9	54.6
WASP-8 b	96	968	1.13	2.54	8.16	0.42	8.09	3.0	23.1	49.5	54.7
WASP-32 b	97	1454	0.96	2.63	2.72	0.76	10.16	2.2	41.8	35.6	54.9
WASP-46 b	98	1639	1.17	1.91	1.43	0.73	11.4	2.2	40.3	37.5	55.0
TOI-157 b	99	1591	1.29	1.18	2.08	0.8	10.89	2.3	44.3	33.0	55.3
WASP-17 b	100	1699	1.93	0.48	3.74	0.35	10.22	2.9	24.4	50.1	55.8

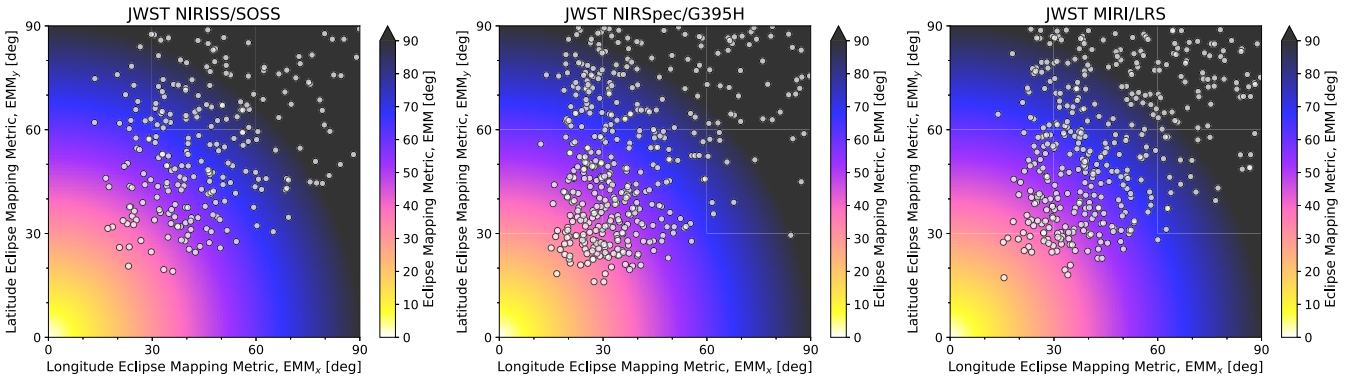

Figure B1. The EMM parameter space for three *JWST* spectrographs: (left) NIRISS/SOSS, (middle) NIRSpec/G395H, and (right) MIRI/LRS. Targets increase in ranking going to the bottom left of the plots.

This paper has been typeset from a TEX/LATEX file prepared by the author.